TRANSVERSE ENERGY MEASUREMENT AND FLUCTUATION STUDIES IN ULTRA-RELATIVISTIC HEAVY ION COLLISIONS

A THESIS SUBMITTED TO THE
UTKAL UNIVERSITY
FOR THE DEGREE OF
DOCTOR OF PHILOSOPHY IN SCIENCE
(PHYSICS)
APRIL, 2007

By
RAGHUNATH SAHOO

INSTITUTE OF PHYSICS, BHUBANESWAR- 751 005, INDIA

CERTIFICATE

This is to certify that the thesis entitled **" Transverse energy measurement and fluctuation studies in ultra-relativistic heavy ion collisions"** which is being submitted by **Mr. Raghunath Sahoo** in partial fulfillment of the degree of **Doctor of Philosophy in Science (Physics) of Utkal University, Bhubaneswar** is a record of his own research work carried out by him. He has carried out his investigations for the last five and half years on the subject matter of the thesis under my guidance at **Institute of Physics, Bhubaneswar**. The matter embodied in the thesis has not been submitted for the award of any other degree by him or by anybody else.

Prof. D.P. Mahapatra
Institute of Physics
Bhubaneswar 751005

DECLARATION

I, Raghunath Sahoo hereby declare that the thesis entitled **" Transverse energy measurement and fluctuation studies in ultra-relativistic heavy ion collisions"** which is being submitted by me in partial fulfillment of the degree of **Doctor of Philosophy in Science (Physics) of Utkal University, Bhubaneswar** is a record of my own research work carried out by me. I have carried out my investigations for the last five and half years on the subject matter of the thesis under the guidance of Prof. D. P. Mahapatra, at **Institute of Physics, Bhubaneswar**. The matter embodied in the thesis has not been submitted to any other University/Institute for the award of any other degree by me.

Raghunath Sahoo
Institute of Physics
Bhubaneswar 751005

Acknowledgments

I take this opportunity to thank all of my friends, well-wishers and family members for their constant support, advice and encouragements. This thesis would not have been possible without the support of these people.

First, I would like to express my deep sense of gratitude to Prof. D.P. Mahapatra, my thesis supervisor at Institute of Physics, for his invaluable guidance, encouragement and his constant support throughout my research period. He has been with me like a family member.

I also place on record my sincere thanks to Dr. Y.P. Viyogi, the PMD project leader and Director of Institute of Physics, for his support and useful advices throughout my research period. I have learnt a lot from him, specially his patience and his continuous effort till one gets results. It is a pleasure and joyous experience in working with him during the ALICE PMD test beam-time in CERN and PMD installation period at BNL, USA.

It is my pleasure to thank my collaborators: Dr. Subhasis Chattopadhyaya, VECC, Kolkata for giving me his valuable time and useful suggestions during the analysis work. He was very instrumental in pushing this analysis for a success. I am greatly indebted to him for his free sharing of insights and constructive criticism during my research. I have learnt a lot on the technical details of the Barrel Electromagnetic Calorimeter from Prof. A.A.P. Suaide and Dr. (Mrs) Marcia Maria de Moura of the university of Sao Paulo, Bazil. They have been always a source of inspiration and help for me, during the time of data analysis and whenever needed.

I would like to express my heartiest thanks to Prof. B.K. Nandi, IITB; who has been always with me like my elder brother with his all time support and encouragements. He has stood with me in all my bad phases during my research period, giving me courage to stand on my own. I have learnt a lot from him, starting from the basics of ROOT and modular programming to any dipper physics issues. I also express my sincere thanks to Dr. T.K. Nayak for his support and encouragement he has extended for me. I thank Dr. Bedangadas Mohanty for his timely helps through out my Ph.D. period. His sincerity in work and pursuing any analysis in hand without giving it up, is of worth learning. He has been a source of inspiration for me.

I am indebted to Prof. S.N. Behera and Dr. R.K. Choudhury, past directors of IOP for their help and supports in all respects. I would like to express my sincere thanks to Prof. Bikash Sinha, Director VECC and SINP for allowing me to work at VECC and use the facilities there, whenever needed. His hospitality and encouragements are always to remember. My special thanks goes to Dr. D.K. Srivastava, Head Physics Group, VECC, Kolkata for his advice, support, constant encouragements, useful discussions on my analysis results and good wishes for me. I thank Prof. J. Cleymans, University of Cape Town, for useful discussions. I also thank Prof. S.C. Phatak and Prof. A.M. Srivastava for many interesting discussions I had with them. I will be incomplete without thanking Prof. R. Varma, IITB. He has extended his all time encouragements and suggestions during my interaction with him. He has been more like a friend-cum-teacher for me. I am also very thankful to Dr. Jan-e Alam, VECC, Kolkata for giving useful suggestions and helping me in better understanding of QGP and related physics. It was pleasant and joyful in interacting with him both from physics and personal fronts.

I would like to thank the whole STAR collaboration and the PMD group in particular for providing a place for me to work and learn. I have learnt many things from all of our PMD collaborators. It is a great pleasure in interacting in the Spectra Physics Working Group while presenting the analysis results. Working in such a big collaboration has made my capabilities many-folds in terms of presenting myself to bigger and diverging communities. It was a pleasant experience to work with Dr. Anand Kumar Dubey and Dr. Dipak Kumar Mishra, my seniors and collaborators at IOP. I remember the moments I have spent with Dipak bhai discussing various problems while working in the collaboration. I would also like to thank Mr. Ajay Kumar Dash and Mr. Chitrasen Jena for their company while working at IoP.

It was equally interesting to work closely with other members of the PMD group. It includes Dr. M.M. Aggarwal, Dr. A.K. Bhati and their group in Panjab University, Chandigarh; Dr. Sudhir Raniwala and Dr. Rashmi Raniwala from University of Rajasthan, Jaipur; Dr. S.K. Badyal, Dr. L.K. Mangotra, Dr. Saroja K. Nayak, Dr. P.V.K.S. Baba and their group at Jammu University, Jammu; Dr. Zubayer Ahmed, Mr. G.S.N. Murthy, Mr. R.N. Singaraju, Dr. P. Ghosh, Mr. S. Pal and Mr. M.R. Dutta Majumdar of VECC Kolkata. I feel I was very fortunate to work with a number of research scholar friends in the collaboration from the above institutions. I thank them for their help, co-operation and good wishes.

I take this opportunity to thank my seniors, scholar friends and others at IoP. They have made my stay in the beautiful campus of IOP a memorable and pleasing one. It will be impossible for me to forget the picnics, pujas, cricket matches, tennis matches and dinner, lunch, breakfast and tea-time interactions with them. I thank them for all their direct and indirect help throughout my research period at IOP. Special thanks to my friend-cum-elder brother Hara bhai for his company and friendship.

I must mention that, one of the most interesting, knowledgeable and difficult course I have attend is the Pre-Doctoral course at IOP. I thank all my teachers who taught me during the pre-doctoral course and other faculty members of IOP.

I am also thankful to all the staff of the beautiful IOP library, the computer center and all the administrative and non-academic staff of IOP, for their co-operation and help at every stage.

My sincere regards and due respect to my teachers, Prof. N. Barik, Prof. L. P Singh, Prof. S. Mohanty, Prof. L. Maharana, Prof. D.K. Basa, Prof. N.C. Mishra, Prof. (Mrs) P. Khare, Dr. K. Maharana, and Dr. (Mrs) S. Mahapatra at Utkal University, Dr. A.R. Panda and Dr. Sk.Samsur, Dr. J.P. Roy, Purusottama Das who taught me at Kendrapara college. It is because of their teachings, constant encouragement and their blessings, that I have come this far in my research career. I am very pleased in getting a family friend like Mr. Baya Prasad Sahoo, who has been with me in all situations.

My humble regards, respect and thanks goes to my grandfather, late grandmother, parents and in-laws for their patience and encouragement during my research period. It is because of their love, affection and blessings that I could complete this thesis. I also feel delighted to note the love and affections I have got from my brothers and sisters. The person who has been with me at all times giving me her love, affection, encouragements and co-operations is no one except my wife, Gayatri. She has been a driving force in me.

Date: **(Raghunath Sahoo)**

Contents

List of Figures

List of Tables

Chapter 1

Introduction to Physics of Quark Gluon Plasma

1.1 Introduction

The quest to understand the origin of mass, the fundamental particles and their interactions have been a driving force in particle physics research. The nature is governed by four fundamental interactions - the strong, the weak, the electromagnetic and the gravitational interactions. Each of these fundamental interactions are mediated by an exchange particle and the relative strength of the interaction is determined by a characteristic coupling. The most interesting interaction is the strong force which is mediated by color charged gluons unlike the electromagnetic force which is mediated by charge-less photons. Thus the theory of strong interaction, the Quantum Chromodynamics (QCD) is more challenging and exciting than the theory of Quantum Electrodynamics (QED). The structure of nucleons or more generally the structure of hadrons is understood in terms of elementary particles called "quarks" that interact so strongly that they could only be observed in "color-neutral" groups of two (the mesons), three (the baryons) and perhaps five of them. The complicacy of the theory comes through the self interaction of gluons which is also strong in nature.

In 1975, Collins and Perry [1] predicted that at high density $\sim$ few times normal nuclear matter density, the properties of nuclear matter are not governed by the hadronic degrees of freedom but by quark degrees of freedom. Furthermore, lattice QCD calculations suggest that at high temperature ($\sim 150 - 200$) MeV, there will be a phase transition from the confined state of hadrons to the deconfined state of quarks, anti-quarks and gluons, called the Quark Gluon Plasma (QGP). It is expected that nucleus-nucleus collisions at ultra-relativistic energies will be able to create such a deconfined state of matter.

QGP is a thermalized state of matter with overall color neutrality and it's properties are governed by quarks, anti-quarks and gluons which are normally confined within hadrons. In QGP, the inter-particle interaction is much less than the average kinetic energy of the particles. This is one of the properties of a weakly interacting plasma.

1.2 QCD, Deconfinement and QGP

QCD, the non-abelian gauge theory of colored quarks and gluons is the theory of strong interaction. The color charge is associated with the non-abelian gauge group $SU(3)_c$ with the quarks carrying three color charges. The gluons come in eight colors and the gluon fields exhibit self-interaction. QCD exhibits two remarkable features. At low energies and large length scales, QCD is a non-perturbative field theory. The effective coupling constant $\alpha_s(Q^2)$ is large and the quarks and gluons are permanently confined inside hadrons. This feature is usually explained by the postulate of "color confinement", which implies that all observable states are color singlets or colorless objects. Its behavior asymptotically approaches that of a non-interacting free-field theory in the high-energy (large momenta, Q) or short-distance scale limit where, $\alpha_s(Q^2)$ decreases logarithmically. This is commonly called "asymptotic freedom" and it imply that quarks and gluons are weakly interacting at high energies and hence perturbative QCD can be a useful tool at this domain. The QCD Lagrangian is given by

$$\mathcal{L}_{QCD} = i\bar{\psi}\gamma^{\mu}(\partial_{\mu} - igA_{\mu}(x))\psi - m\bar{\psi}\psi - \frac{1}{4}F^{a}_{\mu\nu}F^{\mu\nu}_{a} \qquad (1.1)$$

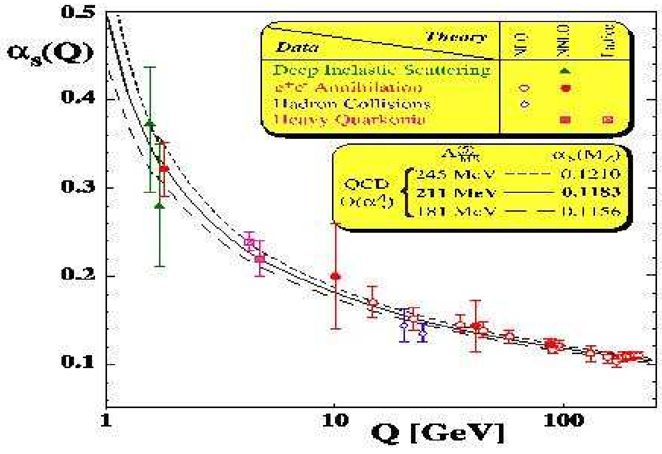

Figure 1.1: (a)The QCD running coupling constant $\alpha_s(Q^2)$ vs Q.

where, the color potential $A_\mu(x)$ is a 3×3 matrix and can be represented by a linear combination of the 8 Gell-Mann matrices (the "generators of $SU(3)$ group"):

$$A_\mu(x) = \frac{1}{2}\sum_{a=1}^{8} A^a_\mu(x)\lambda_a. \tag{1.2}$$

The gauge field $A_\mu(x)$ at the space-time point x can be considered as having eight degrees of freedom in color space with eight components: $A^a_\mu(x)$, a=1,2, ...,8. This color potential is introduced to make the Lagrangian invariant under rotations of the color co-ordinate frame (three dimensional) at the same space-time point x (called local gauge invariance; local in space-time). The eight component field strength tensor is given by

$$F^a_{\mu\nu} = \partial_\mu A^a_\nu - \partial_\nu A^a_\mu + g f_{abc} A^b_\mu A^c_\nu, \tag{1.3}$$

where f_{abc} are the antisymmetric structure constants for the Lie group SU(3). The product $F^a_{\mu\nu} F^{\mu\nu}_a$ is also invariant under a local color gauge transformation. The run-

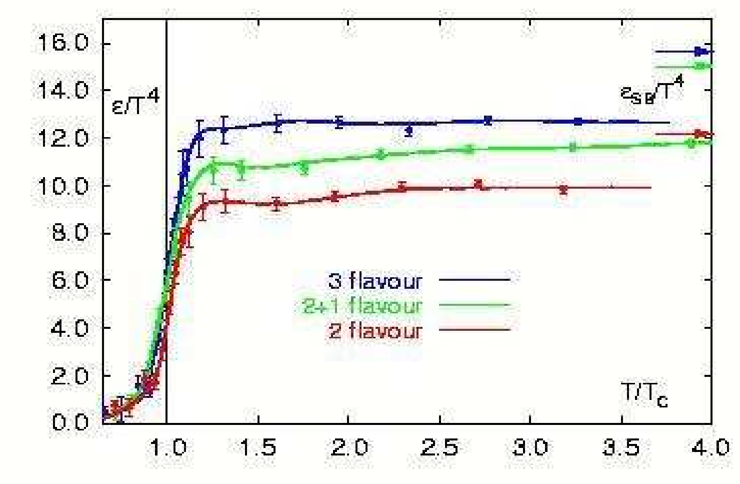

Figure 1.2: Lattice calculations of the dependence of the density versus temperature.

ning coupling constant for strong interaction behaves like

$$\alpha_s(Q^2) = \frac{1}{\beta_0 ln(Q^2/\Lambda^2)} \tag{1.4}$$

where Λ is a dimensional parameter introduced in the renormalization process and the energy scale where $\alpha_s(Q^2)$ diverges to infinity. β_0 is a constant that depends on the number of active quark flavors. As shown in Fig. 1.1, the above formula explains the "asymptotic freedom" and "quark confinement" nature of QCD.

What is the energy density and temperature required for the formation of QGP? The energy density in a nucleon [4] is

$$\rho_E^N = \frac{m_N}{\frac{4}{3}\pi R^3} \simeq 0.5\ GeV/fm^3, \tag{1.5}$$

with $R \simeq 0.8 fm.$. In nucleus-nucleus collisions at relativistic energies, large density results from heating through individual NN interactions as well as the compression of the nuclei when traversing one another. In the collision of two nuclei at this energy, a quark will not be associated with its parent nucleon if the energy per quark in the struck part (plasma) exceeds the energy per quark inside a free nucleon. Therefore, quarks and gluons can't be identified anymore with individual nucleons and we will

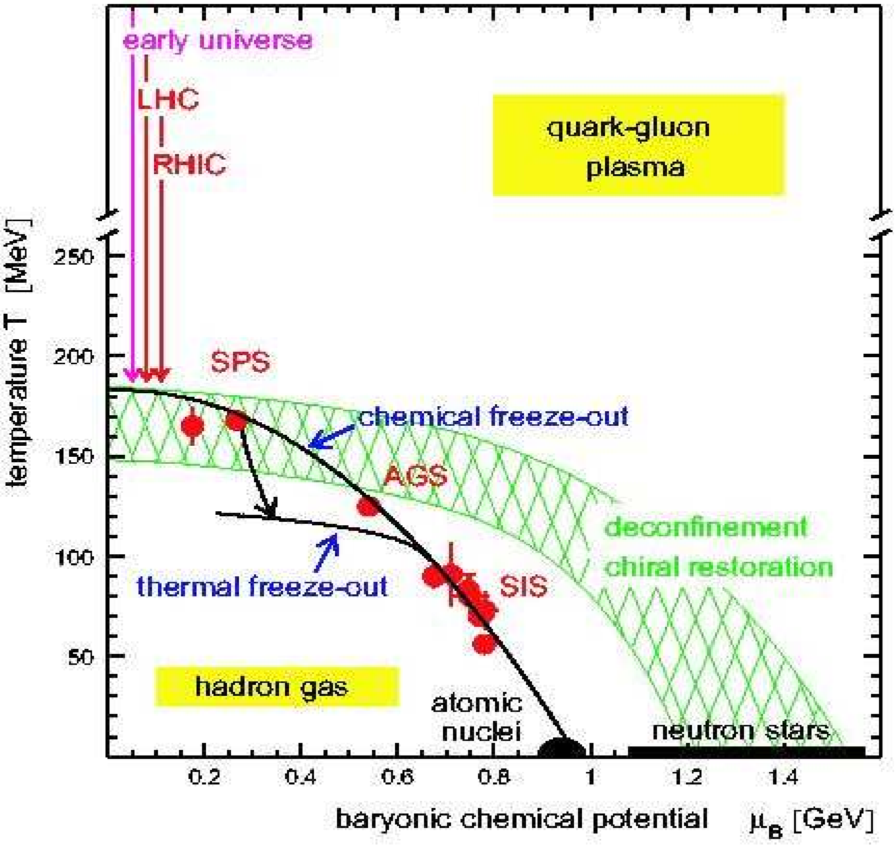

Figure 1.3: The phase diagram of hadronic matter, showing hadron gas and QGP regions. The temperature T and the baryochemical potential μ_B data are derived from particle yield ratios. The solid curve through the data points represents the chemical freeze-out of hadronic-matter. Figure reference [2].

have a transition to partonic matter called QGP. According to this estimate, the energy density for QGP formation should be more than $0.5 GeV/fm^3$ ($\sim 3-4$ times the energy density corresponding to normal nuclear matter).

Lattice QCD calculations, considering two light quark flavors (Fig.1.2), predict a phase transition from a confined state of hadronic matter to a deconfined state of quarks and gluons (QGP), at a temperature around $\sim 150-200$ MeV [3]. As shown in the phase diagram (Fig.1.3), the phase transition is expected to take place at either high temperature or at large baryon chemical potential. The figure shows regions probed by different beam energies as have been obtained from various heavy ion accelerators. The non-zero baryon chemical potential and the high temperature region is the one probed by the highest energy collisions at the Relativistic Heavy Ion Collider (RHIC) located at the Brookhaven National Laboratory (BNL), USA. The region where $\mu_B = 0$ is believed to be one in which the early universe existed, and is also accessible to numerical simulations of QCD on a lattice.

The deconfinement in QGP is also explained by the Debye screening. The mesons and the hadrons could be defined as the bound states of q's and $\bar{q}$'s. In the presence of a large number of q's and $\bar{q}$'s, however the mutual $q-\bar{q}$ or $q-q$ interactions are screened and weakened. This is analogous to the case corresponding to the screening of Coulomb interaction in the presence of large number of electrons. When the temperature is increased, the number of q's and $\bar{q}$'s increases and, consequently, the screening radius decreases. At sufficiently high temperature, if the screening radius becomes shorter than the hadron radius itself, then the $q-\bar{q}$ system can no longer be bound and thus, is deconfined. This is also the reason, why the system is called a plasma.

QCD predicts the existence of a Quark-Gluon-Plasma [5, 6] at extreme nuclear densities or at extremely large temperature. In the new phase, hadrons dissolve, strong interactions become very weak and an ideal color-conducting plasma of quarks and gluons is formed. In QGP, the long range color force is Debye screened due to collective effects in the same way as it happen in the case of electromagnetic plasma. Thus the quarks in QGP can only interact via a short-range effective potential and they become almost free and deconfined. Although the quarks can still be sensitive to the perturbative part of the interaction, non-perturbative effects almost disappear. One can think heuristically of weak- and strong-coupling domains of QCD as two phases: the high energy phase of color-conducting QGP and the low energy phase of color insulators i.e. hadrons [7].

Ultra relativistic nuclear collisions have given us a method to search for QGP formation in the laboratory [8]. A large number of particles produced in a finite volume of the collision suggests the existence of a large energy density.

1.3 Possible Signatures of QGP

The central problem connected with ultra relativistic heavy ion collisions is to search for the evidence for the QGP formation and thus to deduce the energies, entropies and temperatures of the system formed in central collisions. Although the existence of a hot and dense phase of QCD is of no doubt, its observability in nuclear collisions is a matter of intense debate. As the hot and dense matter is initially formed for a brief time interval, it subsequently expands and cools substantially beyond the confining point T_c before freeze-out, when the particles leave the fireball and reach the detectors. The problem becomes more intriguing because hot, excited hadronic matter essentially consists of a quark-gluon system (QGS). After a phase transition, it turns to QGP involving collective behavior. So the observation of QGP essentially means making a distinction between signals arising from QGP and hot QGS respectively. There are many proposed possible experimental signatures of QGP. These range from plotting of $< p_T >$ as a function of particle multiplicity to more current searches for modification of particle properties (enhancement, suppression, medium-induced modification of mass or width) and statistical studies of fluctuations in observables such as multiplicity, charge, transverse energy, E_T etc. on an event-by-event basis. There are probes which give information about "surface effects" like p_T distributions of hadrons, strangeness production and particle interferometry which reveal final state information. Some other probes deal with deeper "volume effects" which are sensitive to early times after the collision. These include hard processes (large momentum transfer) like heavy flavor production $(J/\psi, D-mesons, \Upsilon)$, jets and high p_T particle

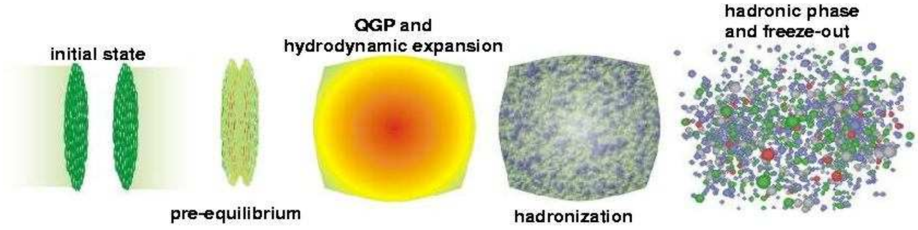

Figure 1.4: Cartoon showing the initial state of ultra-relativistic nuclear collision and time evolution of the fireball.

production. However, the emphasis has been mainly on the volume probes which provide direct information from the hot and dense phase of the reaction and are not influenced much by the number of hadrons produced in the collision. But it is essential to study the modification of the proposed signals by non-QGP, nuclear effects. It's is also worth noting that all the different results must be investigated as a function of the associated particle multiplicity or equivalent probe giving information on global characteristics.

One would also try to understand the onset of all the signals in terms of different handles available to us. Experimentally we can vary the collision centrality (by selecting multiplicity or transverse energy), collision species (a controlled variation of system size) and the center of mass energy. The experimental data at the end helps to constrain the theoretical model parameters and inputs which include a) equation of state, b) expansion dynamics and collective flow, c) size and life time of the system for hydrodynamical models d) initial parton densities, e) parton mean-free path and cross-section, f) nuclear shadowing of initial parton distributions and g) the amount of parton energy loss in the plasma. We will discuss briefly some of the experimental signals which have been proposed to probe the matter created in heavy ion collisions [7, 9, 10].

1.3.1 Strangeness Enhancement

Strangeness enhancement is one of the important probes of QGP formation [11, 12]. There is no strangeness in the initial state of the collision- the strangeness (which is created during the collisions) thus provides information on the reaction dynamics. Moreover, this creates a link between the partonic and hadronic phases. In hadronic reactions, the production of particles containing strange quarks is normally suppressed due to the high mass of strange quark ($m_s \simeq 60-170$ MeV) compared to the same for u and d quarks. In the presence of QGP, the temperature is of the order of s-quark mass and the rapid filling of the phase space available for u and d quarks should favor the production of $s\bar{s}$ pairs in interactions of two gluons ($gg \rightarrow s\bar{s}$) [11, 12]. This should be reflected in an enhanced production of multi-strange baryons and strange anti-baryons in the QGP phase compared to a purely hadronic scenario, at the same temperature. The important observables in this respect are the yields of strange as well as multi-strange hadrons and the ratios of the number of strange hadrons to non-strange hadrons produced in the collision process. To account for incomplete chemical equilibration, a strangeness fugacity γ_s is introduced in a thermo-chemical approach. The particle ratios can be calculated assuming either a hadron gas or a QGP scenario and a comparison can be made of the values thus extracted in conjunction with other model parameters such as T, μ_B and entropy. As the strange hadrons interact strongly, their final state interactions must be modeled in details before predictions and comparisons of strange particle yields can be made [13]. The enhancement in the K/π, ϕ/ω, $\bar{\Lambda}/\Lambda$ and $\bar{\Xi}/\Xi$ ratios are the experimental observables in this sector [7].

Point to note here is kaons account for about 70% of overall strangeness production. The enhancement in K/π ratio from pp, pA to AA is very distinct (factor ~ 2). The fact that strangeness/entropy ratio stays the same for all three systems (S+S, S+Ag and Pb+Pb), suggests that the system has reached some kind of saturation in the s and $\bar{s}$ yields in S+S reaction. This seems to rule out the possible interpretation of strangeness enhancement as a consequence of hadronic re-interactions [14].

1.3.2 J/ψ Suppression and Open charm Enhancement

J/ψ suppression was suggested by Matsui and Satz [15] as a clean signal of QGP. The color charge of a quark in QGP, is screened due to the presence of quarks, anti-quarks and gluons in the plasma. If we place a J/ψ particle, which is a bound state of charm quark c and a charm anti-quark $\bar{c}$, the Debye screening will weaken the interaction of c and $\bar{c}$. Furthermore, in QGP the quarks and gluons are deconfined and the string tension between c and $\bar{c}$ vanishes. In QGP, the screening radius r_D becomes less than the binding radius r_H. Because of these two effects a J/ψ particle placed in QGP at high temperature will dissociate leading to suppression of its production in high energy nucleus-nucleus collisions.

To understand the effect of QGP on a J/ψ particle, let's consider J/ψ as a two body system of a charm quark interacting with a charm anti-quark in the absence of QGP. We place the c quark with a color charge $q > 0$ at the origin and the $\bar{c}$ quark with a color charge $-q$ at $\mathbf{r}$. The color potential between c and $\bar{c}$ is given by the Coulomb potential

$$V_0(\mathbf{r}) = \frac{q}{4\pi r} \tag{1.6}$$

There is also a confining linear potential between c and $\bar{c}$ which increases with their separation,

$$V_{linear}(\mathbf{r}) = kr, \tag{1.7}$$

where k is the string tension coefficient. The potential energy for the $c\bar{c}$ system is

$$V(\mathbf{r}) = (-q)\frac{q}{4\pi r} + kr, \tag{1.8}$$

The Hamiltonian for the $c\bar{c}$ system is given by

$$H = \frac{\mathbf{p}^2}{2\mu} - \frac{\alpha_{eff}}{r} + kr, \tag{1.9}$$

where $\mu = m_c/2$, is the reduced mass of the $c\bar{c}$ system and $\alpha_{eff} = q^2/4\pi$.

Now, if we put the $c\bar{c}$ system in QGP, the system will be affected in the following way. The string tension depends on the temperature. The finite temperature of the quark matter therefore alters the string tension coefficient k between c and $\bar{c}$. Secondly, the presence of quark matter also leads to rearrangement of the densities of quarks, anti-quarks and gluons around c and $\bar{c}$. This rearrangement leads to the screening of c from $\bar{c}$ and vice versa. As a consequence, the interaction between c and $\bar{c}$ is modified from a long range Coulomb interaction Eq (1.6) into a Yukawa-type short range (given by Debye screening length Λ_D) interaction.

Quark confinement occurs when the string tension doesn't vanish. However, the absence of the string tension doesn't automatically mean that c and $\bar{c}$ can't form a bound state. They remain interacting with each other with the Coulomb interaction $-\alpha_{eff}/r$ which in tern is modified by the Debye screening. However, at very high temperature, the screening is so high that c and $\bar{c}$ hardly form any bound state and the $c\bar{c}$ systems dissociate ($\Lambda_D \propto \frac{1}{T}$). The c quark and $\bar{c}$ anti-quark subsequently hadronize by combining with light quarks and light anti-quarks to emerge as "open charm" mesons such as $D(c\bar{u}$, and $c\bar{d})$, $\bar{D}(\bar{c}u$ and $\bar{c}d)$, $D_s(c\bar{s})$, and $\bar{D}_s(\bar{c}s)$. Hence in nucleus-nucleus collisions, in case of the formation of a QGP phase, J/ψ production will be suppressed which will result in the enhanced production of open charm states.

There have been several experimental investigations to study J/ψ production in high energy heavy-ion collisions both at CERN (by NA38 and NA50 collaborations) [16, 17, 18, 19] and RHIC [20, 21]. There are also nuclear effects, such as the break up of J/ψ by hadronic co-movers, which can also suppress the measured J/ψ cross-section in nucleus-nucleus collisions [22].

1.3.3 Jet Quenching

Jets produced by high-energy quarks and gluons in ultra-relativistic heavy ion collisions can also provide a potential probe for the formation of a QGP. High energy partons coming from the initial hard collisions lose energy by traversing through the dense matter. This energy loss is greater in AA collisions, as compared to pp and pA collisions [23]. This phenomenon is called jet quenching. Jet quenching results from the energy loss $(-dE/dx)$ of a high-p_T parton as it propagates in the dense matter. In case of hadronic matter the partons are decelerated due to the string tension $((-dE/dx)_{had} \simeq 1)$ GeV/fm, whereas in a QGP, they lose energy by collisions with the thermal quarks and gluons (elastic scattering) and by bremsstrahlung radiation.

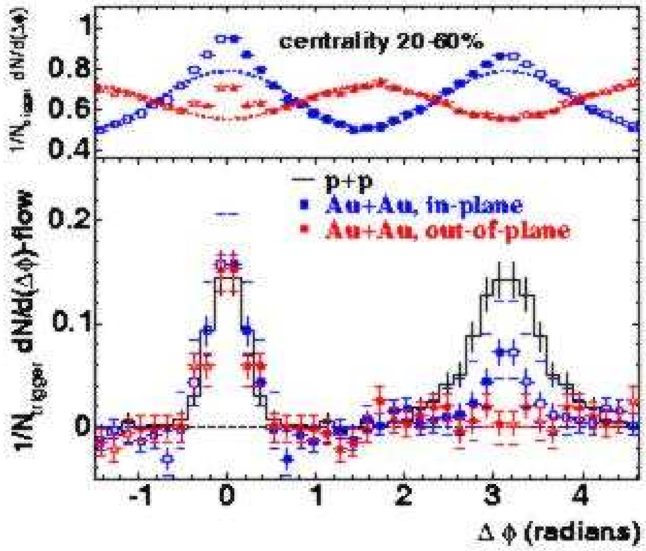

Figure 1.5: Upper panel: Azimuthal distributions of associated particles, for in-plane trigger particles (squares) and out-of-plane trigger particles (triangles) for Au+Au collisions at centrality 20% – 60%. Open symbols are reflections of solid symbols around $\Delta\phi = 0$ and $\Delta\phi = \pi$. Elliptic flow contribution is shown by dashed lines. Lower panel: Distributions after subtracting elliptic flow, and the corresponding measurement in $p + p$ collisions (histogram) Fig. Ref. [24].

It appears that when both the contributions are added, the stopping power of QGP is comparable to that of hadronic matter. However the radiative energy loss is proportional to the square of Debye momentum ($\mu_D \approx \lambda_D^{-1}$) which, according to lattice calculations, decreases rapidly close to the phase transition. Thus in the vicinity of the deconfinement transition, there might be a region where the stopping power of strongly interacting matter decreases with growing energy density. Therefore in the mixed phase, in which the system is expected to spend most of its time, variations of jet quenching may provide a signature for the phase transition [7]. In addition a quark or gluon jet traversing through a dense medium will also be deflected due to the scattering from the constituents of the QGP and also the hadronic matter. This angular deflection will introduce jet acoplanarity or an azimuthal asymmetry. One can then perform the angular correlations among high-p_T particles to study the energy loss effects of the partons in the medium. Fig. 1.5 shows the STAR collaboration measurement of back-to-back (around $\Delta\phi = \pi$) correlations in Au+Au collisions. In-plane trigger particles (high-p_T) are suppressed compared to $p+p$ and even more suppressed for out-of-plane trigger particles. This shows jet quenching in $Au + Au$ collisions compared to $p+p$ collisions.

The nuclear effects that influence strongly the absolute yield of the moderate-p_T and high-p_T hadrons are gluon shadowing and jet quenching. Both the effects are of fundamental interest as they pertain to nuclear structure at the partonic scale and the energy-loss mechanism in dense matter. To measure these nuclear effects in relativistic heavy ion collisions, a comparison of hadron p_T spectrum (from nucleus-nucleus collisions) with that of pp collisions at the same energy is needed. A properly defined ratio of the two is called "nuclear modification factor" and is defined as,

$$R_{AB}(p_T) = \frac{d^2N/dp_T d\eta}{T_{AB} d^2\sigma^{pp}/dp_T d\eta}, \tag{1.10}$$

where, $d^2N/dp_T d\eta$ is the differential yield per event in the nuclear collision A+B, $T_{AB} =< N_{bin} > /\sigma^{pp}_{inel}$ describes the nuclear geometry, and $d^2\sigma^{pp}/dp_T d\eta$ for $p+p$ inelastic collisions is determined from the measured $p+p$ differential cross-section. In the absence of nuclear effects such as shadowing, the Cronin effect, or gluon saturation, hard processes are expected to scale with the number of binary collisions and $R_{AB}(p_T) = 1$.

The high-p_T hadron suppression in central Au+Au collisions also could be studied by comparing the hadron spectra in central and peripheral Au+Au collisions. It's measured by the observable, R_{CP}, defined by,

$$R_{CP}(p_T) = \frac{< N_{bin}^{peripheral} > d^2N^{central}/dp_T d\eta}{< N_{bin}^{central} > d^2N^{peripheral}/dp_T d\eta}, \tag{1.11}$$

1.3.4 Photons and Dileptons

Photons and dileptons are regarded as the "penetrating" probes of a hot and dense matter such as QGP because they are produced in the early thermal stage of the process and they are not affected by the subsequent hadronization of the system. They interact only electromagnetically and their mean free paths are much larger than the transverse size of the collision volume created in nuclear collisions. As a result, high-energy photons and dileptons, produced in the interior of the plasma, usually pass through the surrounding matter without interacting, carrying information directly from wherever they were formed to the detector. Contrary to this, the situation for hadronic particles are completely different, as their abundances and momentum distributions are changed by re-scattering in the expansion phase. Dileptons and photons are thus called "thermometers", because they can reveal information about the temperature of the primordial matter.

The main difficulty in reading out the history of the final-state evolution from the measured photon and dilepton spectra is the existence of several sources which produce photons and dileptons at all stages of the fireball creation and evolution. In the mass spectrum, single leptons are not considered because weak decays of hadrons (especially strange and charm hadrons) produce a strong background. If one considers mass spectrum of opposite sign dileptons, several vector mesons are seen to appear in the spectrum because most of them decay into lepton pairs. They essentially give information about expansion dynamics as well as the effects of the dense medium on the hadrons. Hence in order to study dilepton signals, one should (1) have a good understanding of the thermal production rate of dileptons, and (2) compare these rates with other sources. The most significant channel for the production of dileptons in the QGP sector is the annihilation of quark-antiquark pairs. In the hadronic sector, it is, $\pi^+\pi^-$ annihilation. Other sources of dilepton production are, $\pi N \rightarrow l\bar{l} + \chi$ and $N\bar{N} \rightarrow l\bar{l} + \chi$. The final signal is a mixture of thermal emission of lepton pairs from the plasma and the later hadron gas, with a background from Drell-Yan processes in which a quark and anti-quark pair from the colliding systems annihilates. Charm production also provides a potential background because charm decays possess a large semileptonic branching ratio [7]. Hence, the dilepton signal in the invariant mass spectrum is a convolution of several such complicated backgrounds on top of it. A study of the p_T dependence of various mass windows might perhaps help to disentangle the different contributions to the spectrum.

It is shown in Ref.[25], that the ratio of dilepton production rate from the hadronic sector to that of from the QGP, becomes independent of the chemical potential and temperature if the plasma temperature goes beyond $T_c > 200$ MeV. It is also proposed [26] that the ratio of the dilepton rapidity density to the square of the charged pion rapidity density may provide a measurement of phase transition temperature, provided we get some abrupt change in the slope of the ratio.

Hard and direct photons from the QGP can arise mainly from Compton scattering ($qg \rightarrow q\gamma,\ \bar{q}g \rightarrow \bar{q}\gamma$) and annihilation ($q\bar{q} \rightarrow g\gamma$). Unfortunately, a thermal hadron gas with the Compton scattering reaction $\pi\rho \rightarrow \gamma\rho$ and pion annihilation $\pi\pi \rightarrow \gamma\rho$ have been shown to shine as bright as a QGP [27]. There are also other channels of photon production like, $\pi^0 \rightarrow \gamma\gamma,\ \omega \rightarrow \pi^0\gamma,\ \rho^0 \rightarrow \pi^+\pi^-\gamma$. However, clear signal of photons from a very hot QGP could be visible at p_T in the range 2-5 GeV/c [28, 29]. However, the flow effects can prevent a direct identification of the temperature and the slope of p_T distribution. WA98 has observed a direct photon signal in Pb+Pb collisions at SPS [30]. Compared to the results to pA data, there seems to be an enhancement for central collisions, suggesting a modification of the photon production mechanism. There are also measurements on direct photon at RHIC [31, 32].

There are suggestions [27] to measure T_c by the photons in the p_T range from 1 to 3 GeV. The technique used is simply to fit the p_T distribution with a thermal distribution- the temperature from the fit is approximately equal to the transition temperature.

1.3.5 Medium Effects on Hadron Properties

The widths and masses of the ρ, ω and ϕ in the dilepton pair invariant mass spectrum are sensitive to medium-induced changes, especially to possible drop of vector meson masses preceding the chiral symmetry restoration transition. The CERES data from S+Au and Pb+Au collisions at SPS showed an excess of dileptons in the low-mass region $0.2 < M < 1.5\ GeV/c^2$, relative to pp and pA collisions [33, 34]. Although the CERES data can be explained by a hydrodynamic approach assuming the creation of a QGP [35], alternative scenarios have also provided explanations. These have included for instance, microscopic hadronic transport models incorporating mass shifts of vector mesons and calculations involving in-medium spectral functions (coupling the ρ with nucleon resonances) without requiring a shift in the ρ mass [36]. When the life time of a resonance particle is comparable with the evolution time scale of the phase transition in nucleus-nucleus collisions, the measured properties (mass, width, branching ratio, yield and p_T-spectra) associated with the resonances will depend on the collision dynamics and chiral properties of the medium at high energy density and temperature [37].

1.3.6 Equation of state and Flow

The system formed in heavy ion collision, although small in size, is sufficiently large for statistical physics to be applicable. The thermodynamical properties of the system in statistical equilibrium are described by an equation of state (EoS). One of the important goals of heavy-ion program is to look for the phase transition between hadronic matter and the QGP. The order of the phase transition is not clear till date. Lattice gauge theory calculations using three or more flavors show the phase transition to be first order, while calculations with two light quarks lead to a second order phase transition. For first order phase transition, the pressure remains constant in the region of phase co-existence. This results in vanishing velocity of sound $c_s = \sqrt{\partial p/\partial \epsilon}$. The expansion of the system or collective flow is driven by the pressure gradient, therefore expansion depends crucially on c_s^2. Matter in the mixed phase expands less rapidly than a hadron gas or a QGP at the same energy density and entropy. In case of rapid changes in the EoS without phase transition, the pressure gradients are finite, but still smaller than for an ideal gas EoS, and therefore the system expands more slowly [38, 39]. This reduction of c_s^2 in the transition region is commonly referred as “softening” of EoS. The respective region of energy densities is called a soft region. Here the flow will temporarily slow down (or possibly even stall). Consequently a time delay is expected in the expansion of the system. This prevents the deflection of spectator matter (the bounce-off) and, therefore, causes a reduction of the directed transverse flow in semi-peripheral collisions. The softening of EoS should be observable in the excitation function of the transverse directed flow of baryons.

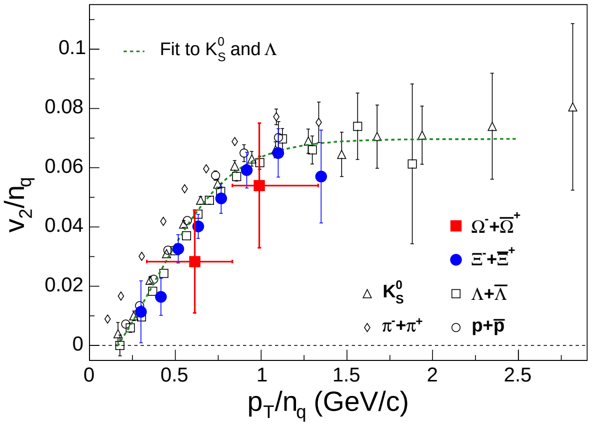

Figure 1.6: (color online). Number of quarks (n_q) scaled v_2 as a function of scaled p_T for $\Xi^- + \bar{\Xi}^+$ (solid circles) and $\Omega^- + \bar{\Omega}^+$ (solid squares). Same distributions also shown for $\pi^+ + \pi^-$ (open diamonds), $p + \bar{p}$ (open triangles), K_s^0 (open circles) and $\Lambda + \bar{\Lambda}$ (open squares). All data are from 200 GeV Au+Au minimum-bias collisions. The dashed line is the scaled result of the fit to K_s^0 and Λ. Fig. Ref. [51].

Due to it's direct dependence on the EoS, $P(\rho, T)$, flow excitation functions can provide unique information about phase transition: the formation of abnormal nuclear matter, e.g., yields a reduction of the collective flow [40]. A directed flow excitation function as a signature of phase transition into the QGP has been proposed by several authors [41, 42]. In experiments, for peripheral nucleus-nucleus collisions, an event in the plane perpendicular to the beam axis exhibits an azimuthal anisotropy in the particle distributions. this happens because the pressure gradient drives the emission of particles in the peripheral collisions. The initial state spatial anisotropy is converted to the final state momentum anisotropy. The azimuthal distribution of particles in momentum space can be expanded in terms of a Fourier series

$$E\frac{d^3N}{dp^3} = \frac{1}{2\pi}\frac{d^2N}{p_T dp_T dy}(1 + \sum_{n=1}^{\infty} 2v_n cos[n(\phi - \psi_r)]) \tag{1.12}$$

where, ψ_r denotes the reaction plane angle. The Fourier coefficients v_n stands for the nth harmonic of the event azimuthal anisotropy. The first harmonic coefficient v_1 is called *directed flow* and the 2nd harmonic coefficient v_2 is called the *elliptic flow*.

There are several flow measurements at RHIC, taking identified charge particles and multi-strange baryons etc. [48, 49, 50]. Multistrange baryons, due to their large mass and small cross sections should be less sensitive to hadronic re-scattering in the later stages of the collision and therefore a good probe of the early stage of the collision. Their transverse flow would then primarily reflect the partonic flow. Fig. 1.6 shows the STAR measurement of n_q-scaled (number of constituent quarks) v_2 versus the n_q-scaled p_T distribution. The constituent quark scaling reflects the partonic collectivity at RHIC. Furthermore, this supports the idea that the partonic flow of s quark is similar to that of u, d quarks.

1.3.7 Global Variables

Global observables like transverse energy E_T, particle multiplicities (N_γ, N_{ch} etc.), p_T-spectra of the produced particles and their pseudo-rapidity distributions ($dE_T/d\eta$, $dN/d\eta$), with mass number and beam energy provide insight about the dynamics of the system and regarding the formation of QGP [64, 43]. It is also proposed that the correlation of transverse momentum p_T and the multiplicity of the produced particles may serve as a probe for the EoS of hot hadronic matter [44]. According to Landau's hydrodynamic model [45], the rapidity density (dN/dy), reflects the entropy and the mean transverse momentum ($< p_T >$) the temperature of the system. Except at the phase transition points, the rapidity density linearly scales with $< p_T >$. If the phase transition is of first order, then the temperature remains constant at the coexistence of the hadron gas and the QGP phase, thereby increasing the entropy density. So $< p_T >$ will show a plateau with increase of entropy. Hence the global observables like dN/dy and $< p_T >$ will give indication of QGP phase and the order of phase transition. $dE_T/d\eta$ gives the maximum energy density produced in the collision process which is necessary to understand the reaction dynamics. The formation of QGP may also change the shape of the pseudo-rapidity distribution [46, 47].

The event multiplicity distribution gives information of the centrality and energy density of the collision. The scaling of multiplicity with number of participant nucleons (N_{part}) reflects the particle production due to soft processes (low p_T). Whereas, at high energy when hard processes (high-p_T) dominate, it's expected that the multiplicity will scale with number of elementary nucleon-nucleon collision (N_{coll}). There are models [52] to explain the particle production taking a linear combination of N_{part} and N_{coll} (called a two-component model).

1.3.8 Observable Fluctuations

Lattice QCD calculations find a phase transition in strongly interacting matter which is accompanied by a strong increase of the number of effective degrees of freedom [53, 54]. Although, the nature and order of the phase transition is not known very well, lattice calculations suggest that QCD has a weak first-order transition provided that the strange quark is sufficiently light [53, 54], that is for three or more massless flavors. However, when the quark flavors become massive, the QCD transition changes to a smooth cross over.

Phase transition being a critical phenomenon, is associated with divergence of susceptibilities and hence fluctuations in corresponding observables. Hence, observable fluctuations could be used as probes of deconfinement phase transitions.

Fluctuations are very sensitive to the nature of the phase transition. First-order phase transition is expected to lead to large fluctuations due to droplet formation or more generally density or temperature fluctuations. In case of a second-order phase transition the specific heat diverges, and this has been argued to reduce the fluctuations drastically if the matter freezes out at the critical temperature. Even if the transition is not of first order, fluctuations may still occur in the matter that undergoes a transition. The fluctuations may be in density, chiral symmetry, strangeness or other quantities and show up in particle multiplicities. The "anomalous" fluctuations depend not only on the type and order of the phase transition, but also on the speed by which the collision zone goes through the transition, the degree of equilibration, the subsequent hadronization process, the amount of re-scattering between hadronization and freeze-out [55].

There have been efforts to use observable fluctuations like, ratios of charged particles [56, 57], baryon number multiplicity [58], net charge [59], mean p_T [60], transverse energy [61], strangeness [62], isospin [63] etc., to probe the deconfinement phase transition.

It is necessary to understand the role of statistical fluctuations, in order to extract new physics associated with fluctuations. The sources of these fluctuations include impact parameter fluctuations, fluctuations in the number of primary collisions and in the results of such collisions, fluctuations in the relative orientation during the collision of deformed nuclei, effects of re-scattering of secondaries and QCD color fluctuations.

1.4 Estimation of Initial Energy Density in Heavy-Ion Collisions

In any frame where the two incoming nuclei have very high energies, the region when/where the nuclei overlap will be very thin in the longitudinal direction and very short in duration. In this scenario, it's fair to describe all secondary produced particles as having been radiated out from a very thin "disk" and that they are all created at essentially at same time. This is the Bjorken hydrodynamic picture [64] of nucleus-nucleus collision.

Once the beam "pancakes" recede after their initial overlap, the region between them is occupied by secondaries at intermediate rapidities. We can calculate the local energy densities of these created particles, if we assume that the secondaries can be considered to be formed at some proper time τ_{Form}, after they are radiated out from the thin source disk.

Our region of interest, in any frame will be a slab perpendicular to the beam direction, with longitudinal thickness dz, with one face of the "source" plane in this frame, and the transverse overlap area A. The region described here corresponds to half the shaded region shown in Fig. 1.7. Since $\beta_{||} \simeq 0$ for particles near the source location, this is an appropriate region over which we can calculate a meaningful energy ' density. At time $t = \tau_{Form}$, this volume will contain all the (now-formed) particles with longitudinal velocities $0 \leq \beta_{||} \leq dz/\tau_{Form}$ (since we assume particles

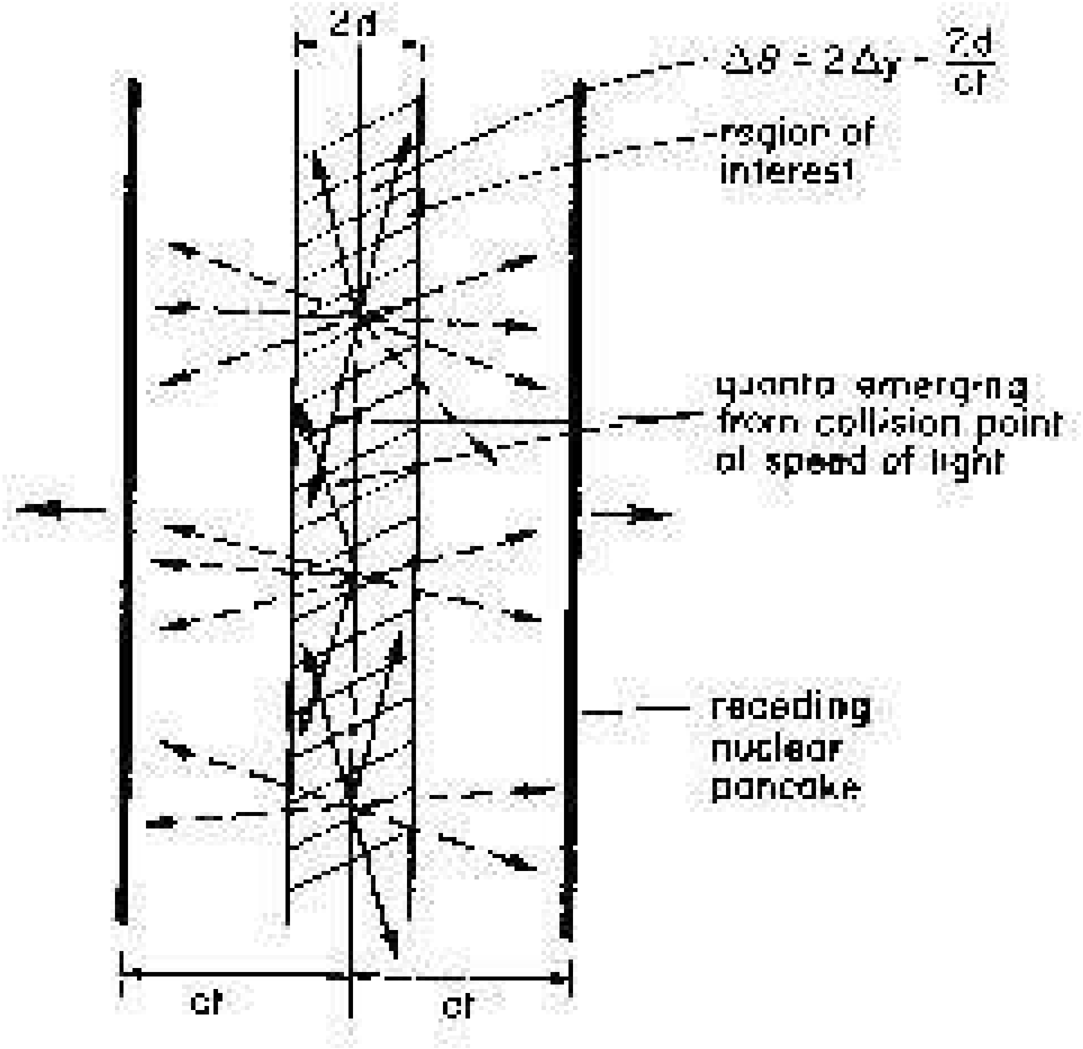

Figure 1.7: Geometry for the initial state of centrally produced plasma in nucleus-nucleus collisions. This picture is valid in any frame in which the incoming nuclei have very high energies and so are Lorentz contracted.

can't scatter before they are formed!). Then we can write this number of particles as $dN = (dz/\tau_{Form})\frac{dN}{d\beta_{||}}$, or equivalently $dN = (dz/\tau_{Form})\frac{dN}{dy}$, where y is longitudinal rapidity, since $dy = d\beta_{||}$ at $y = \beta_{||} = 0$. If these particles have an average total energy $< m_T >$ in this frame ($E = m_T$ for particles with no longitudinal velocity), then the total energy divided by the total volume of the slab at $t = \tau_{Form}$ is

$$\langle\epsilon(\tau_{Form})\rangle = \frac{dN < m_T >}{dzA} = \frac{dN(\tau_{Form})}{dy}\frac{< m_T >}{\tau_{Form}A} = \frac{1}{\tau_{Form}A}\frac{dE_T(\tau_{Form})}{dy}, \qquad (1.13)$$

where, we have equated $\frac{dE_T}{dy} =< m_T > \frac{dN}{dy} \approx< m_T > \frac{3}{2}\frac{dN_{ch}}{dy}$ and emphasized that Eq. (1.13) is true for the transverse energy density present at time $t = \tau_{Form}$. The factor 3/2 compensates for the neutral particles.

Eq. (1.13) is referred as *Bjorken energy density*, ϵ_{B_j}. It is a valid measure of peak energy density in created particles, on very general grounds and in all frames, as long as two conditions are satisfied: (1) A finite formation time τ_{Form} can meaningfully be defined for the created secondaries; and (2) The thickness/"crossing time" of the source disk is small compared to τ_{Form}, that is, $\tau_{Form} >> 2R/\gamma$. Here R is the rest-frame radius of the nucleus and γ is the Lorentz factor. In particular, the validity of Eq. (1.13) is completely independent of the shape of the $dE_T(\tau_{Form})/dy$ distribution to the extent that $\beta_{||}$ is infinitesimally small in a co-moving frame; a plateau in dE_T/dy is not required. For practical purposes at RHIC, we will consider condition (2) above to be satisfied as long as $\tau_{Form} > 2R/\gamma$ is true.

Historically, ϵ_{B_j} has been calculated using the final state dE_T/dy and simply inserting a nominal value of 1 fm/c for τ_{Form}. In addition, fixed target experiments have been using $dE_T/d\eta$ as an estimate for dE_T/dy, which is a good approximation for these experiments. For collider experiments, a correction is made for the Jacobian $dy/d\eta$: ($\sqrt{1 - m^2/ < m_T >^2}\frac{dN}{dy} = J\frac{dN}{dy} = \frac{dN}{d\eta}$). However, we can't take ϵ_{B_j} as an exact estimate of energy density without some justification for the value of 1 fm/c taken for τ_{Form}. Hence, we term it as $\epsilon_{B_j}^{Nominal}$. An indication of potential problems with this choice arises immediately when considering AGS Au+Au and SPS Pb+Pb collisions, where the center of mass "crossing times" $2R/\gamma$ are 5.3 fm/c and 1.6 fm/c respectively, which implies that this choice for $\tau_{Form} = 1$ fm/c actually violates the validity condition $\tau_{Form} > 2R/\gamma$ we set for the use of Eq.(1.13). So we will deprecate the use of $\epsilon_{B_j}^{Nominal}$ as a quantitative estimate of actual produced energy density and instead treat it only as a compact way of comparing $dE_T/d\eta$ measurements across different systems, centralities and beam energies.

1.4.1 Realistic τ_{Form} and ϵ_{B_j} estimates

Is it possible to justify a better estimate for τ_{Form}? From general quantum mechanical grounds, in a frame where it's motion is entirely transverse, a particle of energy m_T can be considered to have "formed" after a time $t = \hbar/m_T$ since it's creation in that frame. To estimate the average transverse mass, we can use the final-state $dE_T/d\eta$ to estimate $dE_T(\tau_{Form})/dy$ and, correspondingly, use the final-state $dN/d\eta$ as an estimate for $dN(\tau_{Form})/dy$ to obtain

$$\langle m_T \rangle = \frac{dE_T(\tau_{Form})/dy}{dN(\tau_{Form})/dy} \simeq \frac{dE_T/d\eta}{dN/d\eta} \quad (Final\ state). \tag{1.14}$$

It has been observed experimentally that the ratio of final-state transverse energy density to charge particle density, each per unit pseudo-rapidity is constant at about 0.85 GeV for full energy central Au+Au collisions. This value is constant for a wide range of centrality and shows a very little change with beam energy, decreasing to 0.7 GeV, when $\sqrt{s_{NN}}$ is decreased by a order of magnitude down to 19.6 GeV. If we approximate $dN_{ch}/d\eta = (2/3)dN/d\eta$ in the final state, then Eq.(1.14) would imply $< m_T > \simeq 0.57$ GeV and corresponding $\tau_{Form} \simeq 0.35$ fm/c, a value shorter than the "nominal" 1 fm/c but still long enough to satisfy our validity condition $\tau_{Form} > 2R/\gamma$ at RHIC.

It's worth noting that the value of energy density obtained by Eq. (1.13) represents a conservative lower limit on the actual $< \epsilon(\tau_{Form}) >$ achieved at RHIC. This follows from two observations: (1) The final-state measured $dE_T/d\eta$ is a solid lower limit on the $dE_T(\tau_{Form})/dy$ present at formation time; and (2) The final-state ratio $(dE_T/d\eta)/(dN/d\eta)$ is a good lower limit on $< m_T >$ at formation time, and so yields a good upper limit on τ_{Form}. The justification of these statements could be realized as follows.

There are several known mechanisms that will decrease dE_T/dy as the collision system evolves after the initial particle formation, while no mechanism is known that can cause it to increase (for $y = 0$, at least). Therefore, it's final-state value should be a solid lower limit on its value at any earlier time. A list of mechanisms through which dE_T/dy will decrease after $t = \tau_{Form}$ includes: (i) The initially formed secondaries in any local transverse "slab" will, in a co-moving frame, have all their energy in transverse motion and none in longitudinal motion; if they start to collide and thermalize, at least some of their E_T will be converted to longitudinal modes in the local frame; (ii) Should rough local thermal equilibrium be obtained while the system's expansion will still primarily longitudinal, then each local fluid element will lose internal energy through pdV work and so its E_T will decrease; (iii) If there are pressure gradients during a longitudinal hydrodynamic expansion then some fluid elements may be accelerated to higher or lower rapidities; these effects are complicated to predict, but we can state generally that they will always tend to *decrease* dE_T/dy where it has its maximum, namely at $y = 0$. Given that we have strong evidence that thermalization and hydrodynamic evolution do occur in RHIC collisions, it's likely that all these effects are present to some degree, and so we should suspect that final-state $dE_T/d\eta$ is substantially lower than $dE_T(\tau_{Form})/dy$ at mid-rapidity.

Coming to the estimate of τ_{Form}, the assumption that $\tau_{Form} = \hbar / < m_T >$ can't be taken as exact, even if the produced particles' m_T's are all identical, since "formed" is not an exact concept. However, if we accept the basic validity of this uncertainty principle argument, then we can see that the approximation in Eq. (1.14) provides a lower limit on $< m_T >$. First, the numerator $dE_T/d\eta$ is a lower limit on $dE_T(\tau_{Form})/dy$, as above. Second, the argument is often made on grounds of entropy conservation that the local number density of particles can never decrease [65], which would make the final-state denominator in Eq. (1.14) an upper limit on its early-time value.

1.5 Event Simulation: HIJING 1.38

To understand the data in heavy-ion collision experiment, it is essential to compare the results with some model predictions. Taking all known physics processes starting from the particle production, their interactions till they are detected, the real experiment is simulated with the help of theoretical models. There are various models (called event generators) with their own physics goals and physics interactions, to study the particle production and the final state properties. The silent features of the model HIJING (Heavy Ion Jet INteraction Generator) [66], we have used for the present study are described below.

The HIJING is a Monte-Carlo event generator based on QCD-inspired models for multiple jet production to study the jets and associated particle production in high energy pp, pA and AA collisions. This model includes mechanisms such as multiple mini-jet production, soft excitation, nuclear shadowing of parton distribution functions and jet interaction in dense matter.

In relativistic-heavy ion collisions, mini-jets are expected to dominate transverse energy production in the central rapidity region. Particle production and correlation due to mini-jets must be investigated in order to recognize new physics of QGP formation. Due to the complication of soft interactions, mini-jet production can only be incorporated in a pQCD (perturbative Quantum Chromodynamics) inspired model. In HIJING, multiple mini-jet production is combined together with Lund-type model [67] for soft interactions, based on a pQCD-inspired model. Within this model, triggering on large-p_T jet production automatically biases toward enhanced mini-jet production. Binary approximation and Glauber geometry for multiple interaction are used to simulate pA and AA collisions. A parametrized parton distribution function inside a nucleus is used to take into account parton shadowing. Jet quenching is modeled by an assumed energy loss dE/dz of partons traversing the produced dense matter. A simplest color configuration is assumed for the multiple jet system and Lund jet fragmentation model used for the hadronization.

1.6 Thesis Organization

The work presented in this thesis is mostly related to the transverse energy measurement and fluctuation studies at $\sqrt{s_{NN}} = 62.4$ GeV Au+Au collisions. The data sample corresponds to that taken by the STAR detector in Run-IV. Details of the procedure of the estimation of transverse energy has been discussed along with the results. The thesis is organized as follows.

In Chapter 1, an overview of physics of quark gluon plasma and heavy ion collisions has already been given along with the results obtained so far. The signatures of QGP has been discussed as an introduction to the subject. In Chapter 2, the STAR detector system in RHIC experiment has been presented. Chapter 3 deals with the estimation procedure of transverse energy and a discussion on the results and observations. In Chapter 4, transverse energy fluctuation studies are presented. The summary and conclusion of the work is presented in Chapter 5. The method used for the estimation of systematic uncertainties is given in a separate chapter as an appendix to the thesis.

Bibliography

[1] J.C. Collins and M.J. Perry, *Phys. Rev. Lett.* **34** (1975) 1353.

[2] P. Braun-Munzinger, *Nucl. Phys.* **A681** (2001) 119c.

[3] F. Karsch, Lect.Notes Phys.**583** (2002) 209-249.

[4] F. Halzen and H.C. Liu, *Phys. Rev.* **D 25** (1982) 1842.

[5] E.V. Shuryak, *Phys. Rep.***61** (1980) 71.

[6] J. Cleymans, R.V. Gavai and E. Suhonen, *Phys. Rep.***130** (1986) 217.

[7] C.P. Singh, *Phys. Rep.***236** (1993) 147-224.

[8] K.Kajantie and L. McLerran, Annu. Rev. Nucl. Part. Sci.**37** (1987) 293.

[9] S.A. Bass *et al.*, *J. Phys. G: Nucl. Part. Phys.* **25** (1999) R1-R57.

[10] Berndt Muller, *Rep. Prog. Phys.***58** (1995) 611-636.

[11] J.Rafelski and B. Muller, *Phys. Rev. Lett.* **48** (1982) 1066.

[12] P.Koch, B. Muller and J.Rafelski, *Phys. Rep.***142** (1986) 165.

[13] M. Calderon de la Barca Sanchez, Ph.D. thesis, Yale University, USA, 2001.

[14] G. Odyniec, *Nucl. Phys.* **A681** (2001) 197c-204c.

[15] T. Matsui and H. Satz, *Phys. Lett.* **B178** (1986) 416.

[16] C. Baglin *et al.*, NA38 collaboration *Phys. Lett.* **B220** (1989) 471, *Phys. Lett.* **B251** (1990) 465, *Phys. Lett.* **B251** (1990) 472, *Phys. Lett.* **B255** (1991) 459, *Phys. Lett.* **B268** (1991) 453, *Phys. Lett.* **B270** (1991) 105, *Phys. Lett.* **B272** (1991) 449.

[17] M. Gonin *et al.*, *Nucl. Phys.* **A610** (1996) 404c.

[18] M.C. Abreu *et al.*, *Nucl. Phys.* **A661** (1999) 93.

[19] M.C. Abreu *et al.*, *Phys. Lett.* **B447** (2000) 28.

[20] R.L. Thews *et al.*, *Phys. Rev.* **C 63** (2001) 054905.

[21] S.S. Adler *et al.*, PHENIX collaboration *Phys. Rev.* **C 69** (2004) 014901.

[22] A. Capella *et al.*, *Phys. Rev. Lett.* **85** (2000) 2080.

[23] X.N. Wang and M. Gyulassy, *Phys. Rev. Lett.* **68** (1992) 1480.

[24] J. Adams *et al.*, STAR Collaboration *Phys. Rev. Lett.* **93** (2004) 252301.

[25] S. Raha and B. Sinha, *Int. J. Mod. Phys.***A6** (1991) 517.

[26] K. Kajantie *et al.*, *Phys. Rev.* **D 34** (1986) 2746.

[27] J. Kapusta *et al.*, *Phys. Rev.* **D 44** (1991) 2774, (erratum *Phys. Rev.* **D 47** (1993) 4171.

[28] D.K. Srivastava *et al.*, *Phys. Lett.* **B276** (1992) 285.

[29] M. Strickland, *Phys. Lett.* **B331** (1994) 245.

[30] M.M. Aggarwal *et al.*, WA98 Collaboration *Phys. Rev. Lett.* **85** (2000) 3595.

[31] S.S. Adler *et al.*, PHENIX Collaboration *Phys. Rev.* **D 71** (2005) 071102(R).

[32] S.S. Adler *et al.*, PHENIX Collaboration *Phys. Rev. Lett.* **94** (2005) 232301.

[33] T. Ullrich *et al.*, *Nucl. Phys.* **A610** (1996) 317c.

[34] A. Drees, *Nucl. Phys.* **A610** (1996) 536c.

[35] D.K. Srivastava *et al.*, *Nucl. Phys.* **A610** (1996) 350c.

[36] R. Rapp *et al.*, *Nucl. Phys.* **A617** (1997) 472.

[37] Z. Xu, *J. Phys. G: Nucl. Part. Phys.* **30** (2004) S325.

[38] J. Kapusta *et al.*, *Phys. Lett.* **B163** (1985) 253.

[39] H. v Gersdorff, *Nucl. Phys.* **A461** (1987) 251c.

[40] J. Hofmann *et al.*, *Phys. Rev. Lett.* **36** (1976) 88.

[41] H. Stocker and W. Greiner, *Phys. Rep.***137** (1986) 277.

[42] N.S. Amelin *et al.*, *Nucl. Phys.* **A544** (1992) 463c.

[43] M. Kataja *et al.*, *Phys. Rev.* **D 34** (1986) 2755.

[44] L. Van Hove, *Phys. Lett.* **B118** (1982) 138.

[45] L.D. Landau, *Izv. Akad. Nauk. SSSR Ser. Fiz.***17** (1953) 51; collected papers Ed. by D. Ter Haar (Pergamon, Oxford, 1965) p. 569.

[46] S. Sarkar *et al.*, *Phys. Rev.* **C 51** (1995) 318.[Erratum:ibid **C51** (1995) 2845.]

[47] A. Dumitru *et al.*, *Z. Phys.* **A353** (1995) 187.

[48] K.H. Ackermann *et al.*, STAR Collaboration *Phys. Rev. Lett.* **86** (2001) 402.

[49] C. Adler *et al.*, STAR Collaboration *Phys. Rev. Lett.* **87** (2001) 182301.

[50] C. Adler *et al.*, STAR Collaboration *Phys. Rev. Lett.* **89** (2002) 132301.

[51] J. Adams *et al.*, STAR Collaboration *Phys. Rev. Lett.* **95** (2005) 122301.

[52] D. Kharzeev and M. Nardi, *Phys. Lett.* **B507** (2001) 121.

[53] C. Bernard *et al.*, *Phys. Rev.* **D 55** (1997) 6861; Y. Iwasaki *et al.*, *Phys. Rev.* **D 54** (1996) 7010.

[54] G. Boyd *et al.*, *Phys. Rev. Lett.* **75** (1995) 4169.

[55] H. Heiselberg, *Phys. Rep.***351** (2001) 161 and the refernces therein.

[56] S. Jeon and V. Koch, *Phys. Rev. Lett.* **83** (1999) 5435.

[57] S. Jeon and V. Koch, *Phys. Rev. Lett.* **85** (2000) 2076.

[58] S. Gavin and C. Pruneau, nucl-th/9906060 and nucl-th/9907040.

[59] J. Adams *et al.*, STAR Collaboration, *Phys. Rev.* **C 68** (2003) 044905.

[60] J. Adams *et al.*, STAR Collaboration, *Phys. Rev.* **C 71** (2005) 064906, H. Appelhauser *et al.*, NA49 Collaboration *Phys. Lett.* **B459** (1999) 679.

[61] T. Akesson *et al.*, Helios Collaboration *Z. Phys.* **C38** (1988) 383, H. Heiselberg *et al.*, *Phys. Rev. Lett.* **67** (1991) 2946, B. Blattel *et al.*, *Nucl. Phys.* **A544** (1992) 479c.

[62] M.I. Gorenstein *et al.*, *Phys. Lett.* **B585** (2004) 237.

[63] B. Mohanty and J. Serreau, *Phys. Rep.***414** (2005) 263.

[64] J.D. Bjorken, *Phys. Rev.* **D 27** (1983) 140.

[65] A. Krasnitz, Y. Nara, R. Venugopalan, *Nucl. Phys.* **A717** (2003) 268.

[66] M. Gyulassy and X.N. Wang, *Comput. Phys. Commun.***83** (1994) 307.

[67] B. Andersson *et al.*, *Phys. Rep.***97** (1983) 31.

Chapter 2

The STAR Detector

2.1 Introduction to RHIC

The RHIC (Relativistic Heavy Ion Collider) [1] at Brookhaven National Laboratory (BNL), USA, is a 2.4 miles accelerator ring with multipurpose colliding beam facility which provides beams of both relativistic heavy ions and polarized protons. RHIC was designed with the following unique goals.

1. To simultaneously accelerate different species in each beam.
2. To access a wide range of collision energies from a minimum of $\sqrt{s_{NN}} = 20$ GeV, for Au+Au collisions, to a maximum of $\sqrt{s_{NN}} = 500$ GeV for p+p collisions.
3. To provide a high luminosity (L) beam, making the measurement of rare processes (small cross-sections) feasible.

The particle accelerator that satisfies the above first two conditions is a synchrotron with two independent beam-pipes. However the last of the criteria puts a strict requirement on the luminosity of the collider. For a process with a cross section σ_i, the event rate R_i is given by $R_i = \sigma_i.L$. The luminosity L is given by

$$L = fn\frac{N_1 N_2}{A} \tag{2.1}$$

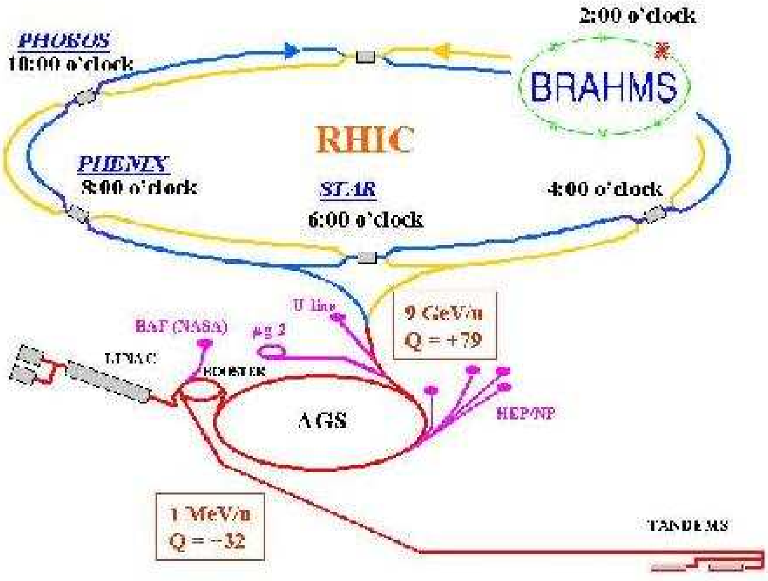

Figure 2.1: The Relativistic Heavy Ion Collider (RHIC) Accelerator Complex.

where N_1 and N_2 are the number of particles contained in the colliding bunches, A is the cross-sectional area of the overlap between the two colliding beams of particles, f is the revolution frequency, n being the number of bunches per beam. Therefore, high luminosity could be achieved by maximizing f, n & N and minimizing the beam profile A.

The collider consists of two quasi-circular concentric accelerator/storage rings on a common horizontal plane. The Blue Ring is for clock-wise and the Yellow Ring is for counter-clock-wise beams. For each ring there is an independent set of bending and focusing magnets as well as radio frequency acceleration cavities. The two rings are oriented to intersect one another at six locations along their 3.8 km circumference. Each ring consist of six arc sections (each $\sim$ 356 m long) six insertion sections (each $\sim$ 277 m long) with a collision point at their center. The rings are focused for collision at the interaction regions using a common set of dipole magnets, the DX and D0 located at 10 m and 23 m respectively. The basic design parameters of the collider is given in Table 2.1. The collision systems used include the heavy-ions Au+Au, Cu+Cu,

Performance Specifications	For Au-Au	For p-p
Beam energy	100→ 30 GeV/u	250→ 30 GeV
Luminosity	$2 \times 10^{26} cm^{-2} s^{-1}$	$1.4 \times 10^{31} cm^{-2} s^{-1}$
Number of bunches/ring	60(→ 120)	60(→ 120)
Number of Particles/Bunch	1×10^{9}	1×10^{11}
Luminosity life time	$\sim$ 10h	$>$ 10h
Bunch width	30 ns	
Ions per beam	1×10^{9}	

Table 2.1: Performance specifications of RHIC.

d+Au and p+p. For Au+Au systems of center of mass energy 200 GeV, Au ions with charge Q = -1 are created using a pulsed sputter ion source. They are then accelerated through the Tandem Van de Graaff facility and a series of stripping foils ultimately yielding Au ions of kinetic energy 1 MeV/nucleon and a net charge of Q = +32. There are two Tandem Van de Graaff accelerators that can run exclusively (using one as a back up) or in parallel (to accelerate two different species simultaneously). The ions are then directed to the booster synchrotron through a 550 meter transfer line. The booster accelerates the Au ions to an energy of 95 MeV/nucleon. The Au ions leaving the booster are further stripped to Q = +77 and are transferred into the AGS, where they are accelerated to 8.86 GeV/nucleon and sorted into four final bunches. Finally, the ions are transferred from AGS to RHIC and stripped to the bare charge state of Q = +79 during the transfer. For p+p beam, protons are injected from the 200 GeV Linac directly into the booster synchrotron followed by acceleration in the AGS and injection into RHIC.

2.2 The RHIC Detector Systems

RHIC consists of four experiments namely, STAR [2], PHENIX [3], PHOBOS [4] and BRAHMS [5] at four different interaction points to study matter at high temperature and energy density for the possible formation of the deconfined state of quarks and gluons, the Quark-Gluon-Plasma (QGP).

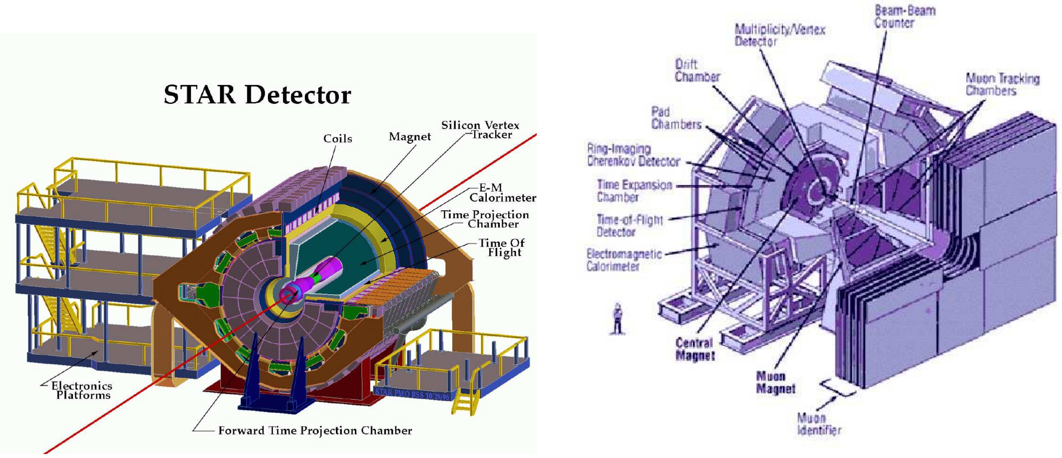

STAR PHENIX

Figure 2.2: Schematic pictures of STAR and PHENIX experiments at RHIC, showing different sub-detectors.

The STAR (Solenoidal Tracker At RHIC) utilizes a solenoidal geometry with a large Time-Projection Chamber (TPC) installed inside a solenoidal magnet, providing a close to 4π solid angle tracking capability for charge particles from the collisions. With projections on the end sectors giving the x-y co-ordinates and drift time of ionization electrons giving the z-coordinates of track segments, the TPC has three dimensional tracking capability. The dE/dx measurement of track segments allow an identification of particles over a significant momentum range of interest. In addition, with the barrel and endcap calorimeters, STAR has the capability of detecting photons, electrons and measuring their energy. It has a Silicon Vertex Tracker (SVT) which surrounds the beam pipe resulting in an improvement in the momentum resolution of the system. It also facilitates the detection of decay vertices of short-lived particles. The PHENIX (Pioneering High Energy Nuclear Interaction eXperiment) (Fig. 2.2) consists of three magnetic spectrometers. It has a central spectrometer consisting of an axial field magnet and two detector arms, one on west and another on east side. It has also two muon arms, one on the north and the other on the south side of the Central Spectrometer along the direction of beams. The basic concept of the Central Spectrometer is to cover selected solid angles with quasi-concentric layers of high-speed detectors of various types. Detector subsystems in the Central Spectrometer arm include Drift Chamber, Pad Chamber, Time Expansion Chamber for tracking and Ring Imaging Cherenkov Detector, Time-of-Flight Detector and Electromagnetic Calorimeter for particle identification. The east and west central arms are centered at zero rapidity and instrumented to detect electrons, photons, and charged hadrons. The north and south forward arms have full azimuthal coverage and are instrumented to detect muons. The global detectors (Zero Degree Calorimeter (ZDC), Beam-Beam Counter (BBC) and the Multiplicity Vertex Detector (MVD)) measure the start time, vertex and multiplicity of particles produced in the interactions. A pair of ZDCs detect neutrons from grazing collisions providing a trigger for the most peripheral collisions. A pair of BBCs provide a measure of the ToF of forward particles to determine the time of a collision. They also provide a trigger for the more central collisions in addition to providing a measure of the collision position along the beam axis. The MVD helps in a more precise determination of event position, multiplicity and measures fluctuations of the charge particle distributions. It is composed of concentric barrels of silicon-strip detectors and end-caps made up of silicon pads. The PHENIX experiment has a high rate capability and fine granularity along with excellent energy, momentum and mass resolution. The major goal of this experiment has been to measure the spin structure of nucleons and to probe each phase of QGP evolution through the study of rare processes involving photons, electrons and muons as well as the predominant hadron production. It has the unique capability of measuring direct photons over a wide range of p_T.

The BRAHMS (Broad RAnge Hadron magnetic Spectrometer) (Fig. 2.3) is a two-arm magnetic spectrometer. One of the arms with a small solid angle is in the forward direction is for the detection of high momentum particles. The other arm is on the side of the collision point for measurements in the mid-rapidity region. Both arms are movable to vary the settings to cover wide range of kinematical regions. The spectrometer consists of room temperature narrow gap dipole magnets, drift chamber planes, other tracking devices, Cherenkov counters and the Time-of-Flight (ToF) detectors which enables momentum determination and particle identification

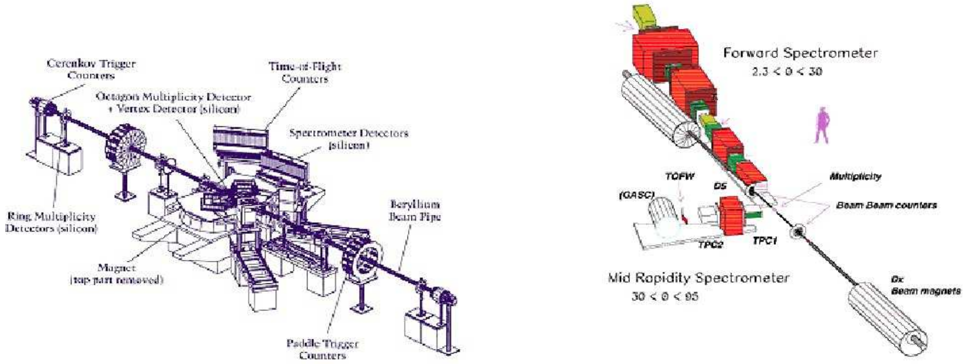

PHOBOS BRAHMS

Figure 2.3: Schematic pictures of PHOBOS and BRAHMS at RHIC, showing different sub-detectors.

over a wide range of rapidity and transverse momentum. BRAHMS does hadron spectroscopy with a wide range of p_T and rapidity to provide essential information on reaction dynamics of collision process. In addition, it measures the rapidity density distributions for protons and anti-protons which is a sensitive measurement for the study of the dynamics of heavy ion collisions. The PHOBOS (named after the famous mission to Mars) (Fig. 2.3) experiment consists of a Multiplicity array, a Vertex detector, a two-arm magnetic spectrometer including a time-of-flight wall, silicon detectors, a set of silicon paddle and cherenkov detector arrays for event triggering and centrality selection. With its multiplicity array it is capable of detecting charged particles over the full solid angle. In addition, it can detect identified charged particles near mid-rapidity in its two spectrometer arms with opposite magnetic fields. The unique feature of PHOBOS is to measure very low p_T charged particles using the silicon detectors.

For the universal characterization of heavy ion collisions, all the four experiments have a common detector subsystem, namely a pair of ZDCs located behind the beam splitting point, out side the dipole magnets. Each of the ZDCs is a small calorimeter which detects neutron multiplicity providing a measure of the collision centrality. The ZDC pair at each crossing point is also used as a luminosity monitor.

2.3 The STAR Detector

STAR [2] was constructed to investigate the behavior of strongly interacting matter at high energy density and to search for signatures of quark-gluon plasma (QGP) formation. STAR measures many observables simultaneously to study both the soft (non-perturbative) and the hard (perturbative) aspects of the possible QGP phase transition and to understand the space-time evolution of the collision process in ultra-relativistic heavy ion collisions. The primary goal is to obtain a fundamental understanding of the microscopic structure of these hadronic interactions at high energy density. A large acceptance design was thus chosen to maximize the information recorded per collision. Additionally, STAR is instrumented with with a high level trigger system that allows real-time selection of rare processes such as high p_T jet, direct photon and heavy quarkonia production. To meet these goals STAR was designed primarily for hadron measurements over a large solid angle featuring layered detector subsystems for high precision tracking, particle identification, momentum analysis and calorimetry about mid-rapidity. STAR's large acceptance makes it unique for detection of hadron jets at RHIC.

The layout of the STAR experiment is shown in Fig. 2.2. A cutaway side view of the STAR detector as configured for the RHIC 2001 run is shown in Fig. 2.4. It is a large acceptance cylindrical detector with full azimuthal acceptance with a room temperature solenoidal magnet [6] with a uniform magnetic field of 0.5 T. This provides the charge particle momentum analysis. Time Projection Chamber (TPC) [7] provides the main tracking of charged particles in STAR with full azimuthal acceptance for $|\eta| \leq 1.8$. Close to the beam pipe TPC is augmented by a silicon inner tracking system (SVT [9] and SSD [10]). This combined system can yield four radial layers of high precision space points, improving the position resolution of the detector and allowing for the secondary vertex reconstruction of short lived particles. The silicon detectors cover a pseudo-rapidity range $|\eta| \leq 1$ with complete azimuthal symmetry. Both SVT and TPC contribute to particle identification using ionization energy loss. To extend the tracking to the forward region, there exists a radial-drift TPC (FTPC) [11] which covers $2.5 < |\eta| < 4$ with complete azimuthal coverage. A

Ring Imaging Cherenkov detector (RICH) [12] ($|\eta| < 0.3$, $\delta\phi = 0.11\pi$) and a time-of-flight (TOF) [13] patch ($-1 < \eta < 0$, $\delta\phi = 0.04\pi$), present in the STAR detector, can extend particle identification to larger momenta, over a limited solid angle at mid-rapidity. Outside the TPC is a highly segmented Barrel Electromagnetic Calorimeter (BEMC) [14] with full ϕ-coverage for $0 \leq |\eta| \leq 1$. It provides measurement of total energy of electromagnetic particles primarily electrons and photons. Along with BEMC, the Endcap Electromagnetic Calorimeter (EEMC) [15] with full ϕ-coverage for $-1 < \eta < 2$. It allows measurement of transverse energy, E_T, of events in addition to providing a trigger for high p_T photons, electrons and electromagnetically decaying hadrons. The EMCs (BEMC and EEMC) include a set of Shower Max Detectors (SMD) to distinguish high momentum single photons from photon pairs resulting from π and η meson decays. The EMCs also provide prompt charged particle signals essential to discriminate against pile up tracks in the TPC, arising from other beam crossings, falling within the 40 μs drift time of the TPC, which are anticipated to be prevalent at RHIC pp collision luminosities ($\approx 10^{32} cm^{-2} s^{-1}$). In the forward region, at a distance of 5.5 m from the interaction point, STAR has a highly granular pre-shower Photon Multiplicity Detector (PMD) [16] for counting photons and their spatial distributions on an event-by-event basis. It covers a pseudo-rapidity region of $-3.8 \leq \eta \leq -2.4$ with full azimuthal coverage. Along with FTPC, PMD can address different physics issues related to charge-to-neutral fluctuations (DCC-like signatures), azimuthal anisotropy (Flow), multiplicity fluctuations (in photons) etc. A Forward Pion Detector (FPD) [21] sits in the forward region at about 7.5 meter from the interaction point. Additionally, there are several detector systems which are used for event selection purposes. These include, Central Trigger Barrel (CTB) [22] ($|\eta| < 1$, $\delta\phi = 2\pi$) two Zero-Degree Calorimeters (ZDCs) [23] located at $\theta < 2$ mrad to the beam axis, at 18 meters on both sides of the interaction point, a Beam Beam Counter (BBC) at high η region and a Multi Wire Proportional Counter (MWPC). The CTB measures charge particle multiplicity for trigger purposes while the BBC is used for normalizing event rates in the pp program. The ZDCs measure the neutron multiplicity in a small solid angle near zero degree for generating an interaction signal for RHIC operation as well as providing a hadronic minimum bias trigger.

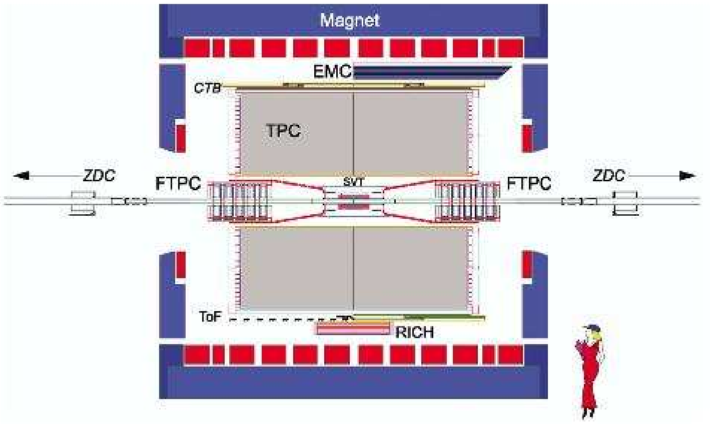

Figure 2.4: Cutaway side view of the STAR detector as configured in 2001.

2.3.1 Time Projection Chamber (TPC)

TPC is the main tracking device in STAR. The TPC records the tracks of particles, measures their momenta and identifies the particles by measuring their ionization energy loss (dE/dx). It haz full azimuthal coverage with $|\eta| \leq 1.8$. Particles are identified over a momentum range from 100 MeV/c to greater than 1 GeV/c and momenta are measured over a range of 100 MeV/c to 30 GeV/c. The STAR TPC is shown schematically in Fig. 2.5. It's surrounded by a large solenoidal magnet which operates at 0.5 T. The TPC is 4.2 m in length and 4 m in diameter. The cylinder is concentric with the beam axis. The inner and outer radii of the active volume are 0.5 m and 2.0 m respectively. TPC covers a pseudo-rapidity interval that ranges from $-1.8 < \eta < 1.8$ for the inner radius and $-1 < \eta < 1$ for the outer radius (see Fig. 2.6). It's an empty volume of gas ($P10 : Ar + 10\%\ CH_4$) at ~ 2 mbar above atmospheric pressure, in a well-defined, uniform electric filed of ≈ 135 V/cm. The paths of primary ionizing particles passing through the gas volume are reconstructed with high precision from the released secondary electrons which drift in the uniform electric field to the readout end caps at the ends of the chamber. Two co-ordinates are determined by the location where the electron is detected. The third co-ordinate is reconstructed using the time taken for the electron to reach the wire chamber (time

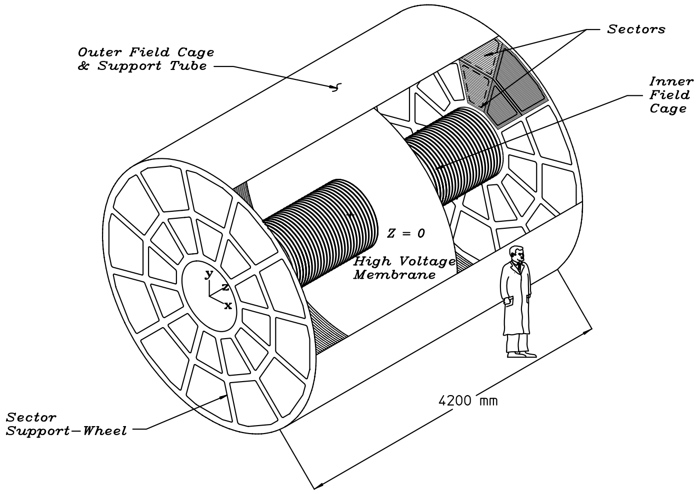

Figure 2.5: The STAR TPC surrounds a beam-beam interaction region at RHIC.

bin) and the electron drift velocity in the gas. The secondary electrons drift inside the electric field to two detection planes, one on each end of the chamber ($z \simeq \pm 210cm$). A large diaphragm made up of carbon coated Kapton (central membrane), having a thickness of 70 μm, is stretched between the inner and outer field cages at the center of the TPC ($z = 0cm$). The central membrane is maintained at a high voltage with respect to the detection planes. The liberated electrons thus drift away from the central membrane to the closest end cap of TPC, where their position in the (r, ϕ) plane is determined as a function of time. The mean drift time constitutes a measurement of the electron's ionization point along the z-axis, yielding the third dimension.

The requirement of the presence of uniform electric field ($\vec{E}$) inside TPC is achieved by a set of field cages. The field cage design consists of two concentric cylinders which define the active volume of the TPC. A highly uniform electric filed is created along the axis by a series of equipotential rings placed on the surfaces of the inner and outer field cages. The field magnitude is the greatest at the central membrane having a bias voltage of -31 kV and decreases in a steady manner to zero voltage at the ground

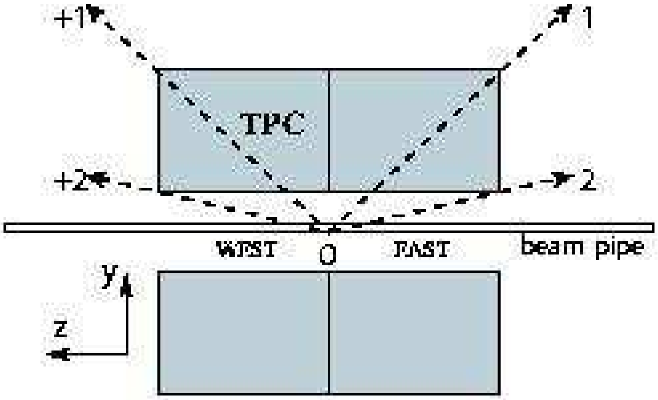

Figure 2.6: Schematic view of the TPC illustrating the co-ordinate system and pseudo-rapidity coverage. The x-axis points out of the page of the paper.

wires located on either end of TPC. Irregularities in the spacing of the rings or in the rings themselves will result in radial field components and consequently lead to a degradation in the momentum resolution. The schematic picture of the field cage design is shown in Fig. 2.7.

The electric field and the gas conditions determine the drift velocity (v_{drift}) of the electrons in TPC. v_{drift} is measured in various ways, but a primary calibration makes use of the mirrored laser system where a single beam is split into many beams of known locations. The beam ionize the P10 gas and the electrons are detected in the MWPC. The known locations of the beams allow for an absolute calibration of v_{drift}. The drift velocity was calculated to be $5.44 \pm 0.01 cm/\mu s$, with typical time dependent variations of the order of $\sim 6\%$.

Particle Identification Method

Charge particles passing through TPC lose energy through ionization. The total charge collected from each hit of a track, due to ionization is proportional to the energy loss of the particle. The mechanism of energy loss is an efficient tool for identifying

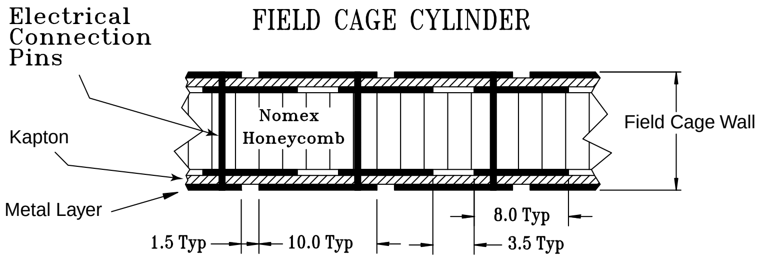

Figure 2.7: An IFC showing the construction and composition of the cylinder wall. Dimensions are in mm.

particle species in TPC. This method works fine for low momentum particles but as the particle energy increases, the energy loss becomes less mass dependent and it's hard to distinguish particles with velocity $v > 0.7c$. The STAR was designed to separate pions and protons up to 1.2 GeV/c. For a charge track crossing the entire TPC we obtain 45 dE/dx values from the energy loss at 45 pad rows. The length over which the energy loss is measured, is too short to average out ionization fluctuations. In fact particles loose energy while going through the gas in frequent collisions with atoms where a few tens of eV are released. Hence it is not possible to measure accurately the average dE/dx. Indeed, the most probable energy loss is measured. We do this by removing the largest ionization clusters. The energy loss is distributed according to the Landau probability distribution. One of the properties of this distribution is that it's tail dies off very slowly and the dispersion of values around the mean is very large (theoretically, it's infinite). A typical procedure to reduce fluctuations from the long Landau tails is to truncate the distribution. In STAR, we have used 70% truncation, i.e. the highest 30% ionization values were discarded. Using the remaining values, a truncated mean is computed and this becomes the basis of any analysis using identified particles in TPC. The measured truncated mean for primary and secondary charged particles is shown as a function of momentum in Fig. 2.8. The continuous curves are the Bethe-Bloch parameterization used in the analysis for different particle hypotheses [8]. We see that at the lowest momentum, the pions have a greater ionization energy loss than the electrons which are already

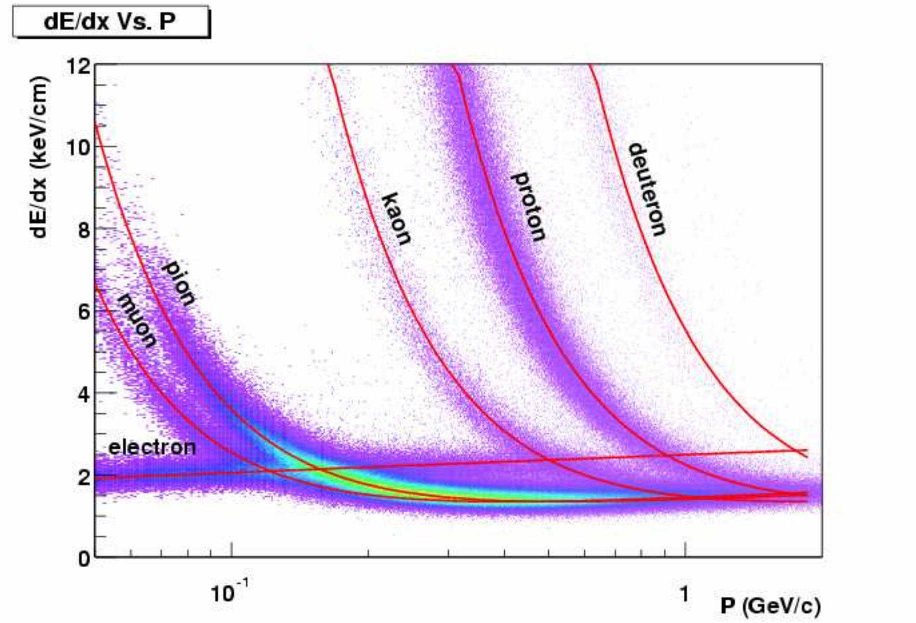

Figure 2.8: The energy loss distribution of particles in the STAR TPC as a function of the momentum of primary particles. The curves are the Bethe-Bloch function for different particle species. The magnetic field was 0.25 T.

in the saturation region of the curve. The pions cross over the electron band around $0.15 GeV/c$ reaching a minimum at about $0.3 GeV/c$. The pions in their relativistic rise merge with the kaons, which are still in the $1/\beta^2$ region, at about $1 GeV/c$.

The Bethe-Bloch formula for energy loss of a particle of charge z (in units of e) and speed $\beta(= v/c)$, passing through a medium of density ρ, is given by

$$-\frac{dE}{dx} = 2\pi N_a {r_e}^2 m_e c^2 \rho \frac{Z}{A}\frac{z^2}{\beta^2}\left[ln\left(\frac{2m_e\gamma^2 v^2 W_{max}}{I^2}\right) - 2\beta^2 - \delta - 2\frac{C}{Z}\right] \qquad (2.2)$$

where

N_a: Avogadro's number
m_e: mass of electron
$r_e(= e^2/m_e)$: classical electron radius
Z: atomic number of the absorbing material
A: atomic weight of the absorbing material
$\gamma = 1/\sqrt{1-\beta^2}$
I: mean excitation potential
W_{max}: maximum energy transfer in a single collision
δ: density correction
C: shell correction

2.3.2 Zero Degree Calorimeter (ZDC)

The very basic step in collider experiments is to decide when to read out the data from the detector. This is called triggering and the scheme may be basic or complex depending on the topology of the collisions to be selected. At the most basic level, it is required to know if a collision has occurred. Such a scheme is called minimum bias trigger. At the most complex level one may want to ignore all the events that do not satisfy the topology of, e.g. a top quark event. At RHIC a common minimum bias trigger scheme was developed for heavy ion running for all the four experiments. The trigger is based on two ZDCs, one on each side of the interaction point. An inelastic

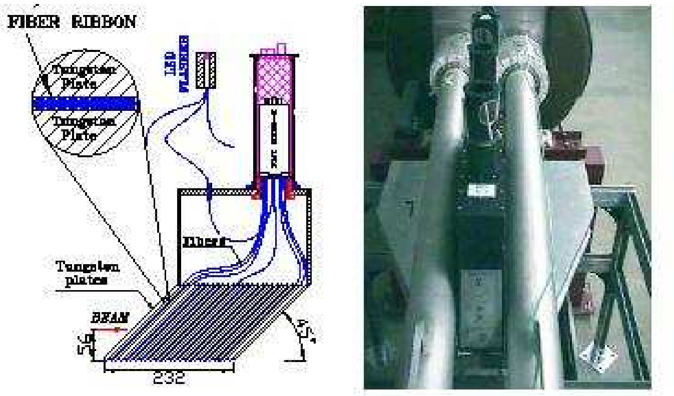

(a) **(b)**

Figure 2.9: (a) Diagram of ZDC layout. (b) Picture of mounted ZDC between the RHIC beam lines.

heavy ion collision is accompanied by the emission of beam remnant neutrons at high energies and small angles (~ 2 mrad) with respect to the beam. ZDC is a hadronic calorimeter that is designed to detect neutrons. The ZDCs are centered at zero degree approximately at ±18 meters downstream of the interaction point and subtend 2.5 mrad. ZDCs are located beyond the DX dipole magnets which bend the beams back into their respective orbits. The DX magnets additionally act to sweep away charged fragments, so only neutral fragments can reach the ZDC. Fig. 2.9 shows the layout and location of ZDCs in the beam line.

The ZDCs employ layers of tungsten absorbers together with Cherenkov fibers for sampling. The light generated in the fibers is sent to a set of three PMTs (Photo Multiplier Tube) with the summed analog output of the PMTs used to generate the ZDC signals. The hadronic Au+Au minimum bias trigger used by STAR requires a coincidence between the two ZDCs, with each ZDC signal having a summed analog PMT output corresponding to ~ 40% of a single neutron signal. The readout electronics used in each of the experiments are identical in design. The signal from each ZDC is split in two, with one signal being sent to the RHIC for luminosity monitoring and the other used as input for the experiment trigger.

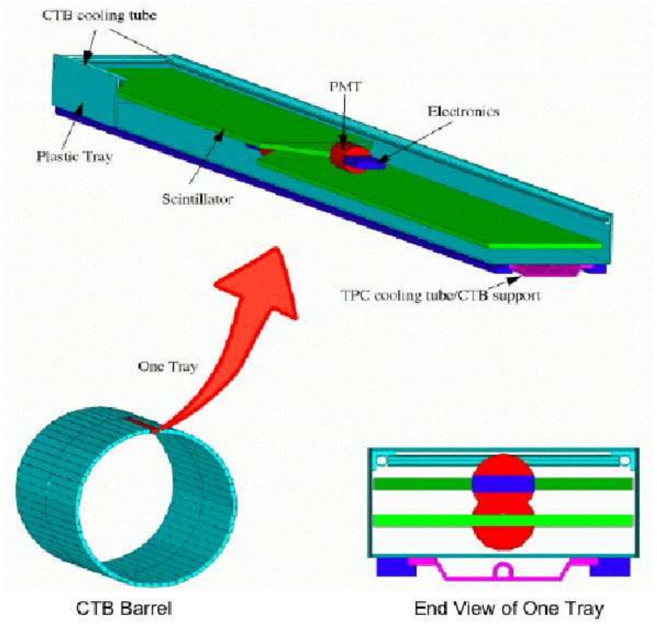

Figure 2.10: CTB cylinder and the details of tray and slat.

2.3.3 Central Trigger Barrel (CTB)

An additional design requirement of STAR was the ability to select events in real time based on charged particle multiplicity at mid-rapidity. This is achieved via a collection of scintillating tiles arranged in a cylindrical fashion around the radial exterior of the TPC (see Fig. 2.4). This collection of tiles is called CTB, the Central Trigger Barrel. Charge particles traversing through a CTB tile, generate scintillation light which is collected via a PMT. The corresponding output is proportional to the number of charged particles that traversed through the slat. CTB is a fast detector and along with ZDC, it allows for a powerful charged particle multiplicity trigger. The CTB consists of 240 slats of plastic scintillator, 4m in length, with $|\eta| \leq 1$ and full ϕ-coverage. The slats are housed in aluminum trays with two slats per tray. Each slat has one radiator, one light guide and one PMT. Fig. 2.10 shows a segment with two slats. The slat closest to the center contain tiles of $112.5 \times 21 \times 1\ cm^3$ and the slat away from the center is $130 \times 21 \times 1\ cm^3$. A single slat covers $\Delta\phi = \pi/30$ radians

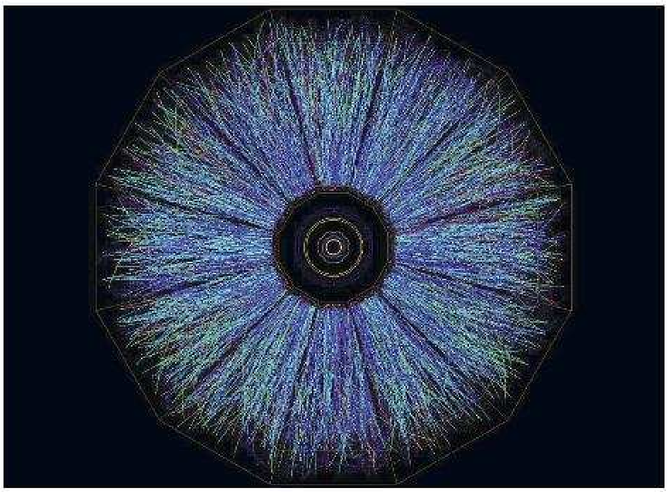

Figure 2.11: Beam's eye view of a central event in the STAR TPC. This event was drawn by the STAR level-3 on line display.

and $\Delta\eta = 0.5$. The PMT signals generated by the slat are sent to digitizer boards, each having 16 inputs. Within each digitizer, the signals are sent to an integrator, an 8-bit ADC and then to a discriminator. The output of the discriminator can be summed over the barrel and used in the trigger logic. The CTB calibration yields an average of 5 ADC counts for a minimum ionizing particle.

2.3.4 Beam Beam Counter (BBC)

The ZDC and CTB are specifically designed for triggering in Au+Au collisions. The topology of p+p collisions is vastly different from Au+Au collisions in terms of multiplicity or the number of tracks per event. In Au+Au collisions, the event multiplicity is very high and thus a minimum bias trigger can be implemented based on many mid-rapidity tracks and spectator neutrons, which p+p collisions lack. To solve this problem of acceptance gap and for the p+p triggering, Beam Beam Counters (BBCs)

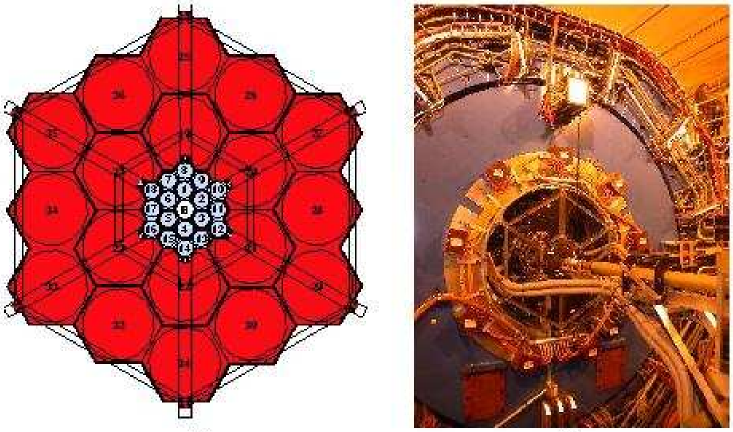

(a) (b)

Figure 2.12: (a) Diagram of BBC layout. (b) Picture of the BBC frame mounted on the STAR end cap with the RHIC beam line.

were introduced. Non-Singly Diffractive (NSD) inelastic interactions are characterized by the breakup of both the incoming protons. The hard scattered partons are realized in the final state as particles near mid-rapidity, while the remnant partons produce two "beam-jets". The beam-jets are groups of high energy hadrons that are focused in the high (near beam) rapidity region. A traditional trigger for NSD interactions is therefore a set of two scintillating disks that are sensitive to the beam jet region.

The BBCs are annular disk shaped scintillator detectors which are sensitive to charge particles. They are situated at ±3.5m from the interaction point as two end caps of the TPC. Fig. 2.12 shows a schematic diagram of BBCs and a picture of BBC frame mounted in STAR. Each BBC disk is composed of scintillating tiles arranged in a hexagonal closed pack structure. The RHIC beam line passes through the center of the BBCs with a 1 cm annular clearance.

Eight PMTs are used for the 18 inner tiles. Each tile has four wavelength shifting (WLS) optical fibers inserted into circular grooves inscribed within the hexagonal scintillator to collect scintillation light. The scintillation light is then sent to the PMTs and digitized via an ADC. The tiles are grouped to allow for radial and azimuthal

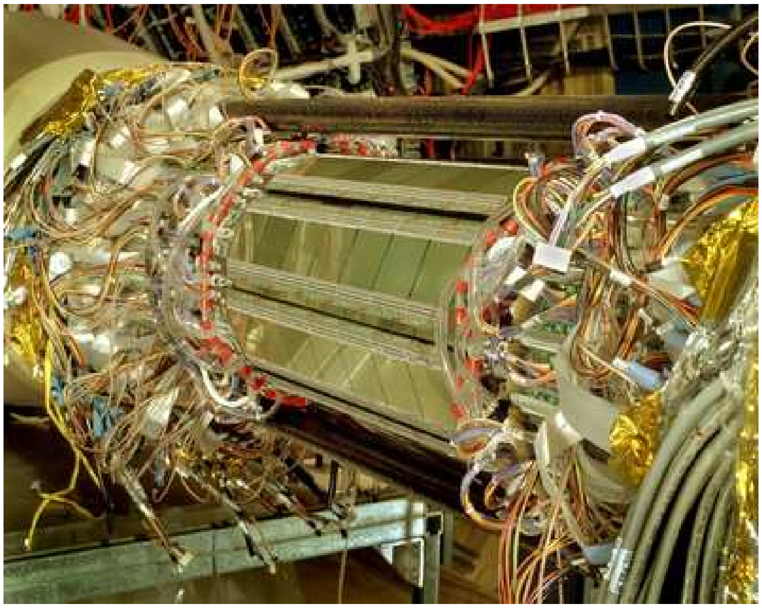

Figure 2.13: Picture of SVT instrumented in RHIC beam line.

segmentation of the readout. The grouping is 1, 2-3, 4, 5-6, 7-9, 10-12, 13-15, 16-18. The fine segmentation of the BBCs was not used in the p+p minimum bias trigger. Rather the trigger sums, the output of all the tiles on a BBC and a coincidence of both BBCs firing above noise threshold was required within a time window of $\Delta t \equiv |t_{east}^{BBC} - t_{west}^{BBC}| < 17$ ns, which is determined by the time resolution of the detector.

2.3.5 Silicon Vertex Tracker (SVT)

The Silicon Vertex Tracker (SVT) is a solid state drift detector located just outside the beam pipe [9]. It is designed to improve the primary vertexing, track identification to a higher precision and better energy-loss measurement for particle identification. It aims to enhance the physics capabilities of the TPC. It also helps in the reconstruction of very short-lived particles through secondary vertexing close to the interaction zone. In addition, it expands the kinematical acceptance for primary particles to very low momentum by using independent tracking in the SVT alone for charged particles that do not reach the active volume of TPC due to the applied magnetic field. The total active length of SVT is 44.1 cm. It has full azimuthal coverage with $|\eta| < 1$. The detector is made up of 216 independent wafers with a dimension of 6.3 cm × 6.3 cm, containing over 13 million pixels multiplexed onto 1300 readout channels. They are arranged in three cylindrical layers at distances of about 7, 11 and 15 cm from the beam axis. A "pixel" in a drift detector is defined by the anode segmentation in one co-ordinate and the drift velocity divided by the sampling frequency in the drift direction co-ordinate. The pixel-like readout of the silicon drift detector makes it a good choice for the high multiplicity environment in heavy ion reactions at RHIC. Since it has three layers, a minimum of three space points are required for the determination of the tracking parameters. It has a lower momentum cut off $\sim$ 50 MeV/c, compared to the TPC for which the corresponding value is $\sim$ 150 MeV/c. The SVT thus enhances the capability of studying low-p_T physics.

Position resolution of 20μm in both co-ordinates as well as energy loss (dE/dx) measurements with a resolution of about 7% were achieved with STAR-SVT. In high multiplicity environments SVT could be used for improving the vertex finding resolution. The overall tracking efficiency for SVT is approximately 80%. It is useful for the study of heavy-flavor physics as well.

2.3.6 Silicon Strip Detector (SSD)

The STAR Silicon Strip Detector (SSD) [10] constitutes the fourth layer of the inner tracking system. Installed between the SVT and the TPC, the SSD enhances the tracking capability of the STAR detector by measuring accurately two-dimensional hit position and energy loss for charged particles. It aims specifically at improving the extrapolation of TPC tracks through SVT hits and increasing the average number of space points measured near the collision, thus increasing the detection efficiency of long-lived meta-stable particles.

The SSD is placed at a distance of 230 mm from the beam axis, covering a pseudo-rapidity range of $|\eta| < 1.2$ which leads to a total silicon surface close to $1m^2$. The design of the SSD is based on two clamshells, each containing 10 carbon-fiber ladders.

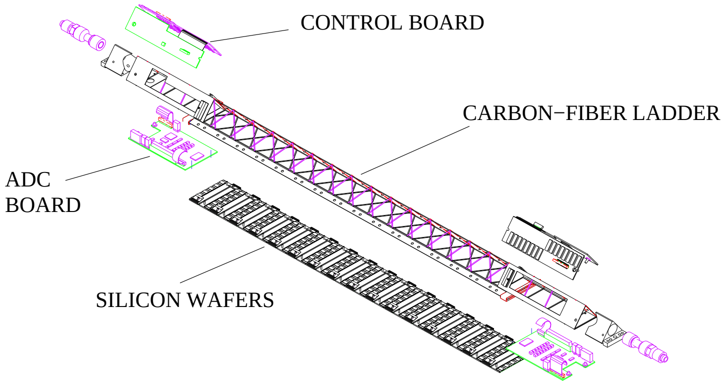

Figure 2.14: An SSD ladder showing separately it's components

Each ladder (shown in Fig. 2.14) supports 16 wafers using double-sided silicon strip technology (768 strips per slide) and connected to the front-end-electronics by means of the Tape Automated Bonded (TAB) technology. The ladders are tilted with respect to their long axis, allowing the overlap of the detectors in the transverse plane for better hermiticity and alignment performances. A bus cable transports the analog signals along the ladder to two 10 bits ADC boards installed at both the ends. After digitization, the signals are sent to readout boards which are linked to the DAQ system through Giga-link optical fibers.

2.3.7 Forward Time Projection Chamber (FTPC)

The two Forward Time Projection Chambers (FTPCs) are radial drift chambers constructed to extend the phase space coverage of the STAR experiment to $2.5 < |\eta| < 4.0$. The FTPCs are located along the beam line at 210 cm from the center of the TPC. They measure momenta and production rates of charged particles as well as neutral strange particles. The FTPC [11] concept was determined firstly by the high particle density with tracks under small angles with respect to the beam direction and secondly by the restricted available space inside the TPC. The layout of FTPC

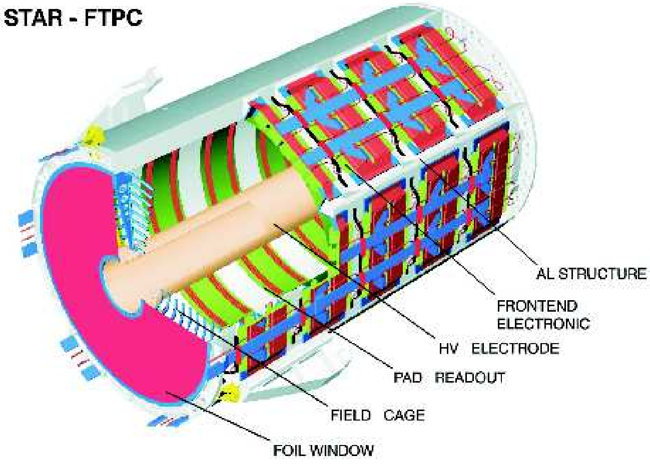

Figure 2.15: Layout of Forward Time Projection Chamber

is shown in Fig. 2.15. It is a cylindrical structure, 120 cm long and 75 cm in diameter, with a radial drift field and readout chambers located in five rings on the outer cylinder surface. Each ring has two pad rows and is subdivided azimuthally into six readout chambers. The radial drift configuration was chosen to improve the two-track separation in the region close to the beam pipe where the particle density is the highest. The field cage is formed by the inner HV-electrode, a thin metalized plastic tube and the outer cylinder wall at ground potential. The field region at both ends is closed by a planner structure of concentric rings, made up of thin aluminum pipes. The front end electronics (FEE), which amplifies, shapes and digitizes the signals, is mounted on the back of the readout chambers. Each particle trajectory is sampled up to 10 times. During the passage of energetic particle, the ionization electrons drift to the anode sense wires inducing signals on the adjacent cathode surface which are read out by 9600 pads (each $1.6 \times 20\ mm^2$). The above design has some new features.

1. The electrons drift in a radial electric field perpendicular to the solenoidal magnetic field.

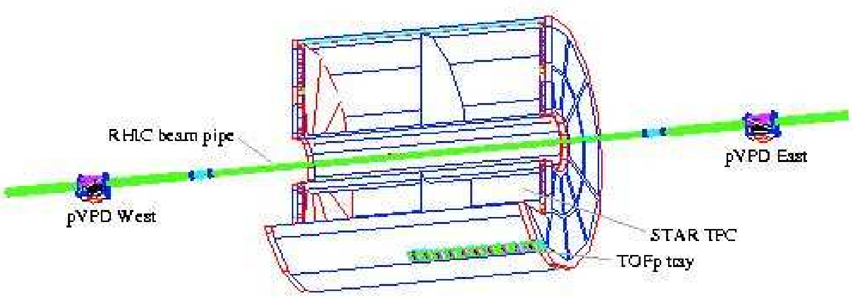

Figure 2.16: A scale drawing of the locations of pVPD and TOFp detectors in relation to the STAR TPC and the RHIC beam pipe. Here TPC view is cut away and the STAR magnet as well as other systems are not drawn.

2. Curved readout chambers are used to keep the radial field as ideal as possible.

3. A two-track separation of 1-2 mm is expected, which is an order of magnitude better than all previously build TPCs with pad readout.

The FTPCs use a mixture of Ar and CO_2 with 50:50 ratio. The FTPC track reconstruction is effected by calculating the track points from the charge distributions measured by the readout electronics. The grouped track points (up to 10 position measurements per track) and the magnetic field map are then used to estimate the momentum. The FTPCs helps in complete event characterization at forward rapidity.

Each FTPC has a position resolution of 100 μm and a two track separation of 1 mm. The momentum resolution is between 12 to 15% with an overall reconstruction efficiency lying between 70 to 80%.

2.3.8 Time Of Flight (TOF)

Time of Flight (TOF) detector aims for the identification of hadrons produced in heavy ion collisions. The STAR TOF consists of two separate detectors namely, Pseudo Vertex Position Detector (pVPD) (the 'start' detector) and the Time of Flight Patch (TOFp) (the 'stop' detector). The TOFp has a phase space coverage of $-1 < \eta < 0$ with $\Delta\phi = 0.11\pi$. It extends particle identification up to $p_T \sim 3GeV/c$ for both p and $\overline{p}$. The pVPD consists of two identical detector assemblies that are positioned

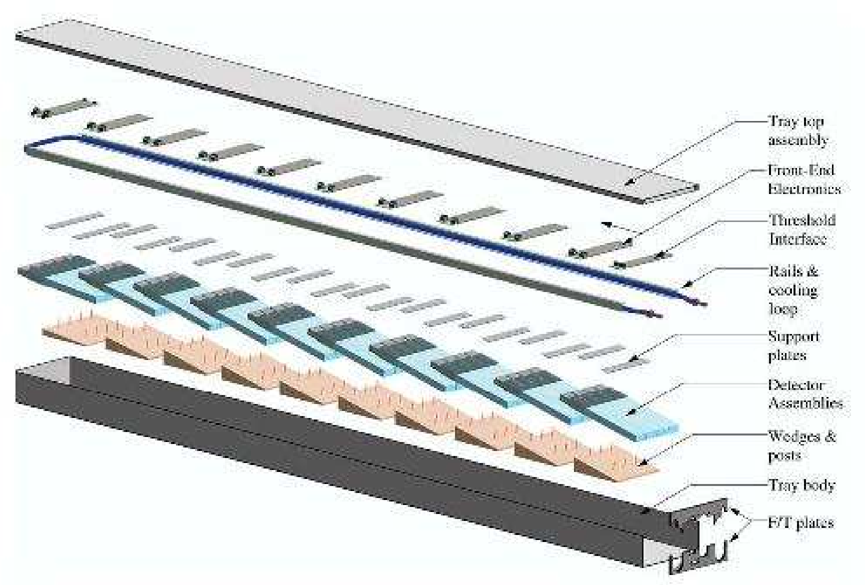

Figure 2.17: An exploded view of TOFp tray

very close to the beam pipe, out side the STAR magnet on both the sides. The TOFp sits inside the STAR magnet just outside the TPC. The location of the collision vertex along the beam pipe is determined by measuring the arrival time of the forward particle pulses at pVPD and TOFp. The average of these two arrival times is the event start time. This, with the TOFp stop time, provides time interval measurements. The design of the pVPD is based on plastic scintillator readout using photomultiplier tubes with CAMAC-based digitization. There are three pVPD detector elements on each side of STAR at a distance of about 5 m from the interaction region. The start resolution attained by the pVPD is around 24 ps, implying a pVPD single detector resolution of 58 ps. The total time resolution of the system averaged over all detector channels is about 87 ps. This allows a $\pi/K/p$ discrimination for momenta up to $\sim$ 1.8 GeV/c and direct $(\pi + K)/p$ discrimination up to $\sim$ 3 GeV/c. The STAR TOF tray (TOFr) is based on multi-gap resistive plate chamber (MRPC) technology. It consists of a highly segmented cylindrical detector immediately surrounding the TPC. It covers a pseudo-rapidity range of $-1 < \eta < 0$ and $\Delta\phi = \pi/30$. For the full coverage in STAR, there are 120 trays, 60 each on east and west sides. Each individual tray is 2.4 m long, 21.3 cm wide and 8.5 cm deep. Each tray corresponds to 33 MRPCs having 6 readout channels [13].

2.3.9 Forward Pion Detector (FPD)

The STAR Forward Pion Detector (FPD) is placed on the east side at about 7.5 m along z-direction from the interaction region, at a radial distance of about 50 cm from the beam line. The FPD consists of a prototype of the Endcap Electromagnetic Calorimeter (pEEMC) together with a Pb-glass detector array. FPD measures single-spin transverse asymmetry for leading π^0s coming from p+p collisions. It confirms if the colliding beams are polarized and can lead to information on the polarization vector at the STAR collision point.

The pEEMC part of the FPD is a lead sampling calorimeter comprised of 21 layers of 5 mm thick Vulcan lead sheets interleaved with 24 layers of 5 mm thick Kuraray SCSN-81 plastic scintillator sheets. The total material is of approximately 21 radiation length. The layers are machined into 12 optically isolated tiles in a 3 × 4 pattern and thus forming 12 towers. The collection and transportation of scintillation light is done using 0.83 mm diameter wavelength shifting fibers inserted into "sigma grooves" machined in the scintillator. The other part of the FPD, called the Shower Maximum Detector (SMD), sits behind the sixth layer of pEEMC with about 5 radiation length of pEEMC material in front of it. It is comprised of two orthogonal planes of finely segmented scintillator strips. There are 60 horizontal and 100 vertical strips. Each strip has a transverse profile resembling an equilateral triangle with an apex-to-base height of 5 mm. Optical isolation was achieved by wrapping individual triangular strips with 50 μm of aluminized mylar. The strips are arranged parallel to each other such that any two adjacent ones have a cross section in the form of a parallelogram [21].

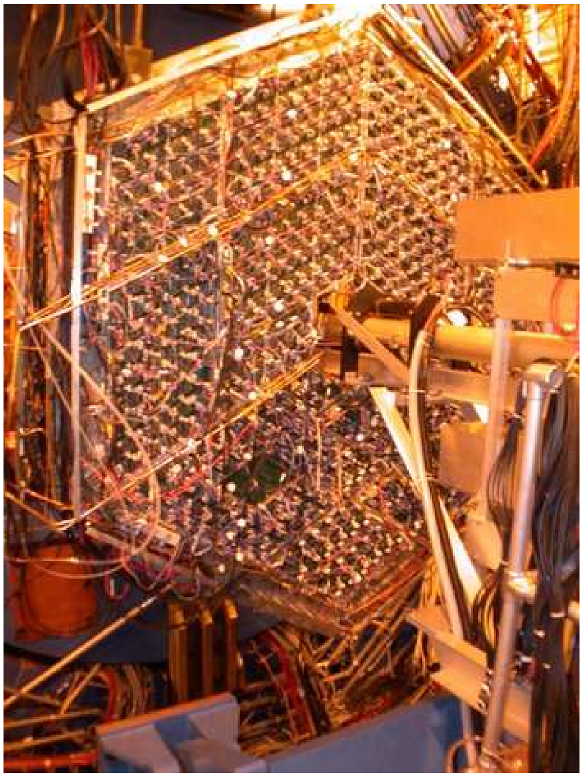

Figure 2.18: Beam view of STAR PMD installed in RHIC beam line (view from tunnel).

2.3.10 Photon Multiplicity Detector (PMD)

The STAR Photon Multiplicity Detector (PMD) is a highly granular pre-shower detector aiming at detecting photons in the forward rapidity region, where high particle density precludes the use of a calorimeter. It is situated at a distance of 5.4 m from the interaction region on the east side of the STAR experiment, covering a pseudo-rapidity interval of $-3.7 \leq \eta \leq -2.4$ with full azimuthal coverage [16]. PMD measures the multiplicity and spatial distribution of photons on an event by event basis. Using similar information of charged particles from other detectors like FTPC, PMD can address various physics issues like: (a) determination of reaction plane and the probes of thermalization via studies of azimuthal anisotropy and flow [17], (b) critical phenomena near the phase boundary leading to fluctuations in global observables like multiplicity and pseudo-rapidity distributions [18, 19] and (c) signals of chiral symmetry restoration [18].

The STAR PMD consists of a pre-shower and a charge particle veto (CPV) plane. Each plane consists of a large array of hexagonal cells (41,472 in each plane) which are tiny gas proportional counters. A mixture of Ar and CO_2 in the ratio of 70:30 is used as the sensitive medium. The cells are physically separated from each other by thin metallic (copper) walls to contain δ-electrons. A honeycomb of 24×24 cells form a unitmodule in the form of a rhombus. A set of unitmodules are enclosed in a gas tight chamber called a supermodule. The number of unitmodules in a supermodule varies from 4 to 9. Each detector plane consists of 12 such supermodules. A 5 mm thick steel support plate and a 15 mm thick lead plate together form a converter of thickness $3X_0$ which is sandwiched between the CPV and the pre-shower planes. For a supermodule, the metallic walls of the honeycomb form a common cathode kept at a large negative potential. The individual anode wires (gold coated tungsten) in the cells are kept at ground potential and are connected to the readout electronics. GASSIPLEX chips [20] have been used in the front end electronics (FEE) with C-RAMS based readout.

In PMD, a photon passing through the lead converter produces an electromagnetic shower. These shower particles produce signals in several cells of the sensitive volume of the detector. Charged hadrons usually affect only one cell and produce a signal

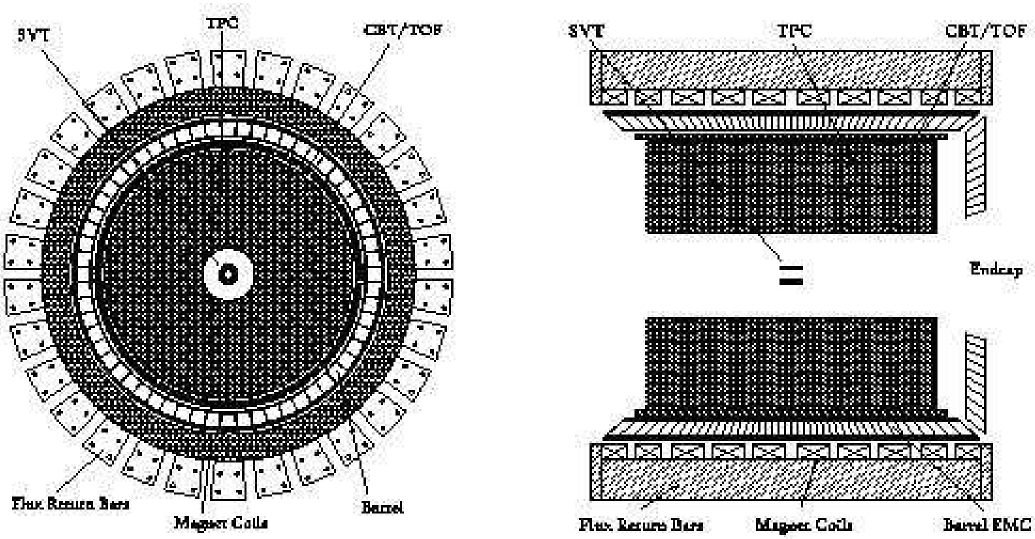

Figure 2.19: Cross-sectional views of STAR detector showing BEMC

resembling that of Minimum Ionizing Particles (MIPs). The thickness of the converter is optimized for high conversion probability of photons, limiting the transverse spread of showers to minimize their overlap in a high multiplicity environment. In order to have better hadron rejection capability, the charge particle veto detector is placed before the lead converter.

2.3.11 Barrel Electromagnetic Calorimeter (BEMC)

The STAR Barrel Electromagnetic Calorimeter (BEMC) triggers on and used to study rare, high p_T processes (jets, leading hadrons, direct photons, heavy quarks) with a large acceptance for photons, electrons, π^0 and η mesons in a variety scenarios (polarized pp through AuAu collisions). The BEMC permits the reconstruction of π^0's and isolated (direct) photons at relatively high $p_T \approx 25 - 30$ GeV/c. It is capable of identifying single electrons and pairs in intense hadron backgrounds from heavy vector mesons and W and Z decays. All these measurements require precise electromagnetic shower reconstruction with high spatial resolution. This is achieved

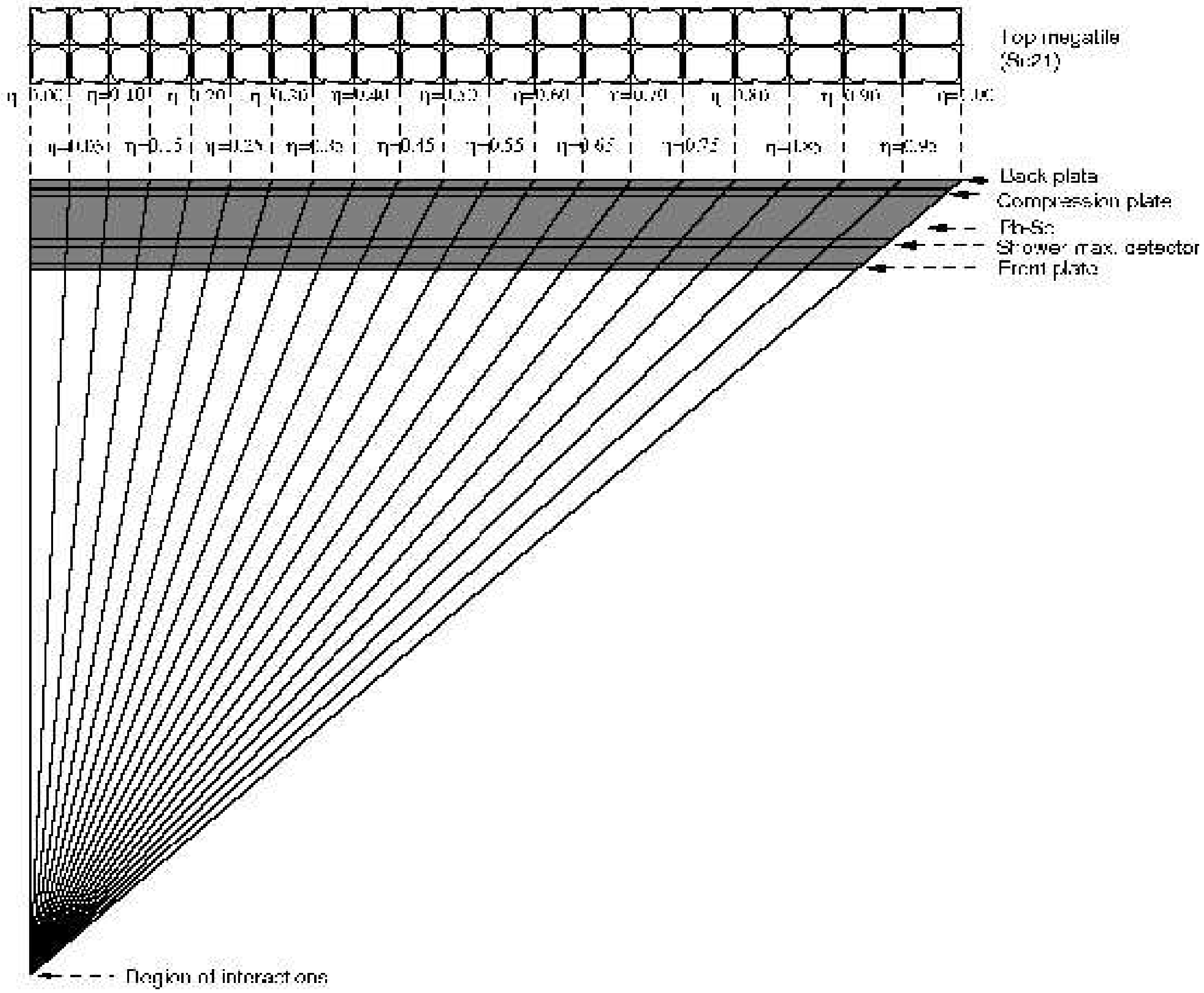

Figure 2.20: Side view of a calorimeter module showing the projective nature of the towers. The 21st mega-tile is also shown in plan view.

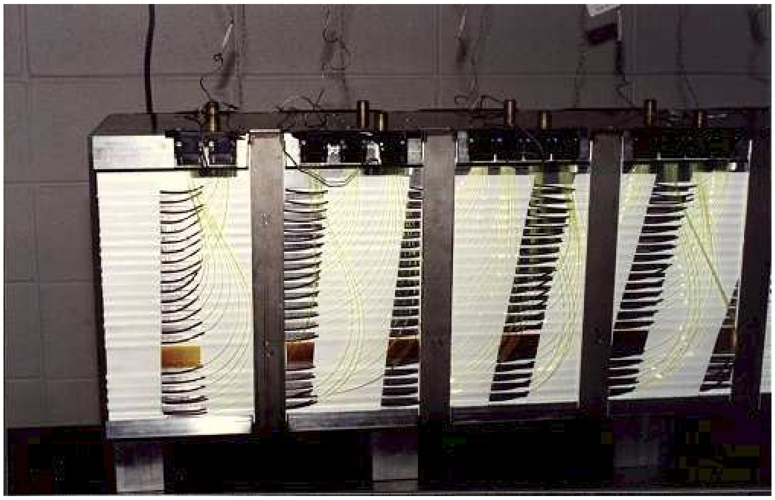

Figure 2.21: Photograph of a BEMC module taken near the $\eta = 0$ end showing the projective towers and the WLS fiber routing pattern along the side of the modules. The WLS fibers terminate in 10 pin optical connectors mounted on the back (top in the photo) plate of the module.

by the implementation of shower maximum detectors (essentially two layers of gas wire pad chambers) within the BEMC lead/scintillator stack. These enable measurement of shower distribution with high spatial resolution in two orthogonal (transverse) directions.

The BEMC [14] is located inside the aluminum coil of STAR solenoid and covers a range of $|\eta| \leq 1.0$ and 2π in azimuth. Thus it matches the acceptance of full TPC for tracking. This is shown schematically in Fig. 2.19. The front face of the calorimeter is at a radius of $\approx$ 220 cm from and parallel to beam axis. The design for BEMC includes a total of 120 calorimeter modules, each subtending 6^0 in ϕ ($\sim$ 0.1 rad) and 1.0 unit in η. These modules are mounted so that there are 60 of them in full ϕ with 2 for the complete η range for every ϕ. The modules are segmented into 40 towers, 2 in ϕ and 20 in η, with $\Delta\phi, \Delta\eta$ for each tower being 0.05 and 0.05 respectively. At the radius of the inner face of the detector, the tower size is $\sim$ 10×10 cm^2 at $\eta = 0$ which increases towards $\eta = 1$. The full BEMC is thus segmented into 4800 towers, arranged in a projective geometry each of them pointing back to the

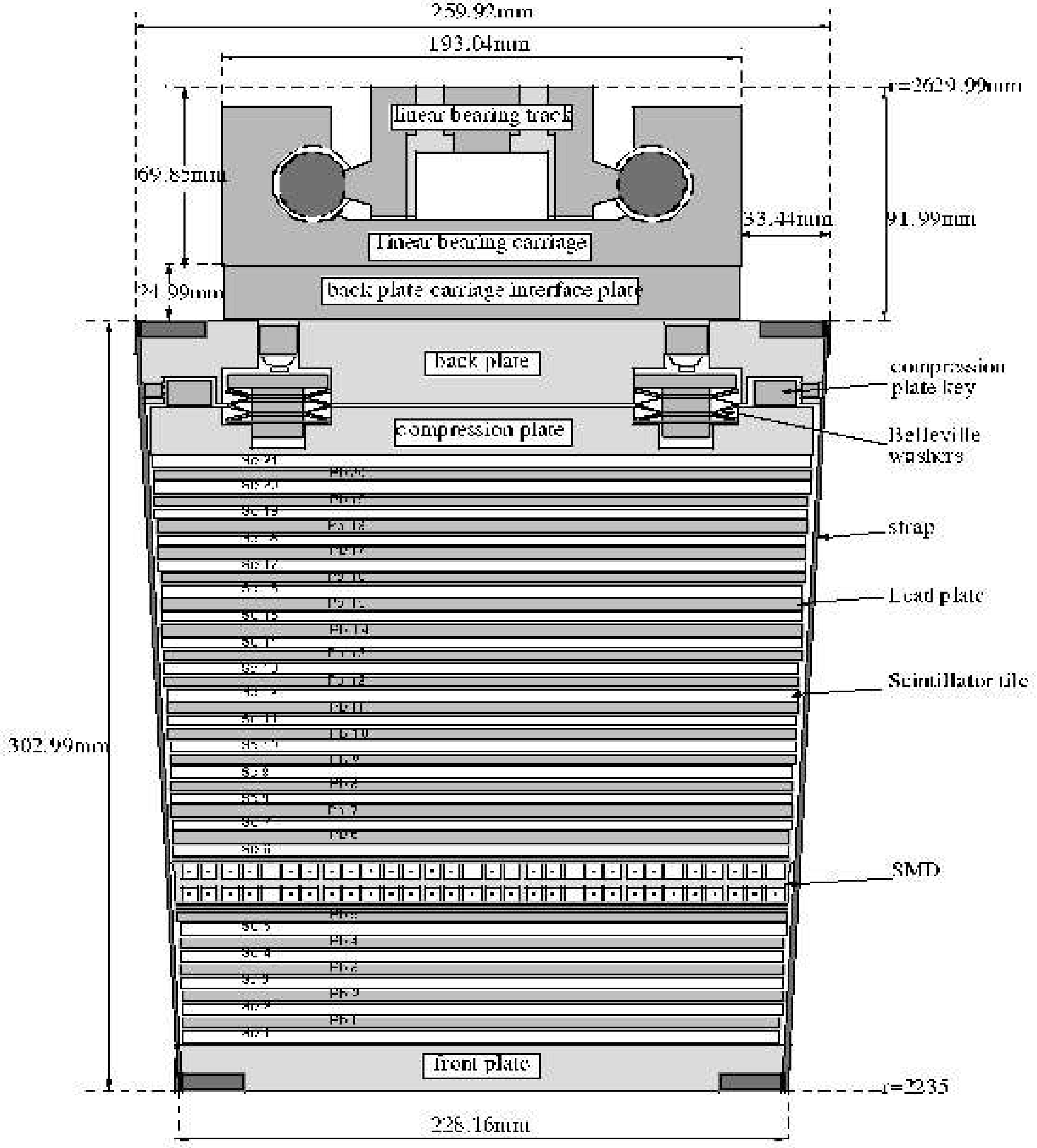

Figure 2.22: Side view of a STAR BEMC module showing the mechanical assembly including the compression components and the rail mounting system. Also shown is the location of the two layers of SMD at a depth of approximately $5X_0$ from the front face at $\eta = 0$.

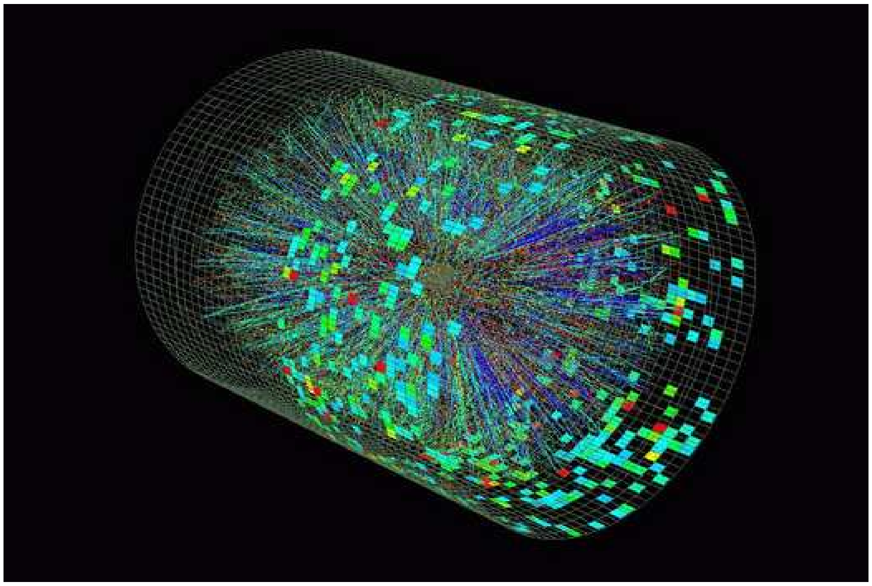

Figure 2.23: The STAR BEMC event display.

center of the interaction diamond. Fig. 2.20 shows a schematic side view of a module illustrating the projective nature of the towers in the η-direction while Fig. 2.21 shows a photograph of the $\eta = 0$ end of a module after assembly, before the light tight covers are put in place.

The BEMC is a sampling calorimeter and the core of each BEMC module consists of a lead scintillator stack and shower maximum detectors situated approximately 5 radiation lengths from the front of the stack. There are 20 layers of 5 mm thick lead, 19 layers of 5 mm thick scintillator and 2 layers of 6 mm thick scintillator. The later ones, which are the thicker scintillator layers, are used in the pre-shower portion of the detector. Fig. 2.22 shows an end view of a module showing the mounting system and the compression components.

BEMC towers provide a precise energy measurement for isolated electromagnetic showers and the high spatial resolution provided by the SMD is essential for π^0 reconstruction, direct photon and electron identification. Information on shower position, shape, signal amplitude and the electromagnetic shower longitudinal development, are provided by the BEMC.

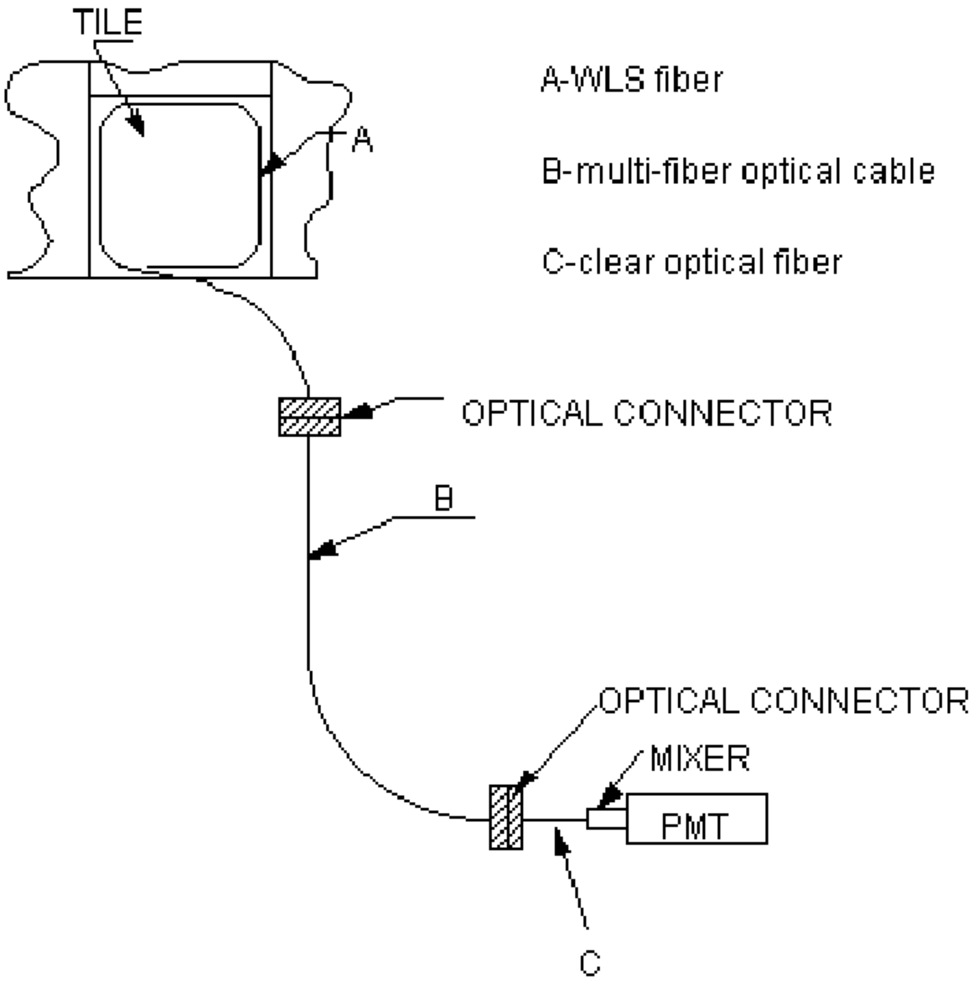

Figure 2.24: Schematic diagram of the BEMC optical system illustrated for a single tile.

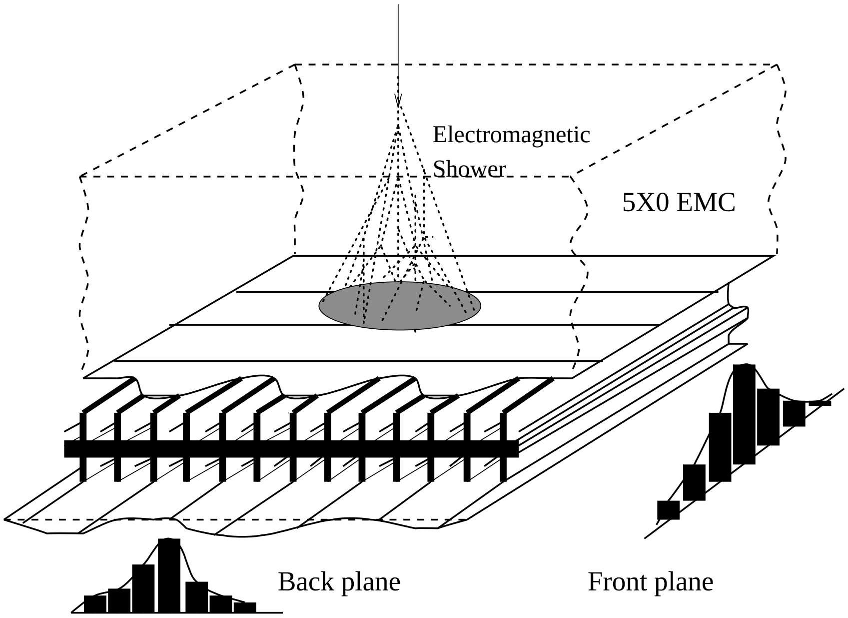

Figure 2.25: Schematic illustration of the double layer STAR BEMC SMD. Two independent wire layers, separated by an aluminum extrusion, image electromagnetic showers in the $\eta-$ and $\phi-$ directions on corresponding pad layers.

Fig. 2.25 shows the conceptual design of the STAR BEMC SMD.

2.3.12 Endcap Electromagnetic Calorimeter (EEMC)

The STAR endcap electromagnetic calorimeter (EEMC) [15] provides full azimuthal coverage for high-p_T photons, electrons and electromagnetically decaying mesons over a pseudo-rapidity range $1.086 \leq \eta \leq 2.00$. It has a scintillating-strip shower-maximum detector (SMD) to provide π^0/γ discrimination over an energy range of 10-40 GeV. The pre-shower and post-shower layers of SMD helps in distinguishing electrons and charged hadrons. The EEMC is crucial for the STAR spin physics program for it's coverage and the jet triggering capabilities.

EEMC is an annular Pb/plastic scintillator sampling calorimeter which is divided into two halves. The geometry is of alternating Pb radiator and scintillator layers. A scintillator strip SMD with high position resolution is located after the fifth radiator plate. Light from the towers and SMD is carried on optical fibers outside the STAR magnet, to photomultiplier tubes mounted on the rear of the pole-tip.

Bibliography

[1] H. Hahn *et al.*, *Nucl. Instr. and Meth. Phys.* **A 499** (2003) 245-263.

[2] K.H. Ackermann *et al.*, *Nucl. Instr. and Meth. Phys.* **A 499** (2003) 624-632.

[3] K. Adcox *et al.*, *Nucl. Instr. and Meth. Phys.* **A 499** (2003) 469-479.

[4] B.B. Back *et al.*, *Nucl. Instr. and Meth. Phys.* **A 499** (2003) 603-623.

[5] M. Adamczyk *et al.*, *Nucl. Instr. and Meth. Phys.* **A 499** (2003) 437-468.

[6] F. Bergsma *et al.*, *Nucl. Instr. and Meth. Phys.* **A 499** (2003) 629.

[7] M. Anderson *et al.*, *Nucl. Instr. and Meth. Phys.* **A 499** (2003) 659-678.

[8] W.R. Leo, Techniques for Nuclear and Particle Physics Experiments, page 23-28, Narosa Publishing House.

[9] R. Bellwied *et al.*, *Nucl. Instr. and Meth. Phys.* **A 499** (2003) 640-651.

[10] L. Arnold *et al.*, *Nucl. Instr. and Meth. Phys.* **A 499** (2003) 652-658.

[11] K.H. Ackermann *et al.*, *Nucl. Instr. and Meth. Phys.* **A 499** (2003) 713-719.

[12] STAR/ALICE RICH collaboration, a ring imaging cherenkov detector for STAR, STARnote 349, 1998.

[13] B. Bonner *et al.*, *Nucl. Instr. and Meth. Phys.* **A 508** (2003) 181-184.

[14] M. Beddo *et al.*, *Nucl. Instr. and Meth. Phys.* **A 499** (2003) 725-739.

[15] C.E. Allgower *et al.*, *Nucl. Instr. and Meth. Phys.* **A 499** (2003) 740-750.

[16] M.M. Aggarwal *et al.*, *Nucl. Instr. and Meth. Phys.* **A 499** (2003) 751-761.

[17] M.M. Aggarwal *et al.*, *Eur. Phys. J.* **C41** (2005) 287-296.

[18] B. Mohanty, Ph.D. Thesis, Institute of Physics, India, 2002.

[19] J. Adams *et al.*, *Phys. Rev. Lett.* **95** (2005) 062301.

[20] J.C. Santiard, ALICE Internal Report, CERN-ECP/94-17.

[21] *Proposal to Install a Forward Pion Detector in STAR*, "http://www.star.bnl.gov/STAR/html/$fpd\_l/$".

[22] F.S. Bieser *et al.*, *Nucl. Instr. and Meth. Phys.* **A 499** (2003) 766.

[23] C. Adler *et al.*, *Nucl. Instr. and Meth. Phys.* **A 499** (2003) 433.

Chapter 3

Transverse Energy Measurement

3.1 Transverse Energy

The transverse energy (E_T) is the energy produced transverse to the beam direction. E_T is an event-by-event variable defined as

$$E_T = \sum_i E_i sin\theta_i \quad and \quad dE_T(\eta)/d\eta = sin\theta(\eta)dE(\eta)/d\eta. \tag{3.1}$$

The sum is taken over all particles produced in an event into a fixed but large solid angle.

To probe the early stages of the produced fireball, it is ideal to take transverse observables like E_T, p_T etc. This is because, before the collision of two nuclei, the longitudinal phase space is filled by the beam particles whereas the transverse phase space is empty. The E_T is produced due to the initial scattering of the partonic constituents of the incoming nuclei and also by the re-scattering among the produced partons and hadrons [1]. The E_T production tells about the explosiveness of the interaction. In addition, the collision centrality can be selected using the minimum-bias E_T distributions.

In this thesis, the transverse energy production is studied for different center of mass energies and with different centralities in order to estimate the initial energy density produced in the collision of two nuclei and to study the particle production mechanism. The initial energy density has been estimated in the framework of

Bjorken boost-invariant hydrodynamic model which has been discussed in Chapter 1. The Bjorken energy density which gives a lower estimate of the energy density produced, has been compared with the lattice QCD calculations in order to know if a state has been achieved where one can search for the deconfinement transition. The details of the analysis procedure and results has been discussed in the subsequent chapters.

3.2 Data Analysis

We have analyzed the 62.4 GeV Au+Au data based on minimum bias Au+Au collisions measured by the STAR detector in the 2004 RHIC run. The detectors used for this analysis include the Time Projection Chamber (TPC) and the Barrel Electromagnetic Calorimeter (BEMC) in the common phase space at mid-rapidity i.e. $0 < \eta < 1$ and with full azimuthal coverage.

3.2.1 Event Trigger

The trigger selection is obtained from the Zero Degree Calorimeters (ZDCs) [23], the Beam Beam Counters (BBCs) and the Central Trigger Barrel (CTB) [22]. The ZDCs are located at ±18m from the interaction point and measure neutron energy. The scintillator based BBCs provide the principal luminosity measurement. The scintillator based CTB surrounds the TPC and measure the charged particle multiplicity at mid-rapidity within $|\eta| < 1$. The coincidence signal from CTB, ZDCs and BBCs provides the minimum bias trigger for Au-Au collisions. For this trigger a vertex cut of $\sim$ 50 cm on BBC (trigger Id: 35007) or on ZDC (trigger Id: 35004) and a ctbSum > 15 cut were used to remove Ultra-Peripheral Collisions (UPC)-like events. The ZDC resolution goes bad at z-distance of $\sim$ 20 cm, so a cut of ±30 cm was used which removes a large fraction of the bias. The trigger efficiency was found to be almost 100%.

3.2.2 Centrality Selection

For any analysis it is desired to take a different detector for centrality selection, other than the detector used for a specific analysis to avoid auto-correlations. TPC and the BEMC are the detectors used for this analysis. Taking FTPC for centrality selection has an advantage as it has large separation in rapidity both from TPC and BEMC. But unfortunately, for the data set under study, FTPC had large gain fluctuation and different electronic losses in east and west sides, which in turn affects the multiplicity distribution. ZDC could not be used for centrality selection as well for its low resolution for high central events. Hence TPC uncorrected mid-rapidity multiplicity, within pseudo-rapidities $|\eta| < 0.5$ and $|V_z| < 30$ cm, was used for the centrality selection. However, auto-correlation is not significant for Au-Au collisions due to large multiplicities.

The events were divided into eight different centrality classes which correspond to fraction of the total geometrical cross section from central to peripheral collisions: $0-5\%, 5-10\%, 10-20\%, 20-30\%, 30-40\%, 40-50\%, 50-60\%, 60-70\%$. Very high peripheral events are not taken for this analysis because BEMC energy deposition corrected for hadronic contaminations, sometimes make the tower energy negative for very peripheral events. This is because the correction is done in a statistical fashion. Table 3.1 enlists the TPC uncorrected multiplicity used for the centrality definitions.

Centrality Bin	TPC RefMult ($\geq$)	N_{part}	N_{bin}
$(0-5)\%$	373	347.4 - 4.4 + 3.7	899.2 - 64.0 + 64.3
$(5-10)\%$	313	293.3 - 7.1 + 5.5	709.6 - 57.7 + 59.6
$(10-20)\%$	222	229.1 ± 8.2	509.5 - 50.3 + 51.9
$(20-30)\%$	154	162.7 - 9.7 + 9.0	319.9 - 39.7 + 42.0
$(30-40)\%$	102	112.5 - 10.5 + 8.2	192.4 - 29.4 + 33.0
$(40-50)\%$	65		
$(50-60)\%$	38		
$(60-70)\%$	38		

Table 3.1: Centrality definitions from different TPC uncorrected reference multiplicity ranges and the corresponding N_{part} and N_{bin} obtained from Glauber model calculations.

3.2.3 Track Selection

TPC is the main tracking detector used for this analysis. The TPC drift volume was located inside the STAR magnet for particle curvature measurement which gives the momentum information. The data were taken at magnetic field $|B_z| = 0.5$ Tesla, where the z-component is parallel to the beam direction. The TPC reconstructed momentum resolution is found to be $\delta p_T/p_T = 0.01 + p_T/(62.4\ GeV/c)$ [5]. For this analysis only primary tracks are taken with a cut on the distance of closest approach (dca): $|dca| < 3$. This is because for initial energy density estimation we need primary particles produced in the collision. This forbids taking the secondary particles which are produced due to decays and re-scatterings at later stages of the fireball evolution. The dca cut significantly reduces the pile up events. The longitudinal z position of the interaction point is determined on-line by the measured time difference in the ZDCs. A cut of 30 cm was used for the z position of the reconstructed primary vertex to ensure nearly uniform detector acceptance. Tracks can leave up to 45 hits on the TPC pad-rows. In this analysis, at least 25 hits are required for each track to avoid track splitting effects. For track fitting, a minimum of 10 fit points has been taken to select good tracks. Tracks to escape from TPC inside the magnetic field of 0.5 Tesla, charged particles have to have a minimum transverse momentum of 0.15 GeV/c. A minimum transverse momentum of $p_T > 0.15$ GeV/c is used in this analysis.

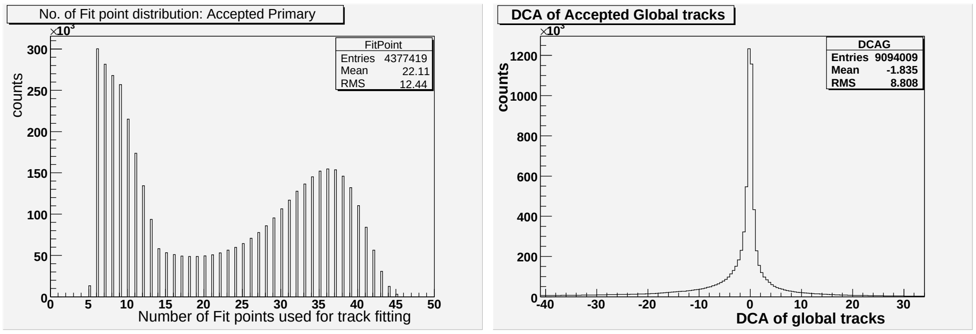

Figure 3.1: The number of fit point distributions for primary tracks (left). The distribution of track dca (distance of closest approach) (right).

Data are analyzed in the common phase space of TPC and BEMC at mid-rapidity with $0 < \eta < 1.0$ over the full ϕ-range.

3.3 Estimation of Transverse Energy

The procedure used in this analysis provides an independent measurement of electromagnetic and hadronic transverse energy on an event by event basis in a common phase space. The hadronic component of transverse energy is obtained from TPC reconstructed tracks after taking into account the long-lived neutral hadrons which couldn't be detected by TPC. The electromagnetic component is estimated from the energy deposited in the electromagnetic calorimeter towers, after correcting for hadronic contaminations by projecting TPC tracks onto the BEMC. In the following sections the procedure to estimate both the components of transverse energy is discussed in details which adds up to give the total transverse energy. This method is identical to that used in Ref. [2].

3.3.1 Hadronic Transverse Energy (E_T^{had})

The hadronic transverse energy, E_T^{had} is defined as

$$E_T^{had} = \sum_{hadrons} E^{had} sin\theta \tag{3.2}$$

where the sum runs over all the hadrons produced in the collision, except π^0 and η for their short life time. θ is the polar angle relative to the beam axis and the collision vertex position. E^{had} is defined for nucleons as kinetic energy, for anti-nucleons as kinetic energy plus twice the rest mass and for all other particles as the total energy [2, 3]. This is given in the following equations. It takes care of the energy of the participant nucleons, thereby making the measured hadronic energy as the hadronic energy produced in the collision.

$$E^{had} = \begin{cases} \sqrt{p^2 + m^2} - m & \text{for nucleons} \\ \sqrt{p^2 + m^2} + m & \text{for anti-nucleons} \\ \sqrt{p^2 + m^2} & \text{for all others} \end{cases}$$

However, experimentally, E_T^{had} is measured using charged particle tracks in TPC by using the equation

$$E_T^{had} = C_0 \sum_{tracks} C_1(ID,p) E_{track}(ID,p) sin\theta \tag{3.3}$$

The sum includes all tracks from the primary vertex in the range $0 < \eta < 1$ and for full azimuthal coverage. C_0 is the correction factor defined as

$$C_0 = \frac{1}{f_{acc}} \frac{1}{f_{p_T Cut}} \frac{1}{f_{neutral}} \tag{3.4}$$

which includes the effective acceptance f_{acc}, the correction $f_{neutral}$ for long-lived neutral hadrons not detected by TPC, and $f_{p_T Cut}$, for the TPC low momentum cutoff. $E_{track}(ID,p)$ is the energy associated with a particular track as defined earlier. This is calculated from the measured momentum and particle identity (ID). The factor $C_1(ID,p)$ is defined as

$$C_1(ID,p) = f_{bg}(p_T) \frac{1}{f_{notID}} \frac{1}{eff(p_T)}, \tag{3.5}$$

where

f_{notID} ≡ corrections for the uncertainty in the particle ID determination
$eff(p_T)$ ≡ momentum dependent tracking efficiency
$f_{bg}(p_T)$ ≡ momentum dependent backgrounds.

The estimation procedures of these correction factors are discussed below.

Estimation of $f_{p_T Cut}$:

Low momentum particles inside the magnetic field, in TPC can't come out because of very high bending of the tracks. The TPC tracking efficiency drops very rapidly for $p_T < 0.15$ GeV/c. In view of the above, in this analysis we have accepted only particles with $p_T > 0.15$ GeV/c. Estimation through HIJING [6] events suggests that this cut excludes 5% of the total E_T^{had}. Finally $f_{p_T Cut}$ is estimated through the formula

$$f_{p_T Cut} = \frac{E_T^{had}\ (particles\ with\ p_T > 0.15\ GeV/c)}{E_T^{had}\ (all\ particles)} \tag{3.6}$$

taking minimum bias events. The value of $f_{p_T Cut}$ is found to be 0.953 ± 0.03. The systematic error on $f_{p_T Cut}$ is estimated by taking simulated tracks with $p_T > 0.15$

GeV/c and calculating E_T^{had} assuming pions with $p = 0$ and $p = 0.15$ GeV/c. This gives a variation of 3% in E_T^{had}.

Estimation of $f_{neutral}$:

Since only the charged tracks detected by the TPC are used in this analysis, we need to correct E_T^{had} to include the contribution from the long-lived neutral hadrons, principally $n(\bar{n})$, K_L^0, K_S^0, and $\Lambda(\bar{\Lambda})$. The correction factor is defined as

$$f_{neutral} = \frac{E_T^{had}\ (charged)}{E_T^{had}\ (charged) + E_T^{had}\ (neutral)} \tag{3.7}$$

HIJING simulation shows this factor doesn't change much from 200 GeV to 62.4 GeV Au+Au collisions and the value of $f_{neutral}$ is found to be 0.82 ± 0.03 [2].

Particle Identification and Estimation of f_{notID}:

As discussed in section 2.3.1, TPC uses the ionization energy loss of different hadrons to separate them. The charge collected for each hit on a track is proportional to the energy loss of the particle. At low momentum, the energy loss is approximately inversely proportional to the square of particle velocity. The particle identification procedure has been already discussed in section 2.3.1, which uses the measurement of momentum and truncated mean specific ionization. This procedure could only separate particles up to $p_T < 1$ GeV/c. For $p_T < 1$ GeV/c, assignment was made to the most probable particle type relative to the Bethe-Bloch expectation. Particles were assumed to be pions if $< \frac{dE}{dx} >$ differed from this expectation by more than three standard deviations, or if p_T was greater than 1 GeV/c. The uncertainty in this procedure was gauged by calculating E_T^{had} for $p_T < 1$ GeV/c both with correct particle assignments and with all particles assumed to be pions i.e.

$$f_{notID} = \frac{E_T^{had}\ (p_T < 1\ GeV/c,\ with\ correct\ PID)}{E_T^{had}\ (p_T < 1\ GeV/c, all\ particles\ assumed\ to\ be\ pions)} \tag{3.8}$$

The correction factor f_{notID} found by this procedure for 62.4 GeV Au+Au collision is $f_{notID} = 0.991 \pm 0.02$. This was estimated from data. As this correction factor was calculated from low momentum particles and hence it doesn't account for the centrality variations in the particle ratios with $p_T > 1$ GeV/c [4]. On the contrary, particles with $p_T > 1$ GeV/c only account for 20% of the total number of particles. When we take care of the centrality dependence in the increase in particle ratios i.e.

p/π, K/π ratios at higher p_T, the estimated E_T^{had} only increases by the order of 2%, which is within the systematic error of f_{notID}.

Estimation of $f_{bg}(p_T)$:

The correction factor $f_{bg}(p_T)$ for background, takes care of electrons, weak decays and secondary tracks that are mis-identified as primary. This however depends on the type of the track and is divided into two classes. The first is for electrons which are mis-identified as hadrons. The second is due to weak decays which have been included in $f_{neutral}$ and therefore must be excluded from the primary tracks to avoid double counting of their contribution to hadronic energy. Assuming that this factor doesn't change much from 200 GeV Au+Au data to 62.4 GeV, we have taken the estimation from STAR 200 GeV transverse energy paper [2]. These values are $f_{bg}(p_T) = 0.84 \pm 0.02$ $(p_T \leq 0.25\ GeV/c)$, 0.94 ± 0.02 $(0.25 \leq p_T \leq 1\ GeV/c)$.

Estimation of $eff(p_T)$:

TPC reconstruction efficiency, $eff(p_T)$, was determined by embedding simulated tracks into real events and comparing the simulated input with that of the final reconstructed event. In order to evaluate the effect of different particle species on the reconstruction efficiency, pions, kaons and protons are embedded in the real events. The final charged track efficiency correction is the number averaged over all particle species weighted by their relative population. This factor depends on the transverse momentum of the tracks and the track density in phase space. For central events, the efficiency is 0.70 ± 0.04 for tracks with $p_T = 0.25$ GeV/c and reaches a plateau at about 0.8 for $p_T > 0.4$ GeV/c. It is interesting to note that although the track density changes from 200 GeV Au+Au collisions to 62.4 GeV Au+Au collisions the track reconstruction efficiency is almost the same [2, 4]. This efficiency correction includes the efficiency of track reconstruction, the probability of track splitting, correction for ghost tracks and the dead regions of the TPC. The resulting systematic uncertainty in E_T^{had}, taking into account all corrections added in quadrature is obtained to be 8.5%. Table 3.2 enlists all individual corrections and the uncertainties in their measurements. The systematic uncertainties from the dynamic cuts used in the analysis, when added in quadrature give an error of 5.8% in E_T^{had}. This is discussed separately in subsequent sections. The final systematic uncertainty in the estimation of E_T^{had} is

Correction Factor	Correction
$f_{p_T Cut}$	0.953 ± 0.03
$f_{neutral}$	0.820 ± 0.03
f_{notID}	0.991 ± 0.02
$f_{bg}(pT)$	0.84 ± 0.02 ($p_T \leq 0.25$ GeV/c)
	0.94 ± 0.02 ($0.25 \leq p_T \leq 1$ GeV/c)
$eff(p_T)$	0.70 ± 0.04 ($p_T \leq 0.25$ GeV/c)
	0.80 ± 0.04 ($0.25 \leq p_T \leq 1.0$ GeV/c)

Table 3.2: Correction factors and their estimated values with uncertainties for E_T^{had} for the 5% most central collisions.

found to be 10.3%.

The final E_T^{had} is corrected for vertex reconstruction efficiency which depends on the number of tracks measured in TPC. This varies from peripheral to central events. For central events, the vertex reconstruction efficiency is 94.5%. For top 5% central events, the event-by-event resolution in E_T^{had} is found to be 9%. The estimated values of $dE_T^{had}/d\eta$ for different centralities in Au+Au collisions at $\sqrt{s_{NN}}$ = 62.4 GeV are given in Table- 3.5.

3.3.2 Electromagnetic Transverse Energy (E_T^{em})

The electromagnetic transverse energy is the sum of transverse energy of electrons, positrons and photons. The largest fraction in this sector comes from π^0 decays. Electrons and positrons are included because most of them are produced in the conversion of photons in the detector materials. Photons and electrons deposit their full energy in the BEMC. Charged and neutral hadrons can also deposit significant fraction of their energy in the BEMC. Hence, this contribution must be subtracted to permit a measurement of E_T^{em}. In order to remove the hadronic contribution from the E_T^{em} measurement, the full spatial profile of the energy deposition of identified hadrons in EMC has been studied. An extensive experimental database of hadronic shower clusters in the calorimeter has been obtained, which, with the help of TPC tracking, allow a correction of the hadronic background in the calorimeter [2].

3.3.2.1 The BEMC Calibration

The BEMC has a total of 4800 towers. The gain of each tower can have different values due to i) the variation in their electronic gains, ii) the variation in operating voltage or iii) could be due to some other intrinsic factors. Hence, there is a requirement of normalizing the gain of each tower before the real data taking. This is called gain calibration of the BEMC. The methods of calibration of BEMC is discussed in brief in the following paragraphs.

The hadronic particles produced in the heavy ion collisions, when interact with BEMC, deposit a widely fluctuating fraction of their energy through hadronic showers. In addition, $\sim$ $30-40\%$ of relativistic charged hadrons penetrate the entire depth of the BEMC without hadronic interaction. However, when such a non-showering charged hadron has sufficient momentum, it will behave like a minimum ionizing particle (MIP). When these MIPs traverse through the scintillator layers, deposit their total energy uniformly. This energy deposition (MIP peak) is nearly independent of the incident momentum and the particle species. It varies linearly with the total path length covered in the scintillator. Due to the projective nature of the BEMC towers, the total length of the scintillator increases with η and hence the MIP peak. The absolute energy of the MIP peak and it's η dependence is determined from the cosmic tests and from the test beam measurements [8].

The above factors along with the high yield of charged hadrons, makes it feasible to use high energy MIPs for calibration and continuous monitoring of variations in the BEMC tower gains.

The method of MIP-calibration requires that the initial gains should be set so that MIP peaks from penetrating charged particles, should sit somewhere within digitizers' (ADC) ranges, reasonably far from their lower and upper limits. The calibration using MIP-hits has two stages. In the first stage, a sample of BEMC modules is exposed to an external beam (in STAR, it is the AGS beam at BNL). The external beam should consists of hadrons, electrons and muons in a selected momentum range. The ratios of each tower responses to MIP's and electron hits i.e. MIP/e-ratios are measured simultaneously. Here "MIP" is the MIP-peak position and the notation "e" is used for the ratio $S_e(E_e)/E_e$, where S_e is the mean BEMC signal from electrons of energy

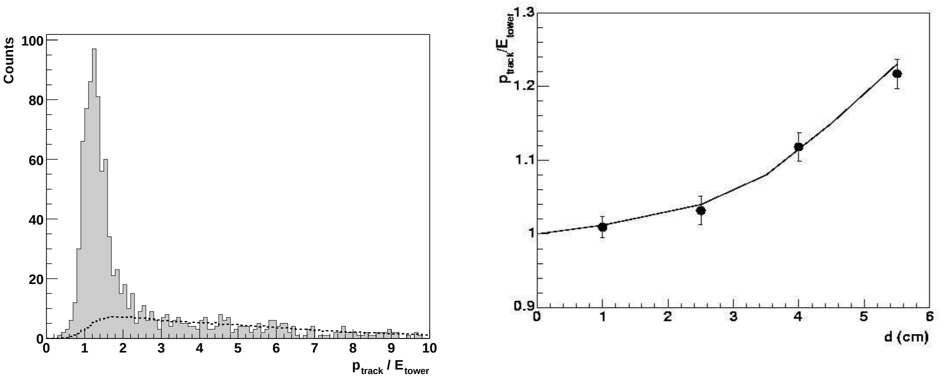

Figure 3.2: a) A typical p/E_{tower} spectrum for electron candidates, selected through dE/dx from the TPC, with $1.5 < p < 5.0$ GeV/c. A well-defined electron peak is observed and the dashed line corresponds to the hadronic background in the dE/dx-identified electron sample. b) Data point are the measured p/E_{tower} electron peak positions as a function of the distance to the center of the tower. The solid line is a calculation based on full GEANT simulation of the detector response to electrons. Fig. Ref. [2]

E_e. Thus, the MIP/e-ratio represents the energy of electrons which would generate in the BEMC, the same mean signal as MIPs. In the second stage, after the BEMC modules are installed in STAR, samples of MIP-hits as close as possible to those in the test beam are accumulated for each tower and the positions of the resulting MIP peaks are measured from real events from RHIC runs. This step essentially completes the procedure of transferring beam-test results to STAR. For those towers already exposed to test beam, their responses to electron hits (momenta used in the test beam-stage) can immediately be predicted, using the known MIP/e-ratios that have been measured from the test beam. For all other modules, these ratios are expected to be close to those of the tested ones, provided that the key design tolerances are kept at the module manufacturing stage.

MIPs of $p_T \sim 1$ GeV/c are used for the calibration purposes to make an compromise between the particle yield p_T and their utility. This is because, we can't choose very low p_T MIPs, as they hit BEMC at very large angles for their deflection in high STAR magnetic field. On the other hand, when the p_T-threshold is chosen very high, the useful event rate would be very low because of the steep drop of particle yield with high p_T.

The absolute calibration of BEMC is also done by selecting identified electron tracks in the TPC, in a wider momentum range ($1.5 < p < 5.0$ GeV/c). The selection of electron candidates in TPC is done by the dE/dx measurements. The purity of electron candidates in this momentum range is poorer than it is for the low momentum ones. However, the hadron rejection factor obtained from the TPC dE/dx provides a clear electron signal in the calorimeter. The Bethe-Bloch predictions for dE/dx of electrons and heavy particles show that the main background in this momentum range comes from deuterons and heavier particles as well as the tails in the distributions of protons and lower mass particles. Tracks with number of space points greater than 25 are used in this procedure to reduce systematic uncertainties. In addition, such long tracks show better dE/dx-resolution. It is also required that the tracks should be isolated in a 3×3 tower patch in the calorimeter.

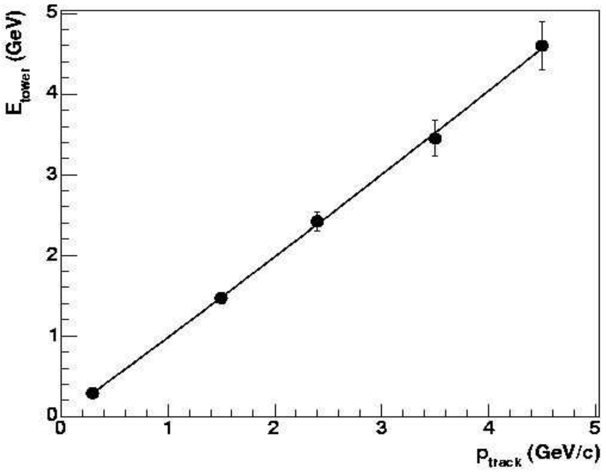

Figure 3.3: The data points show measured energy deposited by electrons in the tower as a function of the momentum for distances to the center of the tower smaller than 2.0 cm. The first point is the electron equivalent energy of the MIPs. The solid line is a second order polynomial fit of the data [2].

For a better accuracy of electron identification, finally the energy deposition by a track in the BEMC tower (E_{tower}) is compared to the momentum of the track (p) in the momentum range $1.5 < p < 5.0$ GeV/c. Fig. 3.2 (a) shows the p/E_{tower} spectrum for the electron candidates, where a well-defined electron peak is observed. The residual hadronic background in this figure is evaluated by shifting the dE/dx selection window toward the pion region. The obtained hadronic background is shown in the figure as the dashed line. The peak position is not centered at 1, after the hadronic background subtraction. This shows the leakage of energy to the neighboring towers which are not taken into account in this procedure. The amount of leakage depend on the distance to the center of the tower hit by the electron and will shift the peak position to higher values as this distance increases. This effect is well-reproduced by the GEANT simulations of the detector response when it is hit by electrons in the momentum range used in this calibration procedure. This is shown by Fig. 3.2 (b). This figure also shows the position of the electron p/E_{tower} peak as a function of this distance. The solid line is a prediction from GEANT simulations. Fig. 3.3 shows the energy deposited in the calorimeter tower as a function of its momentum for electrons in the case where the distance to the center of the tower is less than 2.0 cm. (A distance of 5.0 cm and 7.5 cm correspond to the border of the tower at $\eta = 0$ and $\eta = 1$ respectively.) The first point is the electron equivalent energy of the MIPs. A fit to the data with a second order polynomial i.e. $f(x) = a_0 + a_1x + a_2x^2$ is represented by the solid line.

The combination of the MIP calibration and the electron calibration of the BEMC, gives an overall systematic uncertainty of less than 2% on the total energy measured by the calorimeter. The stability of the tower response was evaluated by monitoring the time dependence of the shape of the raw ADC spectra for each tower. This is the tower response to all particles that reach the calorimeter. The overall gain variation of the detector was less than 5% for the entire RHIC run.

3.3.2.2 The Hadronic Contaminations in BEMC Energy

As discussed earlier, hadrons produced in the collisions traverse through the TPC and then hit the BEMC, as both the detectors share a common phase space and deposit part of their energy in BEMC. In order to measure the electromagnetic transverse energy it is essential to subtract the hadronic energy deposited in the calorimeter. For charged hadrons, the hit locations on the calorimeter are well determined and in case of an isolated hadron, a cluster of energy is identified easily. However, in the high density environment of Au+Au collisions, it is difficult to identify a hadron track. In this case, an average energy deposition based on the measured momentum of the incident track is subtracted out. As one is interested in the cumulative distribution averaged over many events, where each event has many tracks, this averaged correction results in a negligible contribution to the uncertainty in the measured electromagnetic energy. The following is the procedure which explains, how the hadronic contaminations in BEMC is taken care of [2].

The spatial and energy distributions of hadronic showers in the calorimeter is studied both from the real data and from the GEANT simulations. A library of separate profiles for pions, kaons, protons and anti-protons was obtained from GEANT simulations of the detector response in the STAR environment (GSTAR). Events were chosen with a uniform momentum distribution in the range $0 < p < 10$ GeV/c and with vertex positions limited by $|z_{vertex}| < 20$ cm. The constraint on the longitudinal co-ordinate of the vertex ensures that the trajectory of a particle would extrapolate through only one tower of BEMC. Because of the fact that BEMC has a projective geometry, this constraint on the extrapolated track is strongly related to the vertex constraint. The simulated tracks were projected on BEMC using a helix model for the particle trajectory in the magnetic field. The energy distributions and the corresponding mean values are then obtained as a function of the momentum, p, the pseudo-rapidity of the BEMC towers, η and the distance of the incident hit point to the center of the tower, d. The distributions were then binned in the intervals of $\Delta\eta = 0.2$. For all particle species, the total mean deposited hadronic energy in a particular tower has been found to increase approximately linearly with the momentum. This shows very little dependence on η and decreases with increasing d. From the real data, the hadronic shower profiles are obtained from the minimum-bias events, by projecting tracks on the BEMC. This is achieved by accepting tracks which are isolated in a 5×5 tower patch to ensure that the energy in the towers are only from one particle and calculating the energy distributions and the mean values. Profiles for all particles excluding electrons and positrons, for both positive and negative tracks were recorded with good statistics up to $p = 2.0$ GeV/c.

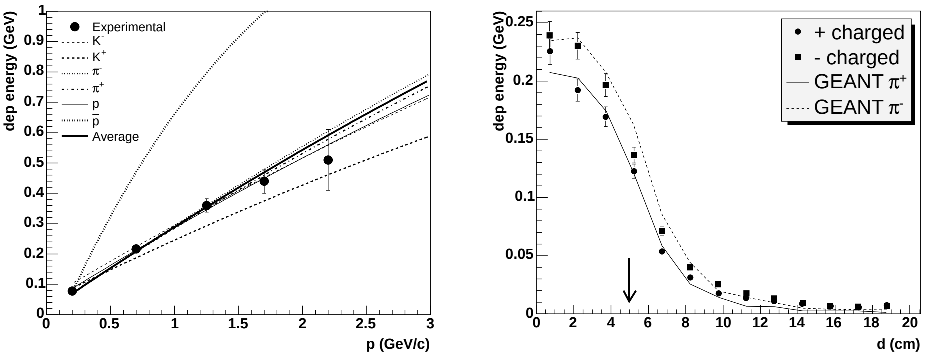

Figure 3.4: a) The mean values of the energy deposited in the BEMC by various hadronic species as a function of momentum. This is from GEANT simulations. b) The spatial profiles of the energy deposition in the BEMC as a function of the distance (d) from the hit point to the center of the tower for π^-, π^+ from simulations and for positive and negative hadrons from data. The arrow indicates the distance corresponding to the border of a tower in $0 < \eta < 0.2$.

Fig. 3.4 (a) shows the mean energy deposited for different particles from GEANT simulations, as a function of p, for a fixed η and d. An average curve, based on the relative yield of different particles is also presented. Small differences are observed for most of the particles except the anti-proton, for which additional annihilation energy is expected. The solid points are the deposited energy obtained from experimental data for charged hadrons. The experimental profiles for charged hadrons agree quite well with the averaged profile. Fig. 3.4 (b) shows the simulated profiles for π^-, π^+ and the experimental profiles for all positive and negatively charged tracks in the momentum range $0.5 < p < 1.0$ GeV/c, as a function of d. Experimental profiles are well described by simulations, except for a normalization factor of the order of 20% for $0 < p < 0.5$ GeV/c and 5% for $p > 0.5$ GeV/c. After renormalization, all experimental profiles up to $p = 2.0$ GeV/c are seen to be in good agreement with simulation. Hence the renormalized simulated profiles are used to allow smooth interpolation in the data analysis and for extrapolation to allow corrections for higher

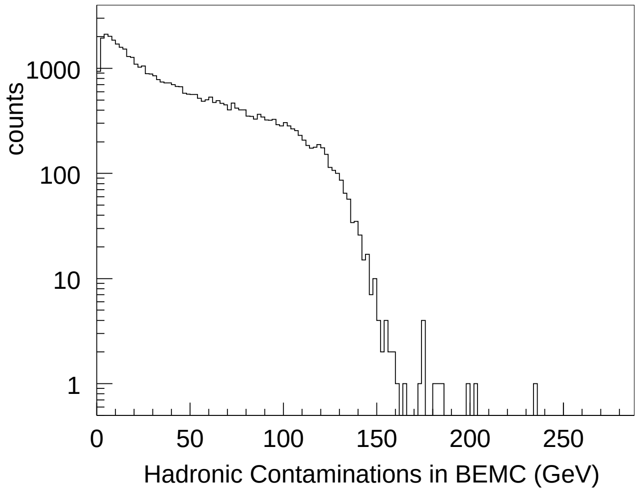

Figure 3.5: The event-by event distribution of the hadronic energy deposited in the BEMC for 62.4 GeV Au+Au minimum-bias collisions.

momentum tracks. Since the interval $p < 2.0$ GeV/c contains 98% of the tracks, the magnitude of this extrapolation is small for the E_T measurement.

Fig. 3.5 shows the distribution of the hadronic energy deposited in the BEMC for minimum-bias events in 62.4 GeV Au+Au collisions. This is the hadronic contamination in the electromagnetic energy measured in BEMC.

3.3.2.3 Measurement of (E_T^{em})

The electromagnetic transverse energy, E_T^{em} is defined as

$$E_T^{em} = \sum_{towers} E_{tower}^{em} \ sin(\theta_{tower}), \tag{3.9}$$

where, E_{tower}^{em} is the electromagnetic energy measured in an BEMC tower and θ_{tower} is the polar angle of the center of the tower relative to the beam axis and the collision vertex position. However, experimentally E_T^{em} is given by

$$E_T^{em} = \frac{1}{f_{acc}} \sum_{towers} (E_{tower} - \Delta E_{tower}^{had}) \ sin(\theta_{tower}), \tag{3.10}$$

where, the sum over BEMC towers corresponds to $0 < \eta < 1$ with full azimuthal coverage i.e. the common phase space of TPC and BEMC.

f_{acc} $\equiv$ the EMC acceptance correction factor,

E_{tower} $\equiv$ the energy measured by an BEMC tower and

ΔE^{had}_{tower} $\equiv$ total correction for each tower to exclude the hadronic contribution to tower energy.

The ΔE^{had}_{tower} is given by

$$\Delta E^{had}_{tower} = \frac{1}{f_{neutral}} \sum_{tracks} \frac{f_{elec}(p_T)}{eff(p_T)} \, \Delta E(p, \eta, d) \ , \tag{3.11}$$

where, $\Delta E(p, \eta, d)$ is the energy deposited by a track projected on an BEMC tower as a function of its momentum p, pseudo-rapidity η and distance d to the center of the tower from the track hit point. This track projection takes into account the magnetic field within which the particles are traversing. $f_{elec}(p_T)$ is a correction factor to exclude the electrons that are misidentified as hadrons in the particle identification procedure through dE/dx method and therefore should not be added to ΔE^{had}_{tower}. The procedure of estimation of this correction factor is the same as described in the previous section to exclude the real electrons from the E^{had}_T measurement. $eff(p_T)$ is the TPC track reconstruction efficiency as discussed previously. The factor $f_{neutral}$ is the correction factor to exclude the long-lived neutral hadron contributions. This is given by

$$f_{neutral} = \frac{\Delta E^{charged}_{tower}}{\Delta E^{charged}_{tower} + \Delta E^{neutral}_{tower}} \tag{3.12}$$

Here $\Delta E^{neutral}_{tower}$ is defined as the energy deposited by all long-lived neutral hadrons. Through HIJING simulation we have observed that this factor doesn't change from 200 GeV Au+Au collision to 62.4 GeV Au+Au collisions. Therefore for this analysis, we have used the value of $f_{neutral}$ used in 200 GeV Au+Au analysis [2]. The value of this correction factor is 0.86 ± 0.03.

The estimation of hadronic correction for charged tracks, $\Delta E(p, \eta, d)$, is based primarily on measured hadronic shower profiles with GEANT simulations used for interpolation between measurements and extrapolation beyond $p = 2$ GeV/c. The systematic uncertainty for this correction to E_T^{em} is estimated from the observed uncertainties in the calculation of hadronic profile at points in the shower library where full measurements were made. After normalization, a 5% systematic uncertainty is found to be consistent with the comparison of measured and calculated shower profiles. Unlike the correction for p_T cut-off for E_T^{had}, there is no correction for p_T cut-off in the hadronic background subtraction in the electromagnetic energy. Low p_T tracks will not reach the calorimeter because of the strength of the magnetic field, and therefore will not deposit any energy in the calorimeter.

The EMC acceptance correction is given by

$$f_{acc} = \frac{Number\ of\ working\ EMC\ towers}{Total\ number\ of\ EMC\ towers} \tag{3.13}$$

The number of working towers, which affects the acceptance factor, can fluctuate in case of electronic readout failures. The value of f_{acc} is estimated to be 0.87 ± 0.02. The systematic error in f_{acc} is estimated by measuring it's variation over several runs. The systematic uncertainty due to the calibration of the calorimeter is of the order of 2% and this uncertainty contributes to the uncertainty in E_T^{em}. The systematic uncertainty due to the electron background track correction is negligible ($< 0.5\%$) [2].

Assuming that all the sources of uncertainties are uncorrelated, when added in quadrature the overall systematic uncertainty estimate for E_T^{em} is 3.0%. All the corrections and corresponding systematic uncertainties are summarized in Table 3.3. The final E_T^{em} is then corrected for the 94.5% vertex reconstruction efficiency. For the 5% most central collisions, the event-by-event resolution in E_T^{em} is found to be 15.6%. The measured values of $dE_T^{em}/d\eta$ for different centralities in Au+Au collisions at $\sqrt{s_{NN}} = 62.4$ GeV are given in Table- 3.5. In order to evaluate the hadronic background subtraction procedure and estimate the event-by-event resolution of the reconstructed electromagnetic energy, simulations have been performed where we compare the reconstructed E_T^{em} energy and the input HIJING. The event-by-event resolution improves when the event becomes more central. The main factors that determine this resolution are the hadronic energy subtraction, the corrections for tracking efficiency and the corrections for long-lived neutral hadrons [2].

Correction Factor	Correction
f_{acc}	0.87 ± 0.02
$f_{neutral}$	0.86 ± 0.03
$f_{elec}(p_T)$	$0.96 \pm < 0.005$ ($p_T \leq 0.25$ GeV/c)
	$1.00 \pm < 0.005$ ($0.25 \leq p_T \leq 1$ GeV/c)
$eff(p_T)$	0.70 ± 0.04 ($p_T \leq 0.25$ GeV/c)
	0.80 ± 0.04 ($0.25 \leq p_T \leq 1.0$ GeV/c)

Table 3.3: Correction factors and their estimated values with uncertainties for E_T^{em} for the 5% most central collisions.

3.3.3 Total Transverse Energy (E_T)

The sum of E_T^{had} and E_T^{em} is the total transverse energy, E_T. The transverse energy distributions (Fig. 3.6)show a peak and a sharp drop off at the lower energy edge corresponding to the most peripheral collisions with grazing impact. It reaches a broad, gently sloping plateau at the middle which corresponds to the mid-central collisions (mid-range of impact parameters). This is dominated by the nuclear geometry. For higher values of E_T, which corresponds to the most central collisions (where the colliding nuclei fully overlap), the shape of the distribution has a “knee” leading to a falloff which is very steep for larger acceptances and less steep for smaller acceptance. This shape is mostly determined by statistical fluctuations and depends on the experimental acceptance [7]. Figs. 3.6 shows the event-by-event distribution of transverse energy and its components. Fig. 3.6 (lower panel and right figure) shows E_T distributions for different centrality classes defined by the percentage of the total cross-section as discussed earlier (Table. 3.1). The shaded area corresponds to the most 5% central collision.

Fig. 3.7 shows the correlation plots for both the components of transverse energy and the total transverse energy for $\sqrt{s_{NN}} = 62.4$ GeV Au+Au collisions.

Combining both the components of transverse energy and after properly taking into account all the systematic uncertainties, we estimate a combined systematic uncertainty of 11% in E_T. For the top 5% central collisions, $< dE_T/d\eta|_{\eta=0.5} > \; = \; <$

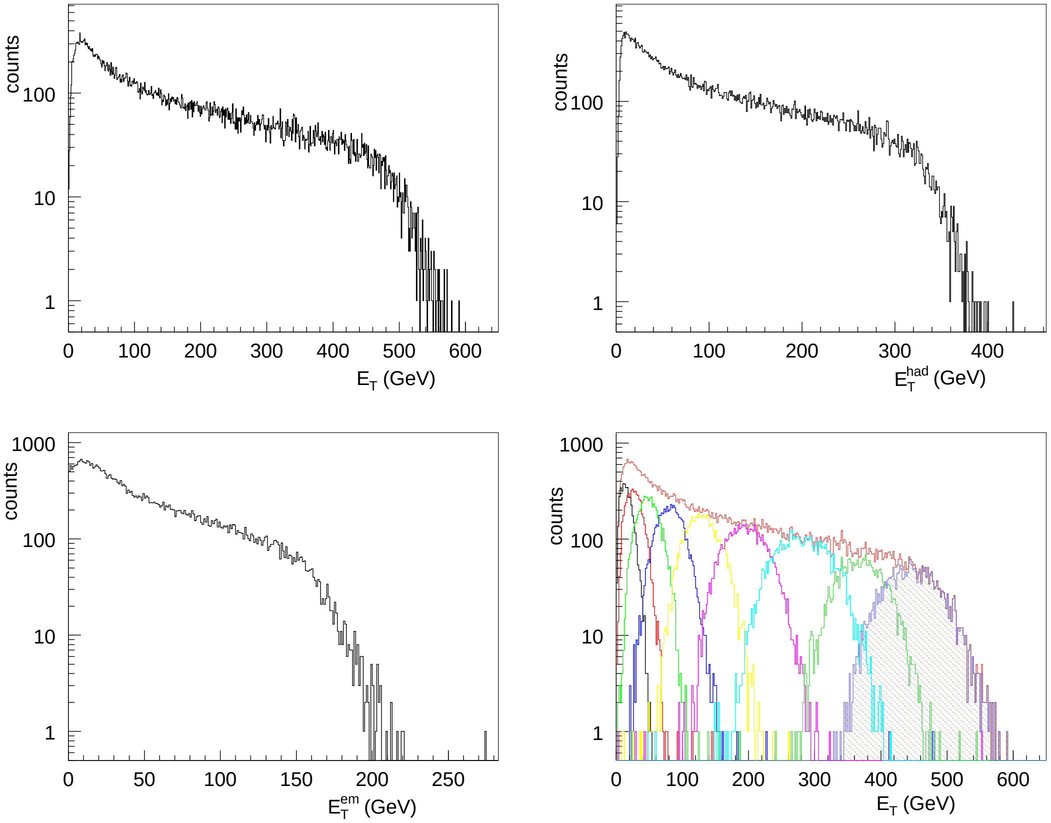

Figure 3.6: Upper panel: Minimum bias distributions of total transverse energy (left side) and hadronic transverse energy (right side), Lower panel: Minimum bias distributions of electromagnetic transverse energy (left side) and total transverse energy for all centrality classes (right side) for $\sqrt{s_{NN}}$ = 62.4 GeV Au+Au collisions. The shaded area corresponds to the top most central bin.

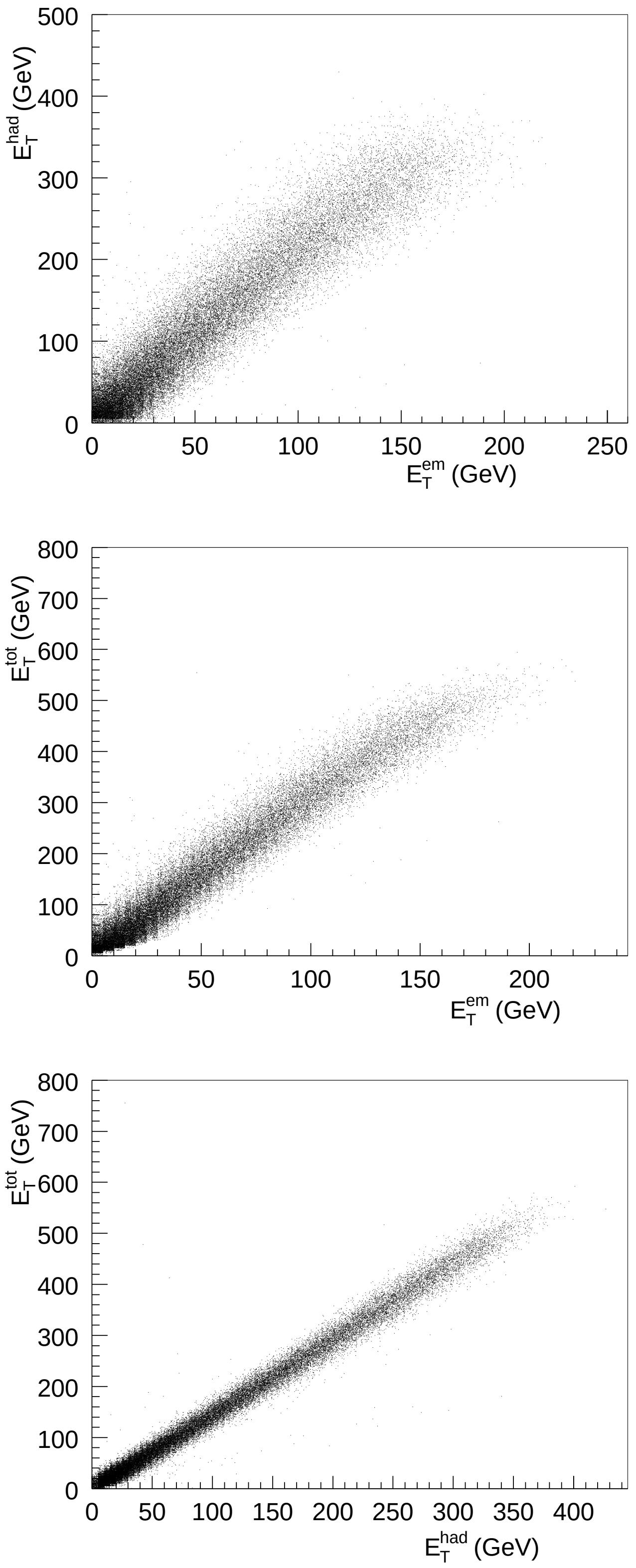

Figure 3.7: The correlation plots for E_T^{em} and E_T^{had} (top), E_T^{em} and E_T (middle) and E_T^{had} and E_T (bottom); for $\sqrt{s_{NN}} = 62.4$ GeV Au+Au collisions.

$E_T >_{5\%} \;=\; 474 \pm 51\ (syst) \pm 1\ (stat)$ GeV. The measured values of $dE_T/d\eta$ for different centralities in Au+Au collisions at $\sqrt{s_{NN}} = 62.4$ GeV are given in Table- 3.5. For the 5% most central collisions, the event-by-event resolution in E_T is found to be 8.9%.

3.4 Results and Discussions

3.4.1 Variation of $< dE_T/d\eta|_{\eta=0.5} >$ per N_{part} pair with Centrality of the Collision

The variation of $< dE_T/d\eta|_{\eta=0.5} >$ per N_{part} pair as a function of N_{part} (obtained from Monte Carlo Glauber calculations) is shown in Fig. 3.8. Here, the result for $\sqrt{s_{NN}} = 62.4$ GeV Au+Au collisions is shown together with similar measurements from Pb+Pb collisions at $\sqrt{s_{NN}} = 17.2$ GeV from WA98 [16], Au+Au collisions at $\sqrt{s_{NN}} = 130$ GeV from PHENIX [17] and Au+Au collisions at $\sqrt{s_{NN}} = 200$ GeV from STAR [2]. The STAR 200 GeV and 62.4 GeV measurements are at $0 < \eta < 1$ and measurements by WA98 and PHENIX are at $\eta = 0$. The dotted line is the EKRT model [13] estimation for 62.4 GeV Au+Au collisions. The measured values of $< dE_T/d\eta|_{\eta=0.5} >$ per N_{part} pair for different centralities in Au+Au collisions at $\sqrt{s_{NN}} = 62.4$ GeV are given in Table- 3.6.

The EKRT model, which is based on final state gluon saturation, predicts that for more central collisions, for both charge particle multiplicity per participant pair and E_T density in pseudo-rapidity per participant pair will decrease. The hydrodynamic work plays a role during the expansion of the fireball by decreasing the observed E_T relative to the initially generated E_T [13]. However, the transverse expansion (radial flow) at later times compensates for this effect [13, 9]. According to the EKRT model, the observed E_T in terms of the center of mass energy ($\sqrt{s_{NN}}$) and the system size (A) is given by

$$E_T^{b=0} = 0.46\ A^{0.92}(\sqrt{s})^{0.40}(1 - 0.012\ lnA\ +\ 0.061\ ln\sqrt{s}) \tag{3.14}$$

The centrality dependence of the above equation can be approximated by replacing

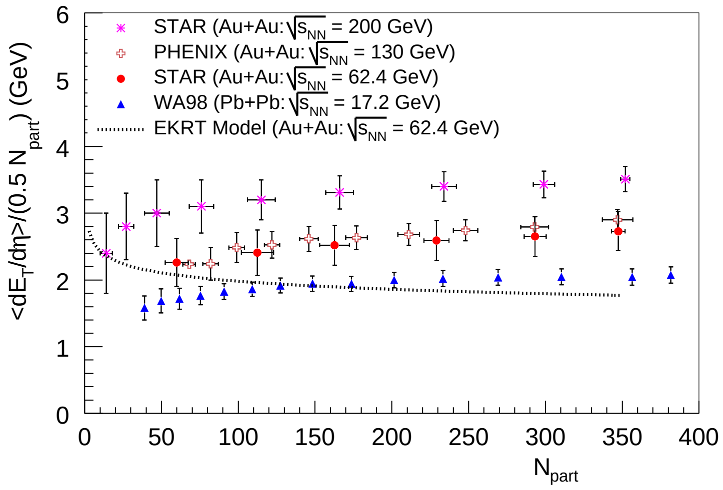

Figure 3.8: $< dE_T/d\eta|_{\eta=0.5} >$ per N_{part} pair vs N_{part}. The dotted line is the estimation from EKRT model (Eqn. 3.14), for 62.4 GeV Au+Au collisions.

A by $N_{part}/2$ [11]. The EKRT model is seen not to agree with the data. It shows a significantly different behavior in the centrality dependence. A more precise comparison of the system size dependence of E_T predicted by the EKRT model, requires either a further refinement of the Glauber calculations or measurements for central collisions with varying mass A.

3.4.2 Why to Compare the Data with EKRT Model?

The bulk hadron multiplicities measured at mid-rapidity in central Au+Au collisions at $\sqrt{s_{NN}}$ = 200 GeV is comparatively lower than the expectations of models with “mini-jet” dominated scenarios, soft Regge models (without accounting for strong shadowing effects) or extrapolation from an incoherent sum of proton-proton collisions. These models fail to explain the data for bulk hadron multiplicities measured at mid-rapidity in central Au+Au collisions. The data show a lower value as expected from these models [12].

Whereas, models like EKRT, based on gluon saturation which takes into account a reduced initial number of scattering centers in the nuclear parton distribution functions agree well with the experimental data.

3.4.3 Variation of $< dE_T/dy >$ per N_{part} pair with Center of mass Energy

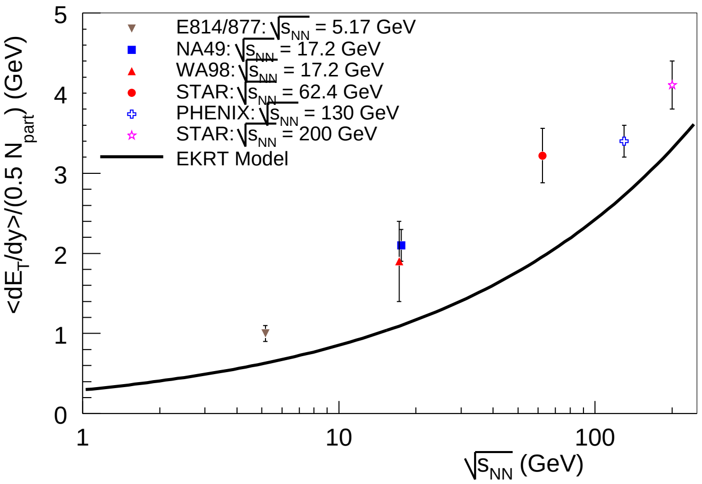

Figure 3.9: $< dE_T/dy >$ per N_{part} pair vs $\sqrt{s_{NN}}$ for central events. The solid line is the EKRT [13] model prediction.

The variation of $< dE_T/dy >$ per participant pair with the center of mass energy is shown in Fig. 3.9. For the top 5% central events in 62.4 GeV Au+Au collisions, the value of $< dE_T/d\eta >$ is estimated and $< dE_T/dy >$ is measured using a factor of 1.18 for the conversion of pseudo-rapidity phase space to rapidity phase space, using HIJING simulations. The value of $< dE_T/dy >$ per participant pair for the top 5% central Au+Au collisions at $\sqrt{s_{NN}} = 62.4$ GeV is estimated to be 3.22 ± 0.34 GeV. This result is compared with results from other experiments from AGS to RHIC [14, 15, 16, 17] for the most central collisions. The result is consistent with the fact that $< dE_T/dy > /(0.5\ N_{part})$ increases logarithmically with $\sqrt{s_{NN}}$. The solid line is the EKRT model prediction for central Au+Au collisions. It is seen that the EKRT

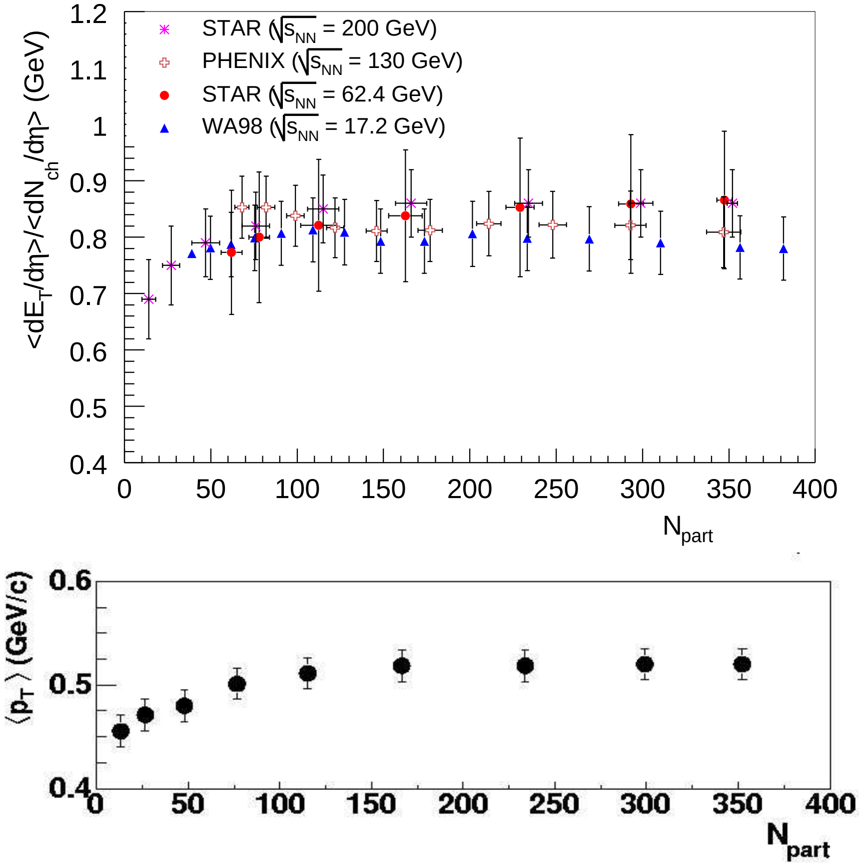

Figure 3.10: $< dE_T/d\eta > / < dN_{ch}/d\eta >$ Vs N_{part} (top). Results from WA98 [16] and PHENIX [17] are shown with STAR measurements. The mean transverse momentum of charged hadrons as a function of N_{part} [10] (bottom).

model underestimates the final transverse energy by $\sim$ 24% for 200 GeV Au+Au collisions and $\sim$ 64% for 62.4 GeV Au+Au collisions.

3.4.4 Variation of $< dE_T/d\eta >$ / $< dN_{ch}/d\eta >$ with Collision Centrality

In order to understand the systematic growth in transverse energy with collision energy shown in Fig. 3.9, the centrality dependence of $< dE_T/d\eta >$ / $< dN_{ch}/d\eta >$ i.e. the scaling of transverse energy relative to the number of charged particles produced in the collision is studied. The centrality dependence of the ratio may indicate the effects of hydrodynamic flow [9]. In this scenario if we assume the expansion of the produced fireball is isentropic (entropy is conserved), then $< dN_{ch}/d\eta >$ will remain constant while $< dE_T/d\eta >$ will decrease due to performance of longitudinal work. This is clearly reflected in the peripheral events as a dip (see Fig. 3.10) where we do expect hydrodynamic flow.

Fig 3.10 (top) shows the centrality dependence of $< dE_T/d\eta >$ / $< dN_{ch}/d\eta >$ from STAR measurements at $\sqrt{s_{NN}}$ = 200 GeV and 62.4 GeV, compared to similar measurements at 17.3 and 130 GeV. For the top 5% central Au+Au collisions at $\sqrt{s_{NN}}$ = 62.4 GeV, the value of $< dE_T/d\eta >$ / $< dN_{ch}/d\eta >$ is found to be 0.866 ± 0.122 GeV. The measured values for different centralities in Au+Au collisions at $\sqrt{s_{NN}}$ = 62.4 GeV are given in Table- 3.5.

Data at all energies starting from lower SPS to RHIC, within uncertainties, are seen to fall on a common curve. It shows a modest increase from the most peripheral collisions at $N_{part} < 50$, reaching a roughly constant value of the ratio at $N_{part} = 100$. Fig 3.10 (bottom) shows the $< p_T >$ for 200 GeV Au+Au collisions measured by STAR [10]. This shows a similar centrality dependence as that of the transverse energy per charge particle: modest increase with N_{part} for $N_{part} < 100$, with constant value for more central collisions. E_T, multiplicity and $< p_T >$ all show a similar behavior. This indicates that the increase of E_T is due to increased particle production. However, the quantitative comparison of theoretical models of particle production with the measured centrality dependences of $< dE_T/d\eta >$ / $< dN_{ch}/d\eta >$

and $< p_T >$ of charged particles will constrain the profile of initial energy deposition and the role of hydrodynamic work during the expansion.

3.4.5 The Global Barometric Observable: E_T/N_{ch}

Average transverse energy per charge particle is an important global barometric measure of the internal pressure in the ultra-dense matter produced in heavy ion collisions. Fig. 3.10 and Fig. 3.11 show the most amazing fact that a constant transverse energy per charge particle $(E_T/N_{ch}) \sim 800$ MeV has been produced which is almost independent of collision centrality and the collision energy. There is a slow logarithmic increase in E_T/N_{ch} amounting to $< 10\%$, which characterizes all the measurements within errors, over a range in which E_T per participant grows by a factor of 4. This has been observed from lower energy AGS measurements to the highest RHIC energies. This is shown in Ref. [19]. HIJING predicts that E_T per charged particle should increase from 0.8 (SPS) to 0.9 (RHIC) due to the enhanced mini-jet activity at RHIC. The EKRT initial state gluon saturation model predicts a growth of this quantity in

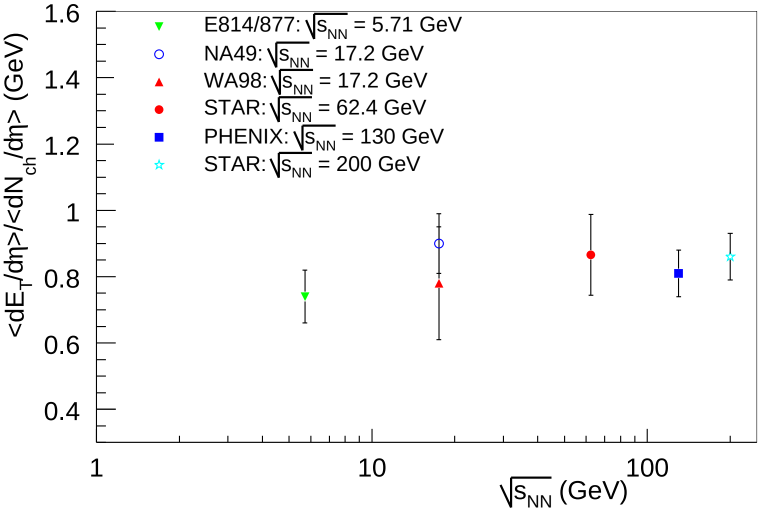

Figure 3.11: $< dE_T/d\eta >$ / $< dN_{ch}/d\eta >$ Vs $\sqrt{s_{NN}}$ for central events.

the initial state by about a factor of 3. The reason that EKRT model remains viable after these data is that the assumed entropy conservation implies that a large amount of pdV work due to longitudinal expansion is performed by the plasma. In 1+1D hydrodynamics the energy per particle, ϵ/ρ ($\approx 2.7\ T$) decrease as the system expands and cools ($T \sim 1/\tau^{1/3}$). If the freeze-out is assumed to occur at all energies and impact parameters in A+A collisions, on a fixed decoupling isotherm, then the energy per particle will always be the same.

However, there are theoretical problems in justifying hydrodynamics and the freeze-out prescription. The observed NULL effect in E_T/N_{ch} is very interesting because it is so difficult to obtain in any transport theory with finite pQCD relaxation rates [18].

3.4.6 Estimation of Energy Density

The estimation of initial energy density of the produced fireball in heavy ion collisions has been discussed in details in Chapter 1. This has been estimated in a boost invariant Bjorken hydrodynamic model. The Bjorken energy density obtained in this framework is given by

$$\epsilon_{Bj} = \frac{dE_T}{dy}\,\frac{1}{\tau_0 \pi R^2} \ \simeq\ < m_T > \frac{3}{2}\frac{dN_{ch}}{dy}\,\frac{1}{\tau_0 \pi R^2} \tag{3.15}$$

where, τ_0 is the formation time, usually assumed to be 1 fm/c and πR^2 is the transverse overlap area of the colliding nuclei. The formation time is usually estimated from model calculations and has been a matter of debate. There are different ways to estimate the transverse overlap area. It goes like $N_{part}^{2/3}$, in an approach which accounts for only the common area of colliding nucleons but not the nuclei (chosen by STAR). In this approach, the transverse overlap area $F = \pi R^2$, where $R = R_0 A^{1/3}$. When we replace A with the number of participants by, $A = N_{part}/2$ [11], F becomes,

$$F = \pi R_0^2\ (\frac{N_{part}}{2})^{2/3} \tag{3.16}$$

In the other approach (adopted by PHENIX) [19], the transverse overlap area of the

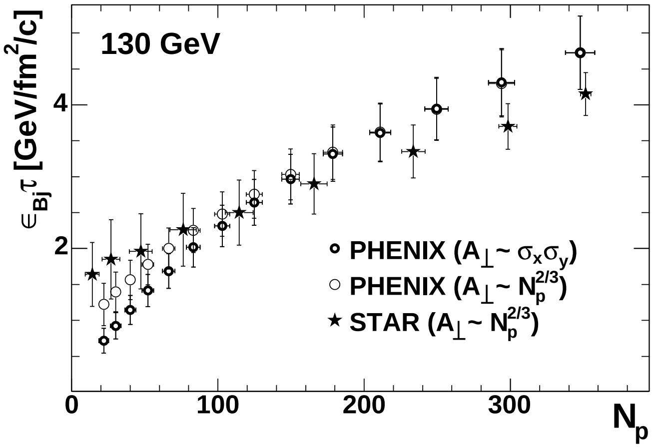

Figure 3.12: The Bjorken energy density vs N_{part} using different estimates of the transverse overlap area at $\sqrt{s_{NN}} = 130$ GeV. Ref. [19].

colliding species, F, is estimated in the following way. The Woods-Saxon parametrization for the nuclear density profile is given by

$$\rho(r) = \frac{1}{(1 + e^{(r-r_n)/d})}, \tag{3.17}$$

where, $\rho(r)$ is the nuclear density profile, r_n is the nuclear radius and d is a diffuseness parameter. Based on the measurements of electron scattering from Au nuclei [21], r_n is set to (6.38 ± 0.27) fm and d to (0.54 ± 0.01) fm. A Monte Carlo-Glauber model with $F \sim \sigma_x\sigma_y$, (where σ_x and σ_y are the widths of x and y position distributions of the participating nucleons in the transverse plane) is used to estimate the transverse overlap area of two colliding nuclei. In this approach, F is the transverse overlap area of two colliding nuclei not the participating nucleons. The normalization to πR^2, where R is the sum of r_n and d parameters in the Woods-Saxon parametrization (given by Eqn. 3.17), is done for most central collisions at the impact parameter $b = 0$.

The results obtained in these two methods, as shown in Fig. 3.12, are different only in the peripheral bins. The results obtained by STAR agree with PHENIX results, within systematic errors. However, STAR data show a a smaller rate of increase of

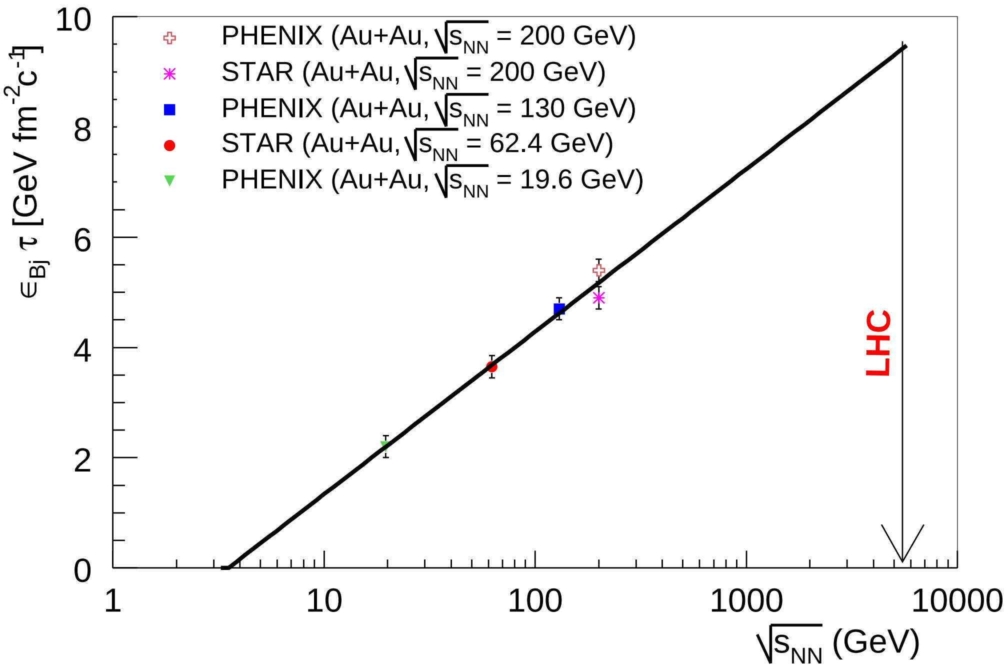

Figure 3.13: The excitation function of $\epsilon_{Bj}\tau$ $[GeV\ fm^{-2}\ c^{-1}]$. A prediction for LHC is indicated by an arrow, on the assumption of the validity of Bjorken hydrodynamic scenario.

the energy density with N_p. As can be seen from the figure, the results agree rather well for central collisions, where we expect a deconfinement of quarks and gluons to take place.

Using the procedure outlined above (for STAR), the ϵ_{Bj} for the 5% most central Au+Au collisions at $\sqrt{s_{NN}} = 62.4$ GeV is found to be 3.65 ± 0.39 GeV/fm^3. The estimated values of $\epsilon_{Bj}\tau$ for different centralities in Au+Au collisions at $\sqrt{s_{NN}} = 62.4$ GeV are given in Table- 3.6. In these estimations we have used a factor of 1.18 for $\eta \to y$-phase space conversion, as compared to 1.25 used by PHENIX [17, 19]. The value of ϵ_{Bj} for Au+Au collisions at $\sqrt{s_{NN}} = 19.6$, 130 [17, 19] and 200 GeV [2] are 2.2 ± 0.2, 4.7 ± 0.5 and 4.9 ± 0.3 GeV/fm^3 (5.4 ± 0.6 GeV/fm^3, PHENIX) respectively. Compared to this, ϵ_{Bj} at SPS for Pb+Pb collisions at $\sqrt{s_{NN}} = 17.2$ GeV is found to be 3.2 GeV/fm^3 [15]. This value of ϵ_{Bj} is much higher than the same for Au+Au collisions at the SPS-like energy i.e $\sqrt{s_{NN}} = 19.6$ GeV at RHIC. As all these estimations assume the same formation time of 1 fm/c, there is an over estimation of ϵ_{Bj} at SPS. In any case these energy densities are significantly larger than the energy density ($\sim$ 1 GeV/fm^3) predicted by lattice QCD calculations [20] for a transition to a deconfined quark gluon plasma phase. Following the deconfinement transition, there is a hydrodynamic expansion. Subsequently local equilibrium is achieved at $\tau_0 \sim 1$ fm/c. This picture is indeed valid, if we compare the RHIC data for elliptic flow to the hydrodynamic calculations [22, 23, 24]. Taking all ϵ_{Bj}s measured, for similar type of colliding species i.e. Au, at RHIC energies and assuming that the Bjorken hydrodynamic model works fine at energies higher than RHIC energy, we have made a prediction for the $\epsilon_{Bj}\tau$ for LHC. This is done using the Eqn. 3.15. This is shown in Fig. 3.13. The solid line is a logarithmic fit. The extrapolated value of $\epsilon_{Bj}\tau$ at LHC is 9.42 ± 0.55 $GeV\ fm^{-2}\ c^{-1}$. However, as the formation time at LHC will be much less than 1 GeV/fm^3, the above value sets a lower bound to the initial energy density to be formed at LHC.

Fig. 3.14 shows the estimate of the product of the Bjorken energy density and the formation time ($\epsilon_{Bj}.\tau$) as a function of the centrality of the collision in terms of N_{part}. The STAR estimation of $\epsilon_{Bj}.\tau$ at $\sqrt{s_{NN}} = 62.4$ GeV Au+Au collisions for different centrality classes, has been compared with similar data from PHENIX

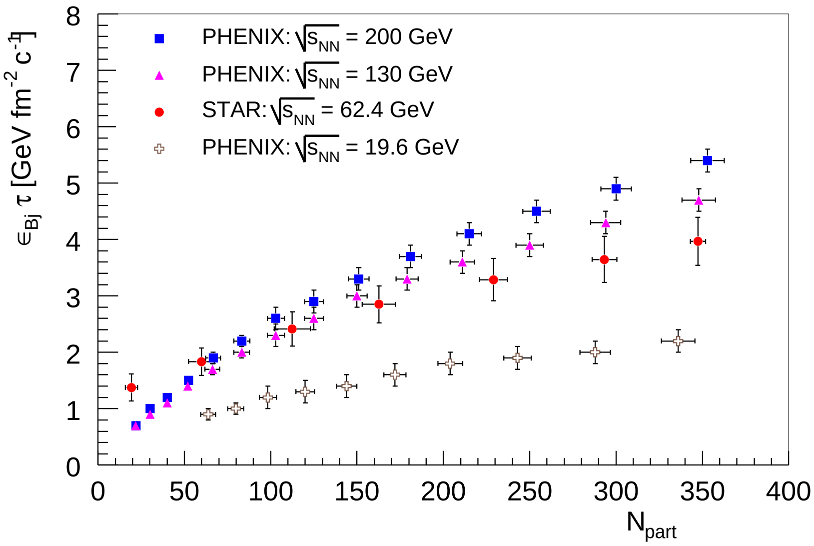

Figure 3.14: The N_{part} dependence of the product of the Bjorken energy density and the formation time ($\epsilon_{Bj}.\tau$) for Au+Au system at different energies at RHIC.

experiment, for similar collision species at different energies. As expected there is an increase in $\epsilon_{Bj}.\tau$ with increasing centrality of the collision. The STAR data for $\epsilon_{Bj}.\tau$ for Au+Au collisions at $\sqrt{s_{NN}}$ = 62.4 GeV show a cross over with PHENIX data for the peripheral collisions. This is because of different ways of estimation of the transverse overlap area by STAR and PHENIX (as explained earlier, see Fig. 3.12).

While comparing the results from different experiments, related to the initial energy density, one need to take care of the following factors: (i) value of the formation time taken into the calculations, (ii) the procedure of estimation of the transverse overlap area and (iii) the value of the Jaccobian used to transform η to y phase space.

3.4.7 Variation of $dE_T/d\eta$ and $dN_{ch}/d\eta$ per N_{part} pair with $\sqrt{s_{NN}}$

To study the variation of $dE_T/d\eta$ and $dN_{ch}/d\eta$ per N_{part} pair with center of mass energy we have taken the most central collisions data form different experiments at

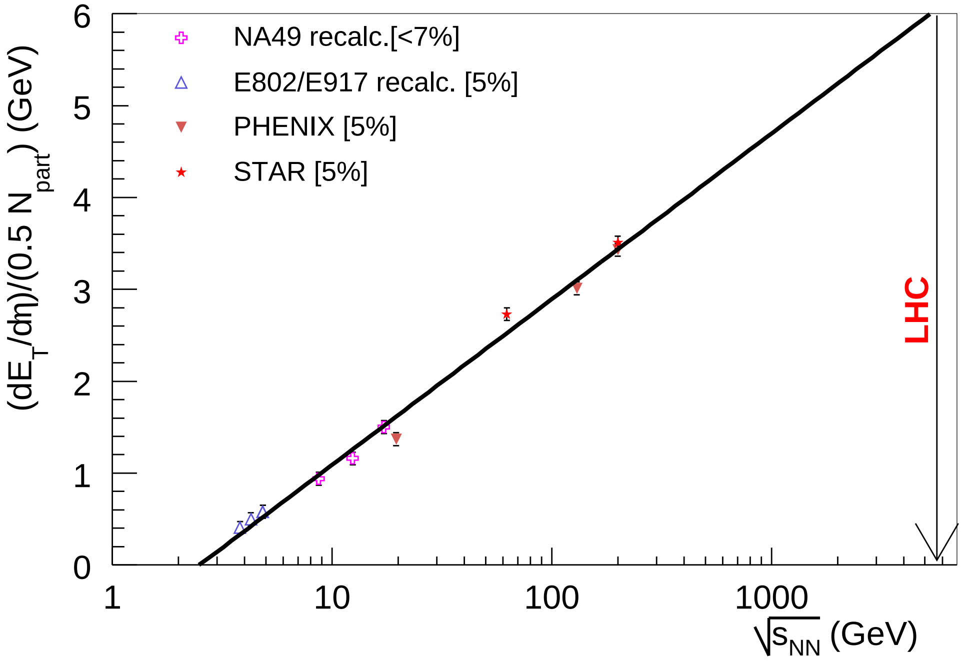

Figure 3.15: $dE_T/d\eta$ per participant pairs measured in most central collisions (value given in brackets) as a function of incident nucleon energy. The line is a logarithmic fit.

AGS [25, 26, 27, 28], SPS [15, 29, 30, 31] and RHIC [2, 17, 19].This is shown in Fig. 3.15 for E_T and in Fig. 3.16 N_{ch}. The values of $dE_T/d\eta$ and $dN_{ch}/d\eta$ per participant pair for the top 5% central Au+Au collisions at $\sqrt{s_{NN}} = 62.4$ GeV are found to be 2.73 ± 0.29 and 3.15 ± 0.29 respectively. We have tried to fit a phenomenological logarithmic function to both the figures motivated by the trend of the data in the range of available measurements. The fitted function is

$$(dX/d\eta)/(0.5\ N_{part}) = A\ ln(\sqrt{s_{NN}}/\sqrt{s^0_{NN}}), \tag{3.18}$$

where $X = E_T$ or N_{ch}. One can see the agreement of the fits in both the figures is very good. The results of the fits are:
for E_T, $\sqrt{s^0_{NN}} = 2.49 \pm 0.12$ GeV and $A = 0.78 \pm 0.014$ GeV,
for N_{ch}, $\sqrt{s^0_{NN}} = 1.60 \pm 0.38$ GeV and $A = 0.80 \pm 0.05$,

The parameter $\sqrt{s^0_{NN}} = 2.49$ obtained from the E_T fit is slightly greater than the minimum possible value of the center of mass energy i.e. $\sqrt{s^{min}_{NN}} = 2\ amu$ (1.86) GeV. The FOPI experiment [32, 33, 34] has carried out a measurement of $dE_T/d\eta$ at $\sqrt{s_{NN}} = 2.05$ which is close to $\sqrt{s^0_{NN}} = 2.49$. For most central collisions corresponding to $N_{part} = 359$, it has got $dE_T/d\eta = 5.0$ GeV [19]. The extrapolation of the fit to the lower energy suggests that the logarithmic parametrization requires higher order terms to describe how the E_T production starts at very low $\sqrt{s_{NN}}$. This is because, at very lower energies, this logarithmic parametrization gives a value of $(dE_T/d\eta)/(0.5\ N_{part})$ which is negative. But energy conservation demands that this value must approach zero smoothly at very low center of mass energies. An estimation of the value of $dE_T/d\eta$ per participant pair at the LHC energy is found to be around 6.03 ± 0.11 GeV, based on the extrapolation of the fit. From top SPS energy ($\sqrt{s_{NN}} = 17.2$ GeV) to the RHIC top energy ($\sqrt{s_{NN}} = 200$ GeV), there is an 131% increase in $dE_T/d\eta$ per participant pair. Whereas, there is an increase of 73% in $dE_T/d\eta$ per participant pair from RHIC top energy to LHC energy ($\sqrt{s_{NN}}$ = 5.5 TeV). Fig. 3.16 shows the earlier mentioned logarithmic fit to $dN_{ch}/d\eta$ per participant pairs for $N_{part} = 350$. Unlike for E_T, the fit parameter $\sqrt{s^0_{NN}}$ for N_{ch} is 1.60 ± 0.38 GeV. This is lower than the minimum center of mass energy as given

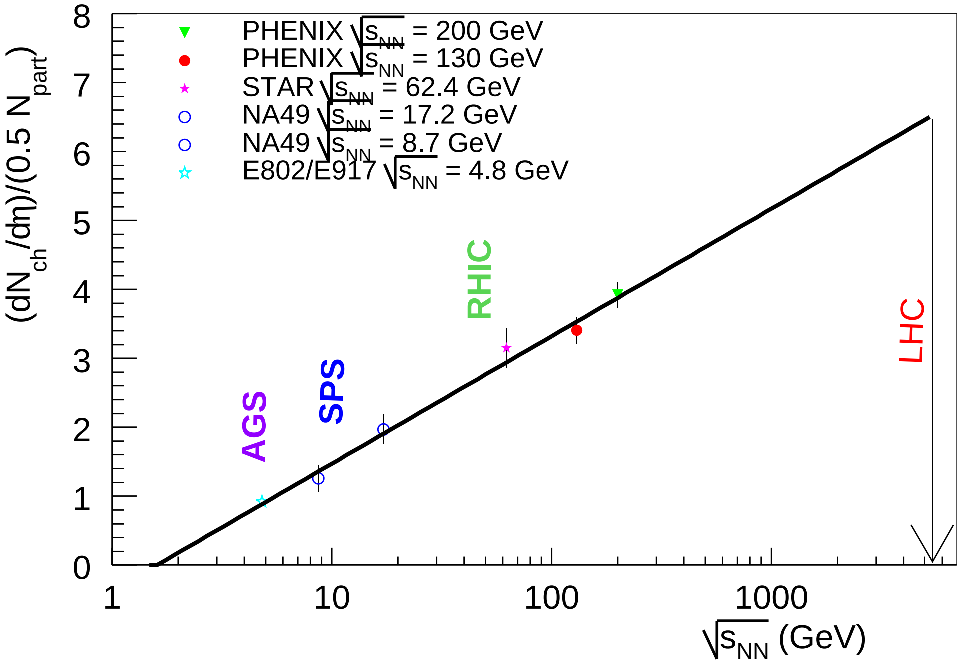

Figure 3.16: $dN_{ch}/d\eta$ per participant pairs measured in most central collisions as a function of incident nucleon energy. The line is a logarithmic fit. A prediction to LHC energy is shown by an arrow.

by $\sqrt{s_{NN}^{min}} = 1.86$ GeV. It suggests that above 2 *amu*, the N_{ch} production as a function of center of mass energy should undergo a threshold-like behavior, unlike the E_T production, which must approach zero smoothly because of energy conservation.

However, the FOPI measurements at $\sqrt{s_{NN}} = 1.94$ and 2.05 GeV agree with the extrapolation of the fit to lower $\sqrt{s_{NN}}$ close to 2 *amu*. It is an interesting result that colliding nuclei with kinetic energies of 0.037 and 0.095 GeV per nucleon in center of mass follow the same particle production trend, as is seen at AGS, SPS and RHIC energies.

The $dN_{ch}/d\eta$ per participant pairs for the most central events, shows about 11.4% increase from the highest AGS energy ($\sqrt{s_{NN}} = 4.8$ GeV) to the top SPS energy. From the highest SPS energy to the highest RHIC energy, there is a 100% increase in $dN_{ch}/d\eta/(0.5\ N_{part})$. Assuming that the same logarithmic behavior extends to the LHC energy, the predicted value of $dN_{ch}/d\eta = (6.53 \pm 0.45) \times (0.5 N_{part})$. This suggests that the increase in charge particle production from the highest RHIC energy to LHC, will be $\sim$ 65% for the most central events. PHENIX [19] explains the above

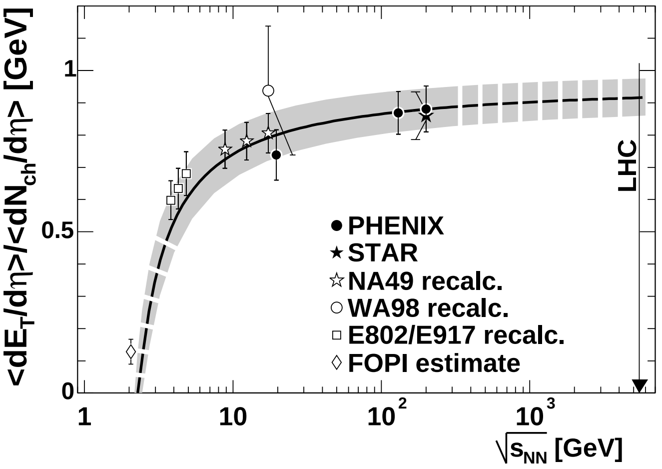

Figure 3.17: The ratio of E_T over N_{ch} for the most central events as a function of $\sqrt{s_{NN}}$. The line is the ratio of two fits shown in Fig. 3.15 and Fig. 3.16. The band corresponds to one standard deviation of the combined error.

behavior of E_T and N_{ch} in the following way. In Fig. 3.17 we have shown the E_T/N_{ch}

ratio for the most central collisions as a function of $\sqrt{s_{NN}}$. The solid line shown in the figure is the ratio of the fits used in Fig. 3.15 (for E_T) and Fig. 3.16 (for N_{ch}). This calculation agrees with the data very well. One can see there are two regions in the figure which could be clearly separated. The region from the lowest allowed energy to SPS energy is characterized by a steep increase of the E_T/N_{ch} ratio with $\sqrt{s_{NN}}$. In this region, the increase in the incident energy causes an increase in the $< m_T >$ of the produced particles [29, 35]. The second region starts from the SPS energies and continues above. In this region, E_T/N_{ch} is very weakly dependent on $\sqrt{s_{NN}}$. The incident energy goes for particle production, rather increasing the energy per particle.

The shape of the E_T/N_{ch} curve in the first region is governed by the difference in the $\sqrt{s^0_{NN}}$ parameter between E_T and N_{ch}. However, in the second region it is dominated by the ratio of the A parameters in the fits, which is close to 1 GeV. The extrapolation of the curve to LHC energy gives a value of E_T/N_{ch} equal to (0.92 ± 0.06) GeV.

3.4.8 The Electromagnetic Component of Total Transverse energy

The electromagnetic fraction of total transverse energy (E^{em}_T/E_T) has contributions predominantly from photons emitted at all stages of evolution of the fireball. This is because, the production cross-section for electrons and positrons, which come in electromagnetic sector, is very less. Hence, this ratio can roughly give information on the integrated photon energy produced in the collision process. As photons are emitted at all stages of the fireball evolution, we have direct photons coming from the plasma and also thermal or decayed photons (from electromagnetic and weak decays) coming at later stages. The main sources of decayed photon are π^0, ω^0 and ρ. In the hadronic sector the production cross-section of pions is the highest. If we assume all the isospin partners of pions are equally probable to be produced in the collision, then the decay of each neutral pion into two photons would result in an E^{em}_T/E_T ratio of 0.33. If we take other decay sources of photons, then this number should be slightly

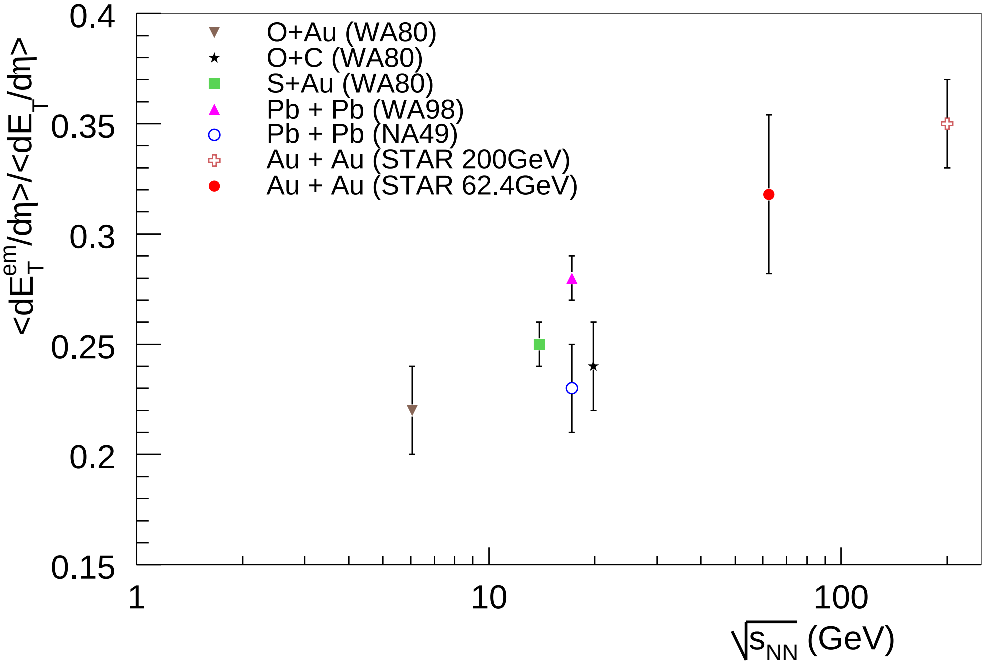

Figure 3.18: The center of mass energy dependence of electromagnetic fraction of total transverse energy for a number of systems from SPS to RHIC energy for central events.

larger than 0.33. For a long-lived plasma we would expect a very high photon yield [38]. Hence, if we observe an increase in this ratio significantly higher than this value, then we can say something on the formation of a long-lived deconfined plasma phase. In addition, the electromagnetic fraction of total energy will strongly be influenced by the meson to baryon ratio. This is because, the main sources of photons are mesons. At lower energies due to nuclear stopping, the baryon content in the produced matter will be very high. At very large energies where the system is almost baryon free, we would expect virtually all the E_T to be carried by mesons. Hence the electromagnetic fraction of total energy should increase with center of mass energy.

Taking top 5% central events, we have estimated the electromagnetic fraction of the total transverse energy for 62.4 GeV Au+Au collisions. This result is shown in Fig. 3.18, as a function of the center of mass energy, along with similar data from other measurements ranging from lower SPS energies [36, 37] to the top RHIC energy. The values of $< dE_T^{em}/d\eta > / < dE_T/d\eta >$ ratio are 0.35 ± 0.02 and 0.318 ± 0.03, for $\sqrt{s_{NN}} = 200$ GeV and 62.4 GeV respectively. The estimated values of $< dE_T^{em}/d\eta > / < dE_T/d\eta >$ for different centralities in Au+Au collisions at $\sqrt{s_{NN}} = 62.4$ GeV are given in Table- 3.6. At SPS, for Pb+Pb collisions at $\sqrt{s_{NN}} = 17.2$ GeV, this ratio has a value of 0.23 ± 0.02 [15]. There is a 52% increase of the electromagnetic fraction of total energy from SPS to RHIC top energy. However, from the values of these ratios, observed at RHIC energies, it is not conclusive to say anything about the formation of a long-lived deconfined phase of quarks and gluons. The energy dependence seen in Fig. 3.18 is presumably dominated by the total meson content of the final state. The centrality dependence of this ratio may provide additional information about the reaction mechanisms. This is shown in Fig. 3.19 for the Au+Au collisions at $\sqrt{s_{NN}} = 62.4$ GeV and 200 GeV. However, no significant centrality dependence of the electromagnetic fraction has been observed. This is similar to what has been found in Au+Au collisions at $\sqrt{s_{NN}} = 200$ GeV [2].

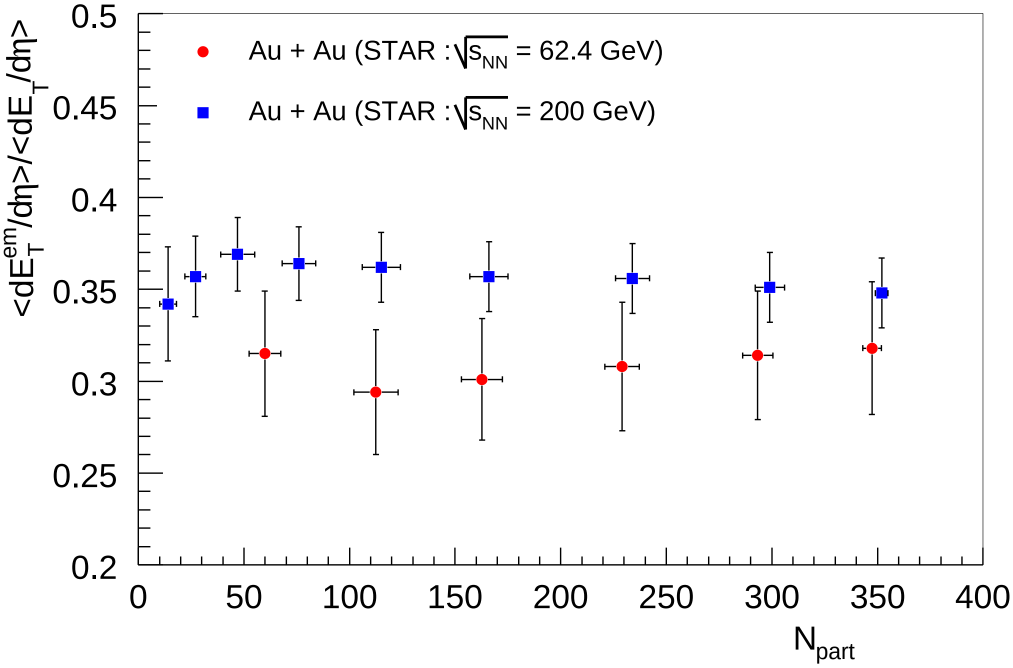

Figure 3.19: The centrality dependence of electromagnetic fraction of total transverse energy.

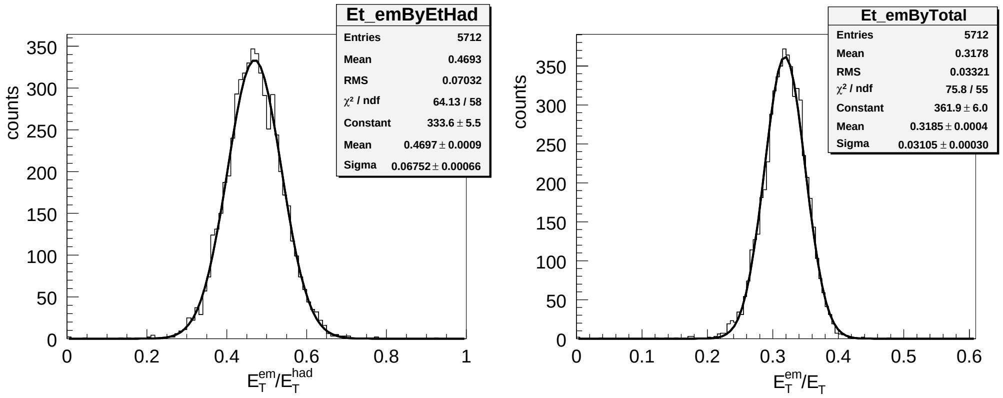

Figure 3.20: Event-by-event distributions of a) E_T^{em}/E_T^{had} and b) E_T^{em}/E_T for the top 5% central events in $\sqrt{s_{NN}}$ = 62.4 GeV Au+Au collisions. A gaussian function is fitted to the distributions.

3.4.9 The Ratios of E_T^{had} and E_T^{em}

Taking top 5% central events in 62.4 GeV Au+Au collisions, we have plotted the ratio of E_T^{em} to E_T^{had} and the ratio of E_T^{em} to E_T in Fig. 3.20. The mean value of E_T^{em}/E_T^{had} and ofE_T^{em}/E_T are found to be 0.47 and 0.32 respectively. These have been obtained from gaussian fittings to the distributions. The gaussian behavior of these distributions indicate the possibility of carrying out fluctuation studies in these ratios. We have estimated the ratio of E_T^{em}/E_T^{had} for top 5% central events in $\sqrt{s_{NN}} = 62.4$ GeV Au+Au collisions. The value of this ratio is 0.47 ± 0.05. This ratio is shown in Fig. 3.21 as a function of center of mass energy, along with similar data from other measurements (NA49 at SPS, PHENIX and STAR at RHIC). This ratio is found to increase with center of mass energy.

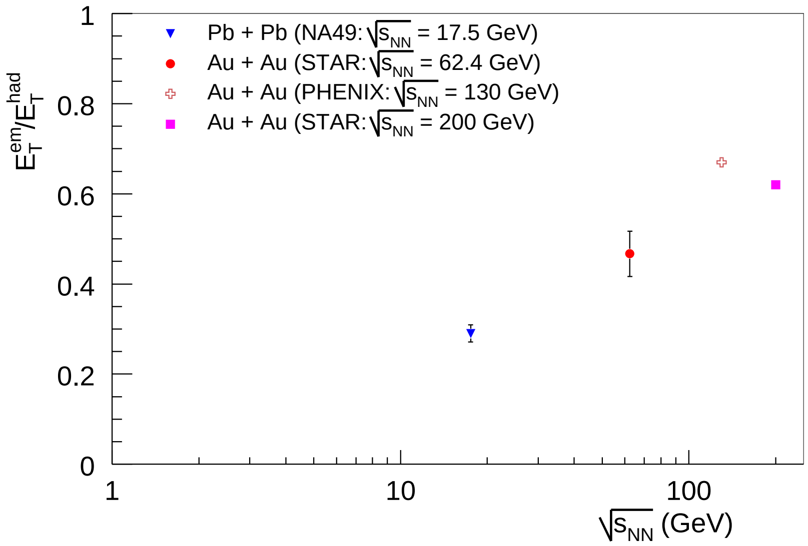

Figure 3.21: E_T^{em}/E_T^{had} is shown as a function of center of mass energy. Data points are from NA49 [15], PHENIX [17] and STAR [2]

Sources of Syst. Errors	E_T^{had}	N_{ch}	E_T^{em}
$\|V_z\| < 50\ cm$	-0.46 %	-0.62%	-
$\|dac\| < 4.5\ cm$	-0.26 %	-0.27%	-
$nFitPoints > 5$	+3.3 %	+3.3 %	-
$nFitPoints > 15$	-5.8 %	-6.6 %	-
correction factors	±8.5%	±6.4%	±2.2%
calibration	-	-	±2.%
Total	10.3%	9.1%	3.%

Table 3.4: The systematic uncertainties in percentage for top 5% central Au+Au collisions at $\sqrt{s_{NN}} = 62.4$ GeV.

3.5 Estimation of Systematic Uncertainties

There are various sources of systematic uncertainties in the estimation of both the components of E_T. We have divided these sources into two classes. One class consists of uncertainties in the estimation of various correction factors used in the measurement. This has been discussed previously in this chapter. The other class is having contributions from the dynamical cuts used in the analysis. The final systematic uncertainty is the quadratic sum of the contributions from both the classes. Here, we discuss the estimation procedure of the uncertainties coming from the dynamic cuts used. The dynamic cuts used in this analysis include a DCA cut ($|dca| < 3\ cm$) to select primary tracks, a cut on z-position of the vertex ($|V_z| < 30\ cm$) and the number of fit points cut on TPC tracks ($nFitPoints > 10$). For the estimation of E_T^{had} and the charge particle multiplicity (N_{ch}), we have varied the DCA-cut to $|dca| < 4.5\ cm$, the z-position of the vertex to $|V_z| < 50\ cm$ and the number of fit points cut to $nFitPoints > 5$ in one case and $nFitPoints > 15$ in another case. While varying individual cuts, we keep other baseline cuts unchanged and find out the percentage of variation in E_T^{had} and N_{ch}. For the estimation of final systematic uncertainties in E_T^{em}, we have taken the quadratic sum of the uncertainties due to correction factors and that due to the calibration procedure. The positive and negative errors are added up separately in quadrature rule. The larger of the two is the final systematic error.

Centrality (%)	N_{part}	E_T (GeV) $\pm 11\%$	E_T^{had} (GeV) $\pm 10.3\%$	E_T^{em} (GeV) $\pm 3\%$	E_T/N_{ch} (GeV) $\pm 14\%$
0-5	347.4 ± 4.4	474 ± 51	322 ± 33	151 ± 5	0.87 ± 0.12
5-10	293.3 ± 7.1	389 ± 43	267 ± 27	122 ± 3	0.86 ± 0.12
10-20	229.1 ± 8.2	297 ± 33	206 ± 21	92 ± 3	0.85 ± 0.12
20-30	162.7 ± 9.7	205 ± 22	143 ± 15	62 ± 2	0.84 ± 0.12
30-40	112.5 ± 10.5	136 ± 15	96 ± 10	40 ± 1	0.82 ± 0.12
40-60	59.9 ± 7.5	68 ± 7	49 ± 5	21.4 ± 0.6	0.80 ± 0.12
60-80	19.3 ± 3.5	24 ± 3	16 ± 2	11.2 ± 0.3	0.77 ± 0.11

Table 3.5: E_T, E_T^{had}, E_T^{em} and E_T/N_{ch} for different centralities in Au+Au collisions at $\sqrt{s_{NN}} = 62.4$ GeV. All uncertainties are systematic and statistical errors are negligible.

Table. 3.4 enlists the sources of systematic errors and their estimated values for E_T^{had}, E_T^{em} and N_{ch}. The uncertainty in E_T is the quadratic sum of the same estimated in E_T^{had} and E_T^{em}. We have estimated the systematic uncertainties in the top 5% central Au+Au collisions and have applied the same percentage to the systematic uncertainties in other centrality classes.

Taking the systematic uncertainties in E_T, E_T^{had}, E_T^{em} and N_{ch} we have estimated the uncertainties in various observables such as $E_T/(0.5N_{part})$, E_T^{em}/E_T, $\epsilon_{Bj}\tau$ etc., using the usual error propagation formula (see Appendix-1). The estimated values of these observables and the coresponding systematic errors are tabulated in Table. 3.5 and Table. 3.6. The method and formulae used to estimate the systematic uncertainties in different observables are given in Appendix-1.

Centrality (%)	N_{part}	$E_T/(0.5N_{part})$ (GeV) ±10.6%	E_T^{em}/E_T ±11.3%	$\epsilon_{Bj}\tau$ $(GeV fm^{-2}c^{-1})$ ±10.8%
0-5	347.4 ± 4.4	2.73 ± 0.29	0.318 ± 0.036	3.97 ± 0.43
5-10	293.3 ± 7.1	2.65 ± 0.3	0.314 ± 0.035	3.64 ± 0.41
10-20	229.1 ± 8.2	2.59 ± 0.3	0.308 ± 0.035	3.29 ± 0.37
20-30	162.7 ± 9.7	2.52 ± 0.3	0.301 ± 0.033	2.85 ± 0.32
30-40	112.5 ± 10.5	2.41 ± 0.34	0.294 ± 0.034	2.41 ± 0.30
40-60	59.9 ± 7.5	2.26 ± 0.36	0.315 ± 0.034	1.83 ± 0.24
60-80	19.3 ± 3.5	2.47 ± 0.54	0.468 ± 0.054	1.37 ± 0.24

Table 3.6: $E_T/(0.5N_{part})$, E_T^{em}/E_T and $\epsilon_{Bj}\tau$ for different centrality classes in Au+Au collision at $\sqrt{s_{NN}} = 62.4$ GeV. All uncertainties are systematic and statistical errors are negligible.

Bibliography

[1] M. Jacob and P.V. Landshoff, *Mod. Phys. Lett.* **A1** (1986) 657; X.N. Wang, *Phys. Rep.***280** (1997) 287.

[2] J. Adams *et al.*, STAR Collaboration, *Phys. Rev.* **C 70** (2004) 054907.

[3] T. Akesson *et al.*, HELIOS Collaboration, *Z. Phys.* **C38** (1988) 383.

[4] J. Adams *et al.*, STAR Collaboration, Long *Phys. Rev.* **C** under preparation.

[5] J. Adams *et al.*, STAR Collaboration, *Phys. Lett.* **B637** (2006) 161.

[6] X.N. Wang and M. Gyulassy, *Phys. Rev.* **D 44** (1991) 3501.

[7] T. Abbott *et al.*, *Phys. Rev.* **C 63** (2001) 064602.

[8] T. Cormier *et al.*, *Nucl. Instr. and Meth. Phys.* **A 483** (2002) 734.

[9] P.F. Kolb *et al.*, *Nucl. Phys.* **A696** (2001) 197.

[10] J. Adams *et al.*, STAR Collaboration, *Phys. Rev. Lett.* **91** (2003) 172302.

[11] D. Kharzeev and M. Nardi, *Phys. Lett.* **B507** (2001) 121.

[12] David d'Enterria, nucl-ex/0608049.

[13] K.J. Eskola *et al.*, *Nucl. Phys.* **B570** (2000) 379.

[14] J. Barrettee *et al.*, *Phys. Rev. Lett.* **70** (1993) 2996.

[15] T. Alber *et al.*, *Phys. Rev. Lett.* **75** (1995) 3814.

[16] M.M. Aggarwal *et al.*, WA98 Collaboration, *Eur. Phys. J.* **C18** (2001) 651.

[17] K. Adcox *et al.*, PHENIX Collaboration, *Phys. Rev. Lett.* **87** (2001) 052301.

[18] M. Gyulassy, *Lecture Notes in Physics* **583** (2001) 37.

[19] S.S. Adler *et al.*, PHENIX Collaboration, *Phys. Rev.* **C 71** (2005) 034908.

[20] F. Karsch, *Nucl. Phys.* **A698** (2002) 199c.

[21] B. Hahn *et al.*, *Phys. Rep.***101** (1956) 1131; C.W. De Jager *et al.*, At. Data Nucl. Data Tables **24** (1974) 479;

[22] T.S. Ullrich, *Nucl. Phys.* **A715** (2003) 399c.

[23] J. Adams *et al.*, STAR Collaboration, *Phys. Rev. Lett.* **92** (2004) 052302.

[24] P.F. Kolb and U. Heinz, nucl-th/0305084 (2003).

[25] L. Ahle *et al.*, E802 Collaboration, *Phys. Rev.* **C 59** (1999) 2173.

[26] L. Ahle *et al.*, E802 Collaboration, *Phys. Rev.* **C 58** (1998) 3523.

[27] B.B. Back *et al.*, E917 Collaboration, *Phys. Rev. Lett.* **86** (2001) 1970.

[28] L. Ahle *et al.*, E802 Collaboration, *Phys. Rev.* **C 57** (1998) 466(R).

[29] J. Bachler *et al.*, NA49 Collaboration, *Nucl. Phys.* **A661** (1999) 45.

[30] S.V. Afanasiev *et al.*, NA49 Collaboration, *Phys. Rev.* **C 66** (2002) 054902.

[31] M. van Leeuwen *et al.*, NA49 Collaboration, *Nucl. Phys.* **A715** (2003) 161.

[32] W. Reisdorf *et al.*, FOPI Collaboration, *Nucl. Phys.* **A612** (1997) 493.

[33] W. Reisdorf *et al.*, FOPI Collaboration, *Z. Phys.* **A357** (1997) 215.

[34] B. Hong *et al.*, FOPI Collaboration, *Phys. Rev.* **C 66** (2002) 034901.

[35] S.S. Adler *et al.*, PHENIX Collaboration, *Phys. Rev.* **C 69** (2004) 034909.

[36] R. Albrecht *et al.*, WA80 Collaboration, *Phys. Rev.* **C 44** (1991) 2736.

[37] WA98 Collaboration, Systematics of Transverse Energy Production in Pb+Pb Collisions at 158 GeV/nucleon (1996).

[38] F. Halzen and H.C. Liu, *Phys. Rev.* **D 25** (1982) 1842.

Chapter 4

Transverse Energy Fluctuations

4.1 Introduction

Fluctuations in physical observables in heavy ion collisions have been a topic of interest since decades. They provide important signals regarding the formation of QGP and also help to address important questions related to thermalization [1]. The study of fluctuations on an event-by-event basis has become a reality with the advent of modern accelerators where a large number of particles are produced in heavy ion collisions. There have been several new methods for the study of event-by-event fluctuations in global observables to probe the nature of the QCD phase transition [2, 3, 4, 5, 6]. In a thermodynamic picture of a strongly interacting system produced in the collision, the fluctuations in particle multiplicities, mean transverse momentum ($< p_T >$), transverse energy (E_T), net charge and other global observables, are related to the fundamental properties of the system, such as the chemical potential, specific heat and the matter compressibility. These help in the understanding of the critical fluctuations near the QCD phase boundary. The existence of a tricritical point at the QCD phase boundary, has been predicted to be associated with large event-by-event fluctuations in the above observables [2].

It is believed that in the first order phase transition scenario, the supercooling might lead to density fluctuations which result in droplet and hot spot formations [7]. These might lead to fluctuations in rapidity in the form of spikes and gaps.

The event-by-event fluctuations of the number of photons to charged particles has been proposed to be a probe for the formation of the disoriented chiral condensates (DCC) [8, 9]. The study of fluctuations in particle ratios, e.g. $K/\pi, \pi^+/\pi^-, \pi^0/\pi^\pm$ etc. are interesting, as many systematic errors get nullified. There are also theoretical predictions on strangeness fluctuations [10].

E_T is an extensive global variable which provides a direct measure of the violence of an interaction. It is also an indicator of the energy density produced in the collision. Since energy density is directly associated with the quark-hadron phase transition, it is extremely important to study E_T and fluctuations in E_T. In addition, it is interesting to compare the fluctuations in E_T to that observed in the particle multiplicities. This is because, E_T has a very good correlation with the charge particle multiplicity and the center of mass energy. In addition, E_T fluctuation has been predicted to be leading to J/Ψ suppression [11]. It is also interesting to study the fluctuations in both the components of E_T, as we have an independent event-by-event measurement of both the electromagnetic and hadronic components of transverse energy.

There have been a lot of interest to study event-by-event fluctuations which is motivated by the experimental observation of near perfect Gaussian distributions of $< p_T >$, particle multiplicity and particle ratios at various centralities [12, 13]. The variance or width of these Gaussian distributions contain information about the reaction mechanism as well as the nuclear geometry [2, 14, 15, 16].

4.2 Fluctuation Measures

There are various different methods used to quantify fluctuations in different observables. This also helps in comparing the measurements carried out by different experiments which use different methods for fluctuation studies.

4.2.1 The Variance and the Φ Measure

The relative fluctuation (ω_A), in an observable A, could be expressed as

$$\omega_A = \frac{\sigma_A}{< A >} = \frac{(< A^2 > - < A >^2)^{1/2}}{< A >} \tag{4.1}$$

where, σ_A is the standard deviation of the distribution and $< A >$ is the mean value. The variance which we get from the experimental data has contributions both from the statistical and dynamical sources. One need to know the statistical and other sources of fluctuations in order to extract new physics from the observed dynamical fluctuations. The known sources of fluctuations contributing to the ω_A include, the finite particle multiplicity, impact parameter fluctuations in the real experiment, effect of limited detector acceptance, fluctuations in the number of primary collisions, resonance decays, Bose-Einstein correlations, fluctuations in the transverse flow velocity and the effects of re-scattering of the secondary particles [2]. $\frac{\sigma_A^2}{<A>}$ is also used as a measure of fluctaution [17].

To get rid of the statistical fluctuations in ω_A, it is calculated independently from data and from the baseline i.e. mixed event distributions. The difference in fluctuation from a random baseline is defined as

$$d = \omega_{(A,data)} \; - \; \omega_{(A,baseline)} \tag{4.2}$$

The sign of d is positive if the data distribution contains a correlation. The fraction of the fluctuations that deviate from the random baseline expectation is

$$F_A = \frac{\omega_{(A,data)} \; - \; \omega_{(A,baseline)}}{\omega_{(A,baseline)}} = \frac{\sigma_{(A,data)} \; - \; \sigma_{(A,baseline)}}{\sigma_{(A,baseline)}} \tag{4.3}$$

where $\sigma_{(A,data)}$ refers to the standard deviation of the event-by-event data distribution and $\sigma_{(A,baseline)}$ refers to the standard deviation of the mixed event distribution. The most commonly used quantity Φ [18] is given by

$$\Phi_A = [\sigma_{(A,data)} \; - \; \sigma_{(A,baseline)}]\sqrt{< N_A >} = d < A > \sqrt{< N_A >} \tag{4.4}$$

where N_A is the number of particles or tracks or clusters depending on specific cases. Φ_A is related to F_A by

$$\Phi_A = F_A \; \sigma_{(A,baseline)} \; \sqrt{< N_A >}. \tag{4.5}$$

All the above variables are used to quantify the fluctuations and they are all correlated through the above equations.

4.2.2 The ν_{dyn}

The variable ν_{dyn}, as a measure of fluctuations was first suggested in Ref.[6]. The basis of this variable is the single- and two-particle distribution functions. The ν_{dyn} used for the net-charge fluctuation is given by

$$\nu_{+-,dyn} = \frac{< N_+(N_+ - 1) >}{< N_+ >^2} + \frac{< N_-(N_- - 1) >}{< N_- >^2} - 2\frac{< N_+N_- >}{< N_+ >< N_- >} \tag{4.6}$$

This is based on two-particle correlation functions. The ν_{dyn} is very robust, as it is independent of the detector efficiency and acceptance.

4.2.3 The Balance Function

The balance function, as a technique to study the dynamics of hadronization in relativistic heavy ion collisions, was first proposed by Bass *et al.* [19]. The idea behind balance function is that the rapidity range of the correlations is changed when a collision forms QGP. To be specific, charged hadrons form late in the reaction, after hadronization, resulting in shorter-ranged correlations in rapidity space for charge/anti-charge pairs than expected in the absence of the plasma. The balance function is defined as

$$B(p_2|p_1) \equiv \frac{1}{2}[\rho(b, p_2|a, p_1) - \rho(b, p_2|b, p_1) + \rho(a, p_2|b, p_1) - \rho(a, p_2|a, p_1)], \tag{4.7}$$

where $\rho(b, p_2|a, p_1)$ is the conditional probability of observing a particle of type b in bin p_2 given the existence of a particle of type a in bin p_1. The conditional probability $\rho(b, p_2|a, p_1)$ is generated by first counting the number $N(b, p_2|a, p_1)$ of pairs that satisfy both criteria and then dividing by the number $N(a, p_1)$ of particles of type a that satisfy the first criteria.

$$\rho(b, p_2|a, p_1) = \frac{N(b, p_2|a, p_1)}{N(a, p_1)} \tag{4.8}$$

The balance function is also related to the ν_{dyn} [6].

4.3 The E_T Fluctuation

As discussed in Chapter 3, for all centrality classes, the E_T distributions are Gaussians. Hence, we can study fluctuations in E_T. Fig. 4.1 shows the E_T distribution for

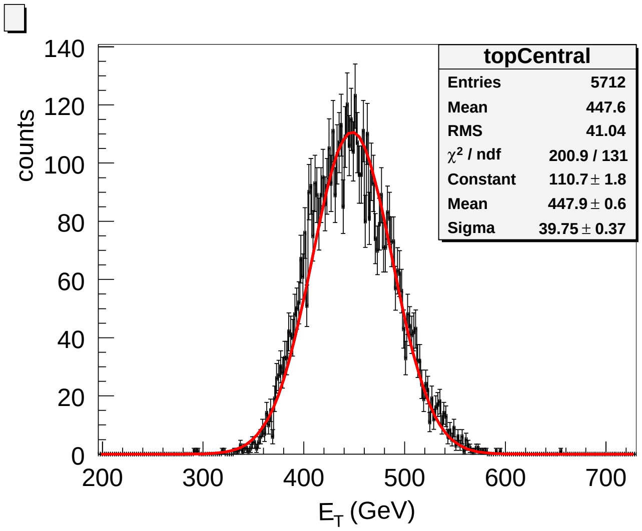

Figure 4.1: The E_T distribution for the top 5% central events for $\sqrt{s_{NN}} = 62.4$ GeV Au+Au collisions, is shown to fit to a Gaussian distribution function.

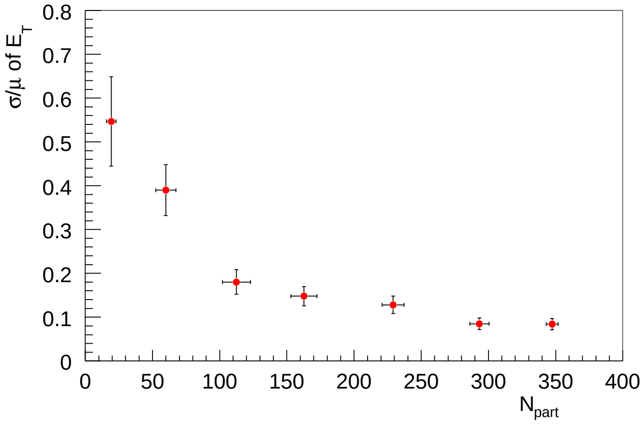

Figure 4.2: The σ/μ of E_T for $\sqrt{s_{NN}} = 62.4$ GeV Au+Au collisions is shown as a function of the centrality of the collision.

top 5% central events in $\sqrt{s_{NN}} = 62.4$ GeV Au+Au collisions. We have estimated the $\sigma/ < E_T >$ for all centrality classes. This is shown in Fig. 4.2 as a function of centrality. When we go from the central to peripheral collisions, the fluctuation in E_T increases. However, there is a necessity of taking narrower centrality bins and more efficient fluctuation variable to extract physics from dynamical fluctuations in E_T. For the top 5% central events in $\sqrt{s_{NN}} = 62.4$ GeV Au+Au collisions, the $\sigma/ < E_T >$ is found to be 8.4%.

For the top 5% central events, we have already shown the event-by-event distribution of E_T^{em}/E_T^{had} and E_T^{em}/E_T in Chapter 3. They fit very well to Gaussian functions. The fluctuations in these observables in terms of their σ/μ for top 5% central events in $\sqrt{s_{NN}} = 62.4$ GeV Au+Au collisions are 14.4% and 9.74% respectively.

Bibliography

[1] L. Van Hove, *Phys. Lett.* **B118** (1982) 138; H. Heiselberg, *Phys. Rep.*351 (2001) 161; E.V. Shuryak, *Phys. Lett.* **B423** (1998) 9; S. Mrowczynski, *Phys. Rev.* **C 57** (1998) 1518; *Phys. Lett.* **B430** (1998) 9; M. Gazdzicki and S. Mrowczynski, *Z. Phys.* **C57** (1992) 127.

[2] M. Stephanov *et al.*, *Phys. Rev. Lett.* **81** (1998) 4816; *Phys. Rev.* **D 60** (1999) 114028.

[3] G. Baym and H. Heiselberg, *Phys. Lett.* **B469** (1999) 7.

[4] M. Asakawa *et al.*, *Phys. Rev. Lett.* **85** (2000) 2072.

[5] S. Jeon and V. Koch, *Phys. Rev. Lett.* **83** (1999) 2076.

[6] C. Pruneau, *et al.*, *Phys. Rev.* **C 66** (2002) 044904.

[7] L. van Hove, *Z. Phys.* **C21** (1984) 93; J.I. Kapusta and A.P. Vischer, *Phys. Rev.* **C 52** (1995) 2725.

[8] M.M. Aggarwal *et al.*, WA98 Collaboration, *Phys. Rev.* **C 64** (2001) 011901(R).

[9] B.Mohanty and J. Serreau, *Phys. Rep.***414** (2005) 263-358 and the references therein.

[10] M.I. Gorenstein *et al.*, *Phys. Lett.* **B585** (2004) 237.

[11] J.P. Blaizot *et al.*, *Phys. Rev. Lett.* **85** (2000) 4012.

[12] H. Appelshauser *et al.*, NA49 Collaboration, *Phys. Lett.* **B459** (1999) 679; G. Roland, *Nucl. Phys.* **A638** (1998) 91c.

[13] K. Adcox *et al.*, PHENIX Collaboration, *Phys. Rev.* **C 66** (2002) 024901.

[14] G. Baym *et al.*, *Phys. Lett.* **B219** (1989) 205.

[15] R. Albrecht *et al.*, *Z. Phys.* **C45** (1989) 31.

[16] F. Corriveau *et al.*, NA34 Collaboration, *Z. Phys.* **C38** (1988) 15; J. Schukraft *et al.*, NA34 Collaboration, *Z. Phys.* **C38** (1988) 59.

[17] M.M. Aggarwal *et al.*, WA98 Collaboration, *Phys. Rev.* **C 65** (2002) 054912.

[18] M. Gazdzicki and S. Mrowczynski, *Z. Phys.* **C54** (1992) 127.

[19] S A. Bass *et al.*, *Phys. Rev. Lett.* **85** (2000) 2689.

Chapter 5

Summary and Conclusion

In thesis, we have reported results on the transverse energy measurement and fluctuation studies in Au+Au collisions at $\sqrt{s_{NN}} = 62.4$ GeV. This data set was taken by the STAR experiment at RHIC, BNL. We have used the STAR TPC and the BEMC detectors for this data analysis. In the common phase space of both the detectors ($0 < \eta < 1$ and full ϕ), we have obtained the hadronic transverse energy from the TPC reconstructed tracks and the electromagnetic transverse energy from the BEMC tower hits after correcting for the hadronic contaminations in the calorimeter. This method provides an independent measurement of both the components of transverse energy on an event-by-event basis. The measurement of E_T is very important as it helps in the estimation of the initial energy density of the produced fireball. The initial energy density tells about the QCD phase transition which is related to the formation of QGP. The centrality dependence of E_T production is crucial in understanding the particle production mechanism. The fluctuations in E_T can provide important information related to the QCD phase transition.

With the above motivations, we have measured the E_T from both of it's components and have made a detailed study with center of mass energy and centrality of the collisions. For the top 5% central collisions we have obtained $< E_T >_{5\%} = 474 \pm 51$ $(syst)$ ± 1 $(stat)$ GeV. We have also investigated the scaling of transverse energy with the number of participating nucleons and with the number of charged particles produced in the collision. For the 5% most central collisions we have obtained, $<$

$dE_T/d\eta > /(0.5N_{part}) = 2.73\pm0.29$ GeV and $< dE_T/d\eta > / < dN_{ch}/d\eta >= 866\pm122$ MeV respectively. The most striking feature is the observation of a nearly constant value of $< dE_T/d\eta > / < dN_{ch}/d\eta >$ from AGS, SPS to RHIC. This also shows a very weak centrality dependence. It is found that the increase in E_T production from lower AGS to higher RHIC energies comes mostly from the increase in particle multiplicity. A final state gluon saturation model (EKRT) is compared with the data. A different centrality behavior has been predicted by this model. However, the uncertainty in the N_{part} estimation rules out discarding this model. $< dE_T/dy > /(0.5N_{part})$ is seen to increase logarithmically with center of mass energy: from AGS, SPS to RHIC.

Theoretical calculations along with the measurements at RHIC suggest that a dense and equilibrated system has been formed in the collision. The expansion of the system also respects the hydrodynamics of an ideal fluid. There is a very good agreement between the hydrodynamic calculations and the results from identified spectra and elliptic flow [1], on the onset of hydrodynamic evolution at a time $\tau_0 < 1$ fm/c after the collision [2]. In addition, the suppression phenomenon for high-p_T hadrons observed at RHIC [3], suggests that the system at it's early times is very dense. Based on the boost-invariant Bjorken hydrodynamic model, the estimation of the initial density of the produced system is about $3.65 \pm 0.39\ GeV/fm^3$. This has been calculated from the measured E_T for the top central collisions at $\sqrt{s_{NN}}$ = 62.4 GeV. This energy density is almost 50-100 times the cold nuclear matter density and is a lower bound to the estimated energy density. This is because, there is a strong reduction in observed E_T relative to that produced initially, due to the longitudinal hydrodynamic work done during the expansion of the system. All these different approaches agree roughly for the estimated energy density, with a value which is well in excess of that predicted by lattice QCD for the deconfinement phase transition. Taking similar colliding species i.e. Au, from all the similar measurements (top 5% central collisions) of the initial energy density at RHIC energies and assuming the validity of Bjorken hydrodynamic model at energies higher to RHIC, we have predicted the value of $\epsilon_{Bj}\tau \sim 9.42\pm0.55\ GeV/fm^{-2}c^{-1}$ for LHC. In this approach the advantage of taking similar colliding species is that, the estimation will be independent of the number of participant nucleons.

We have also made predictions for the E_T and charge particle multiplicity for the LHC energies, based on the measurements of $dE_T/d\eta$ per participant pair and $dN_{ch}/d\eta$ per participant pair at different energies from AGS to RHIC. These quantities show a logarithmic increase with the center of mass energy. Based on the extrapolation of the above logarithmic behavior, we have given prediction for the LHC energy. The values of $dN_{ch}/d\eta$ and $dE_T/d\eta$ at LHC, are $\sim (6.53 \pm 0.45) \times (0.5N_{part})$ and $\sim (6.03 \pm 0.11) \times (0.5N_{part})$ respectively.

The electromagnetic fraction of the total transverse energy for top 5% central events obtained in this work is 0.318 ± 0.036, consistent with a final state dominated by mesons. There are theoretical predictions regarding the formation of a long-lived deconfined plasma state in central events, which increase the yield of direct photons. This, however should increase the electromagnetic fraction of the transverse energy. Our observations at RHIC, suggest the electromagnetic fraction is almost independent of collision centrality. Hence, from this behavior and the values of the electromagnetic fraction of transverse energy obtained at RHIC, it is not possible to conclude regarding the formation of a long-lived plasma phase. This however, doesn't discard the possibility of formation of a plasma for a very short period of time. In addition, the ratio of E_T^{em} to E_T^{had} increases with center of mass energy. The meson dominance at higher energies is reflected from this behavior.

Furthermore, we have studied the event-by event fluctuations in E_T and in the ratio of it's components. We have taken the σ/μ as the fluctuation variable. For 5% most central collisions, the fluctuation in E_T is found to be 8.4%. The fluctuation in E_T has been found to increase when we go from central to peripheral collisions. The fluctuations in E_T^{em}/E_T^{had} and E_T^{em}/E_T are found to be 14.4% and 9.74% respectively, for the 5% most central collisions at $\sqrt{s_{NN}} = 62.4$ GeV.

Bibliography

[1] J. Adams *et al.*, STAR Collaboration, *Phys. Rev. Lett.* **92** (2004) 052302.

[2] P.F. Kolb and U. Heinz, nucl-th/0305084 (2003).

[3] C. Adler *et al.*, STAR Collaboration, *Phys. Rev. Lett.* **89** (2002) 202301; C. Adler *et al.*, STAR Collaboration, *Phys. Rev. Lett.* **90** (2003) 082302; J. Adams *et al.*, STAR Collaboration, *Phys. Rev. Lett.* **91** (2003) 072304.

Appendix A

Estimation of Systematic Errors

A.1 Estimation of Systematic Errors

If we measure $x_1,\ x_2,\ ....,x_n$ with uncertainties $\delta x_1,\ \delta x_2,.......,\delta x_n$ and these measured values are used to compute the function $q = f(x_1, ..., x_n)$, then the uncertainty in q is given by

$$\delta q = \sqrt{\sum_i^n (\frac{\partial q}{\partial x_i})^2 (\delta x_i)^2} \qquad (A.1)$$

This is valid if the uncertainties in $x_1,\ x_2,\ ....,x_n$ are independent and random in nature. This is the general formula for propagation of errors. We have used this formula for the estimation of the uncertainties in the measurements.

A.2 Estimation of Systematic Errors in E_T

For the estimation of E_T^{had}, the experimental formula is

$$E_T^{had} = C_0 \sum_{tracks} C_1(ID, p) E_{track}(ID, p) sin\theta \qquad (A.2)$$

The sum includes all tracks from the primary vertex in the range $0 < \eta < 1$ and for full azimuthal coverage. C_0 is the correction factor defined as

$$C_0 = \frac{1}{f_{acc}} \frac{1}{f_{p_T Cut}} \frac{1}{f_{neutral}}. \qquad (A.3)$$

The factor $C_1(ID,p)$ is defined as

$$C_1(ID,p) = f_{bg}(p_T)\frac{1}{f_{notID}}\frac{1}{eff(p_T)}, \tag{A.4}$$

The factors used in the estimation of C_0 and C_1 are already discussed in Chapter 3. Using Eqn. A.1 and the correction factors, we have first estimated the systematic errors in the factors C_0 and C_1. The uncertainties in the estimation of C_0 and C_1 are given by the following formulae.

$$\delta C_0 = \sqrt{(\frac{1}{f_{neutral}\ f^2_{p_TCut}})^2(\delta f_{pTCut})^2 + (\frac{1}{f_{p_TCut}f^2_{neutral}})^2(\delta f_{neutral})^2}. \tag{A.5}$$

Here, $f_{acc} = 1$.

$$\delta C_1 = \sqrt{(\frac{1}{f_{notID}\ eff})^2(\delta f_{bg})^2 + (\frac{f_{bg}}{eff\ f^2_{notID}})^2(\delta f_{notID})^2 + (\frac{f_{bg}}{(eff)^2 f_{notID}})^2(\delta eff)^2}. \tag{A.6}$$

The uncertainties in C_0 and C_1 are then used to estimate the error in E_T^{had} due to the uncertainties in correction factors. Finally, the uncertainty in E_T^{had} is measured by adding in quadrature, the uncertainties due to the correction factors and that due to the dynamic cuts.

In a similar fashion, the systematic errors on E_T^{em} and N_{ch} have been estimated using their experimental formulae. The systematic error in E_T is given by

$$\delta E_T = \sqrt{(\delta E_T^{had})^2 + (\delta E_T^{em})^2} \tag{A.7}$$

A.3 Estimation of Systematic Errors in Ratios

We have used observables like $(dE_T^{em}/d\eta)/(dE_T/d\eta)$ and $(dE_T/d\eta)/(dN_{ch}/d\eta)$ to study E_T production. The systematic uncertainties in these ratios have been estimated using the following formulae.

$$\delta(E_T^{em}/E_T) = \frac{1}{E_T}\sqrt{(\delta E_T^{em})^2 + (\frac{E_T^{em}}{E_T})^2\ (\delta E_T)^2} \tag{A.8}$$

$$\delta(E_T/N_{ch}) = \frac{1}{N_{ch}}\sqrt{(\delta E_T)^2 + (\frac{E_T}{N_{ch}})^2\ (\delta N_{ch})^2} \tag{A.9}$$

The systematic error in $(dE_T/d\eta)/(0.5N_{part})$ is estimated using the formula

$$\delta[(dE_T/d\eta)/(0.5N_{part})] = \frac{1}{0.5N_{part}}\sqrt{(\delta(dE_T/d\eta))^2 + (\frac{dE_T/d\eta}{N_{part}})^2\ (\delta N_{part})^2} \tag{A.10}$$

The systematic error in σ_{E_T}/E_T, which is used to study E_T-fluctuation, is also calculated in a similar way using Eq. A.1.

A.4 Estimation of Systematic Errors in $\epsilon_{Bj}\tau$

The Bjoken formula used to estimate the initial energy density is

$$\epsilon_{Bj} =< \frac{dE_T}{dy} > \frac{1}{\tau\pi R^2} \tag{A.11}$$

where, τ is the formation time and πR^2 is the transverse overlap area of the colliding nuclei. The nuclear radius $R = R_0 A^{1/3}$, where A is the mass number of the nuclei. As discussed in Chapter 3, to study the centrality behavior of $\epsilon_{Bj}\tau$, we have used the relation $A = N_{part}/2$. A factor of 1.18 for $\eta \rightarrow y$-phase space conversion is used. Taking the above aspects into account, the formula for $\epsilon_{Bj}\tau$ simplifies to,

$$\epsilon_{Bj}\tau =< \frac{dE_T}{d\eta} > \times \frac{1.18}{\pi R_0^2 (N_{part}/2)^{2/3}} = \frac{< dE_T/d\eta >}{N_{part}^{2/3}} \times 0.414 \tag{A.12}$$

The systematic error in $\epsilon_{Bj}\tau$ is given by

$$\delta[\epsilon_{Bj}\tau] = \frac{0.414}{N_{part}^{2/3}}\sqrt{(\delta(< dE_T/d\eta >))^2 + (\frac{2}{3}\frac{< dE_T/d\eta >}{N_{part}})^2\ (\delta N_{part})^2} \tag{A.13}$$